POZNAN UNIVERSITY OF TECHNOLOGY

Faculty of Chemical Technology

Institute of Chemistry and Technical Electrochemistry
Division of Applied Electrochemistry

DOCTORAL DISSERTATION

Study of electrode/electrolyte interface of novel layered 2D materials

Badanie granicy faz elektroda/elektrolit nowych, warstwowych materiałów dwuwymiarowych (2D)

Masoud Foroutan Koudahi

Field of study: Chemical Technology

Supervisor:

Prof. dr hab. Elżbieta Frąckowiak

Poznan, 2024

Acknowledgment to the National Science Centre of Poland for providing financial support under the frame of the **OPUS project** (2018/31/B/ST4/01852), titled “Study of electrode/electrolyte interface of high stability and quick charge response” (Principal Investigator: **Prof. dr hab. Elżbieta Frąckowiak)** and the opportunity of conducting the **Preludium project** (2022/45/N/ST5/02275), titled “Preparation and characterization of novel 2D MXenes material” (Principal Investigator: **mgr inż. Masoud Foroutan Koudahi**).

"If you want the moon, do not hide from the night. If you want a rose, do not run from the thorns. If you want love, do not hide from yourself."

Rumi

Acknowledgments

The presented findings and achievements in this dissertation are the result of the dedication and help that I have received during the implementation of PhD studies from my supervisor and mentor, Professor Elżbieta Frąckowiak, as well as my colleagues of the powersourcegroup, Poznan. Working as a PhD student at Poznan University of Technology provided me precious and applicable understanding of the world of energy storage devices. I truly appreciate your assistance that allowed me to expand my knowledge.

In addition, I would like to express my gratitude to all co-authors of my publications for their perseverance and collaboration.

I would like to acknowledge my family, in particular my parents, for their unceasing support and care during my studies.

Table of contents

Abstract

The content of this thesis can be divided into four main sections. The initial chapter provides an introduction as a literature review based on the fundamentals and operational principles of energy storage devices. The main focus is dedicated to the design and performance of electrochemical capacitors (ECs) because the target materials in this dissertation are engineered as electrode materials for ECs. The second chapter presents investigations and results already published during the realization of my PhD studies. In particular, four publications, named Article 1, Article 2, Article 3, and Article 4, were selected as they present studies on novel 2D materials (3DG/FeS_2, 3DG/VS_2, MXenes) used as electrodes in ECs operating in aqueous media and ionic liquids. Article 1 and 2 concern meaningful information and strategies regarding the precise engineering of electrode materials based on transition metal dichalcogenides (TMDs) and carbons using hydrothermal reactors. The goal is to find safe potential limits for both EC electrodes, without electrolyte decomposition. Article 3 presents the fundamental understandings of the charge storage of transition metal carbides (MXenes) in aqueous media. The target is to clarify the type of bonding during charging/discharging of MXenes and to show alternatives for designing wide voltage range of ECs. Key information is related to the interactions involved in the hydrogen storage in MXenes. In Article 4, advanced *operando* technique such as electrochemical dilatometry is employed to track the volumetric expansion of different MXenes in ionic liquids. For the first time, a thorough investigation regarding the energy storage of such materials as TiMo/MXenes is presented. Two main members of MXenes, including Ti and Mo/Ti carbides, are prepared using different etching agents to remove Al from MAX phases. Various interlayer spacing and surface functionalities are obtained under different etching conditions. Ti carbides show high capacitive charge storage due to a high volumetric expansion in the negative potential range. In addition, faradaic currents driven by hydrogen bonding contribute to the capacitance of the electrode. In contrast, Mo/Ti carbides showed a significant strain increase for the positive electrode that correlates with the higher capacitance values.

The third chapter indicates the achievements, including publications, attended conferences, and projects that were conducted.

Streszczenie

Treść niniejszej pracy doktorskiej można podzielić na cztery główne części. Rozdział początkowy zawiera wprowadzenie będące przeglądem literatury dotyczącej podstaw i zasad działania urządzeń magazynujących energię. Główny nacisk poświęcono budowie i działaniu kondensatorów elektrochemicznych (EC), ponieważ materiały docelowe w tej rozprawie zostały zaprojektowane jako elektrody dla EC. W drugim rozdziale przedstawiono opublikowane wyniki badań, które zrealizowano w trakcie studiów doktoranckich. Wybrano cztery publikacje zatytułowane Artykuł 1, Artykuł 2, Artykuł 3 i Artykuł 4, które przedstawiają wyniki badań nowych 2D materiałów (3DG/FeS_2, 3DG/VS_2, MXenes) jako elektrody ECs, w środowisku wodnym oraz w cieczach jonowych. Artykuły 1 i 2 omawiają strategie dotyczące precyzyjnej preparatyki materiałów elektrodowych na bazie dichalkogenków metali przejściowych (TMD) i węgli w reaktorze hydrotermalnym. Celem tych badań było określenie potencjałów bezpiecznej pracy obu elektrod, bez rozkładu elektrolitu. Artykuł 3 przedstawia badanie procesu magazynowania ładunku w węglikach metali przejściowych (MXenes) w środowisku wodnym. Motywacją do tych badań było wyjaśnienie mechanizmu ładowania/wyładowania na granicy faz elektroda/elektrolit i zaproponowanie alternatyw dla projektowania EC o szerokim zakresie napięcia. Przedstawiono możliwe interakcje zachodzące podczas magazynowania wodoru w MXenes. W artykule 4 zastosowano zaawansowaną technikę, tj. elektrochemiczną dylatometrię, w celu śledzenia rozszerzania się objętościowego różnych MXenów w cieczach jonowych. Po raz pierwszy przedstawiono szczegółowe badania dotyczące magazynowania energii w materiałach typu MXenes. MXenes na bazie Ti i Mo/Ti spreparowano przy użyciu dwóch sposobów wytrawiania Al z fazy MAX, stąd różnią się odstępami międzywarstwowymi i grupami funkcyjnymi. Węgliki Ti prezentują wysoką pojemność w związku z objętościową ekspansją w zakresie ujemnych potencjałów oraz elektrochemiczną sorpcją wodoru. Przeciwnie, węgliki Mo/Ti wykazują objętościowe

zmiany podczas polaryzacji dodatniej elektrody, przy czym wzrasta także jej pojemność.

W rozdziale trzecim wskazano osiągnięcia, w tym publikacje, udział w konferencjach oraz zrealizowane projekty.

Abbreviations and symbols

Abbreviation	Description
3DG	-three-dimensional graphene
AC	-activated carbon
Ar	-argon
$BeSO_4$	-beryllium sulfate
BMP	-1-Butyl-3-methylimidazolium
C3mpyr	- N-Propyl-N-methylpyrrolidinium
CA	- Carbon Aerogel
CO_2	-carbon dioxide
CV	-cyclic voltammetry
CVD	-chemical vapor deposition
CNT	-carbon nanotube
CNF	-carbon nanfiber
ECs	-electrochemical capacitors
EDL	-electrical double-layer
EDLC	-electrical double-layer capacitor
EMIm	-1-Ethyl-3-methylimidazolium
FeS_2	-iron disulfide
GO	-graphene oxide
GCD	-galvanostatic charge-discharge
GITT	-galvanostatic intermittent titration technique
HCl	-hydrochloric acid

H_2SO_4	-sulfuric acid
ILs	-ionic liquids
MAX	-transition metal aluminum carbides/nitrides
MXenes	-transition metal carbides/nitrides
PTFE	-poly(tetrafluoroethylene)
SWCNT	-single walled carbon nanotube
TMDs	-transition mental dichalcogenides
KF	-potassium fluoride
LiF	-lithium fluoride
Li_2SO_4	-lithium sulfate
$Mo_2Ti_2AlC_3$	-molybdenum titanium aluminum carbide
$Mo_2Ti_2C_3T_x$	-molybdenum titanium carbide
MoS_2	-molybdenum disulfide
NaF	-sodium fluoride
Na_2SO_4	-sodium sulfate
NH_3	-ammonia
NO_3^-	-nitrate
$NaNO_3$	-sodium nitrate
TAA	-thioacetamide
Ti_3AlC_2	-titanium aluminum carbide
$Ti_3C_2T_x$	-titanium carbide
TFSI	-(trifluoromethylsulfonyl)imide
VS_2	-vanadium disulfide
WS_2	-tungsten disulfide

Chapter 1

Literature Review

1. Motivation and context of the research

Today's world is facing an urgent need to replace traditional energy sources with clean, renewable energies [1-4]. Concerns have been raised about the shortage and overgrowing consumption of fossil fuels [5-6]. Predictions state that the main reservoirs, including gas and oil, will run out by 2050 to 2060, and coal resources will be out of reach by 2080 [7-8]. Such exploitation significantly impacts air pollution and global warming [9]. As climate change accelerates, the global community at the UN Climate Conference 2015 agreed to reduce the earth's surface temperature by decreasing gas emissions [10]. Around the world, human beings are experiencing ramifications such as droughts, extinction of different species, food shortages, and rising sea levels [11-12]. Thus, social pressure to take necessary and effective measures for a quick transition from fossil fuels to green energies has been increased. The decarbonization of today's energy systems allows us to moderate the temperature increase below 2 °C, and to create a more compatible climate [13].

Hopefully, the planet offers a variety of clean energy resources such as hydropower [14], biomass [15], tidal energy [16], wind power [17], and solar energy [18] to end the further CO_2 pollution of our globe. Conversion of stored energy to electricity, transmission, and distribution between the consumers must be implemented to provide the required energy (Figure 1) [19].

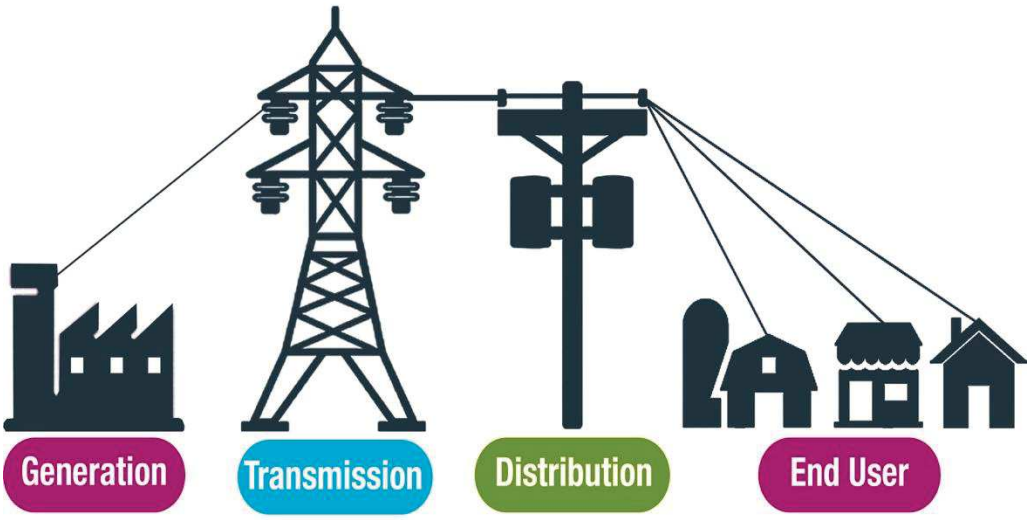

Figure 1. Schematic representation of necessary steps from the generation to the provision of electricity for the consumers.

Therefore, the European Commission aims to accelerate the electrification of industries, grid infrastructure, and the transport sector to meet the EU's 2030 climate and energy framework [20]. One of the key priorities is to establish strong, competitive, and sustainable energy storage devices in Europe. Meeting this target allows us to enhance the stability and efficiency of the power supply in not only portable applications such as transportation but also stationaries. The energy supply in the industry and grid sector is an example. In peak hours when the demand for power increases, the distribution system faces frequent interruptions as a result of an overload [21]. Natural accidents such as storms may disturb the stability of the energy supply to put a grid out of power for a time period, or even to cause a serious failure in electrical equipment [22]. This problem can be addressed by realizing backup power systems for a quick injection of electricity during the intervals [23]. Another issue is related to the cost of energy which varies at different hours of the day. In peak hours, consumers have to pay a higher price as the demand for energy supply goes up [24]. To decrease the power price, customers can store energy during the off-peak hours when the energy price is low and enjoy uninterrupted, cheap power in the high-demand period [25].

Where do we need to be in 2030? By 2030, Europe should be the host of reliable and efficient energy storage systems to guarantee grid and transport electrification giving a significant reduction of CO_2 emissions [26].

2. Introduction

From the Stone Ages till the modern era, energy supply is a must for having a convenient life and an essential production input. Without a doubt, energy can be considered the core driver for industrial evolution, where power accessibility led to a long-run growth of the economy, and subsequently, a rapid population increase [27]. In particular, the modified Newcome engine, also known as the Watt steam engine [28], allowed machines to be driven by steam instead of wind, water, or manpower. Noteworthy, Watt's engine was turned into a principle for the production of the steam turbine, from which the globe's electricity has been provided [29]. Although electricity generation lighted streets around the world, the primary energy for industry and transportation was provided by burning fossil fuels such as coal, oil, and natural gas [30]. The world gradually has become adopted for the maximum production, fast transportation, and easy utilization of energy. Overconsumption of traditional fuels has led to the pollution of the atmosphere, which subsequently causes major issues such as air pollution and global warming. We are at a critical stage in our lives, as society is encountering a fast transition from traditional to renewable energies and their consumption in the form of electricity. The stable and efficient provision of electricity depends on the development of energy storage devices [31]. The first battery was invented by Alessandro Volta in 1800, discovering the passage of current by soaking two pieces of silver and copper into an electrolyte. It is still the basis on which chemical batteries are working [32].

2.1. Energy Storage Devices

Electrical and electrochemical energy storage systems such as capacitors [33], electrochemical capacitors [34], batteries [35], and fuel cells [36] have attracted much

attention in the recent years. They can be categorized mainly based on the nature of the mechanisms or interactions by which energy is stored. Traditional capacitors are made of two conductive plates and a separator in between, made of solid dielectric materials like ceramic [37-38]. Once a potential difference between plates is applied, the negative and positive charges are polarized on the surface of the plate with the opposite charge. Such interactions are electrostatic, and no chemical reactions are involved [39]. The fast kinetics of adsorption/desorption allows capacitors to deliver a small amount of electrical energy on short notice [40-41]. On the other hand, batteries and fuel cells follow the second type of mechanism in which faradaic reactions are responsible for energy storage [42-43]. These reactions require the transportation and diffusion of active ions into the bulk of electrode materials, and therefore, they are slow in kinetics compared to electrostatic interactions [44]. Nevertheless, a higher energy is accessible because of the occurrence of faradaic interactions [45]. To exploit both high energy and power densities, electrochemical capacitors (ECs) were largely introduced [46]. In these devices, fast adsorption/desorption of ions at the surface rather than in the bulk of electrodes is at the origin of energy storage [47]. Hence, the kinetics of interactions are substantially faster than in-bulk faradaic reactions. Another advantage of ECs is their long cyclability in comparison with batteries [48]. This is because of the nature of surface interactions, which is more stable and less destructive than faradaic interactions that require repetitive ionic insertion/deinsertion into the bulk sites [49]. Figure 2, known as the Ragone plot, compares the energy *versus* power performance of different energy storage systems [50]. These factors are determined by the nature of reactions by which the energy storage system operates. As a result, batteries and fuel cells with a slow kinetic interactions are located at the top left corner of the plot, while electrochemical capacitors can be found on the right side. On a practical basis, however, various factors govern the performance of a system, which will be discussed in detail further.

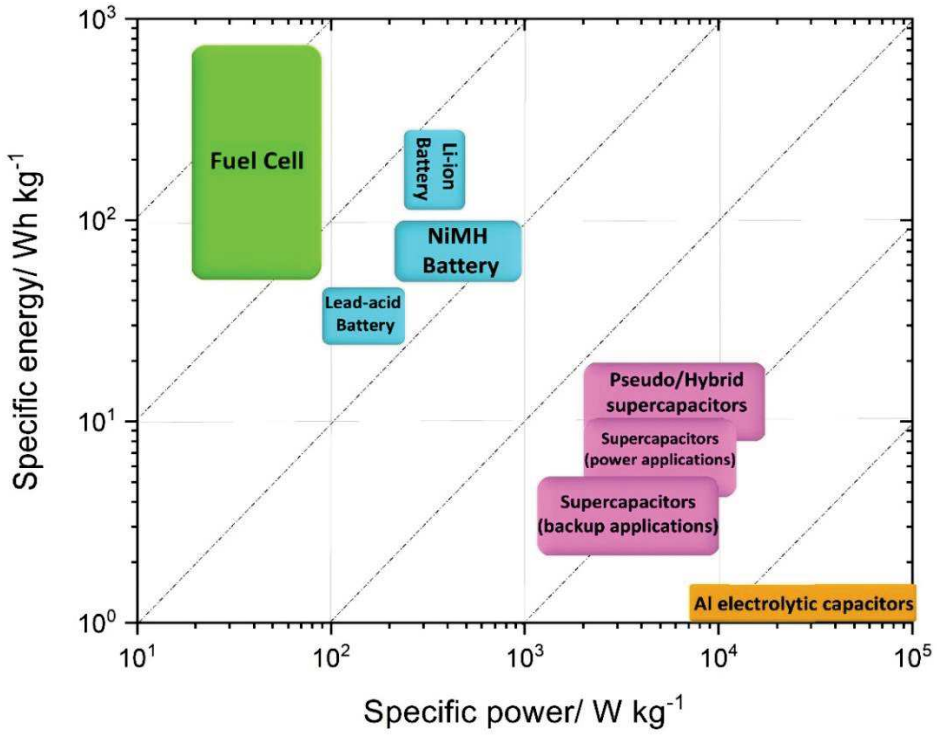

Figure 2. Comparing the energy and power performance of different energy storage devices.

2.2. Electrochemical capacitors (ECs)

Electrochemical capacitors, or supercapacitors store energy by the fast adsorption/desorption of active ions at the electrode surface [50-51]. ECs consist of two electrodes and a porous membrane in between that is ionically conductive but electronically insulating. Electrodes are connected to the current collectors, and both of them are soaked in an electrolyte medium [52]. ECs can be divided into two main categories (Figure 3), distinguished by the type of involved interactions in each system [53].

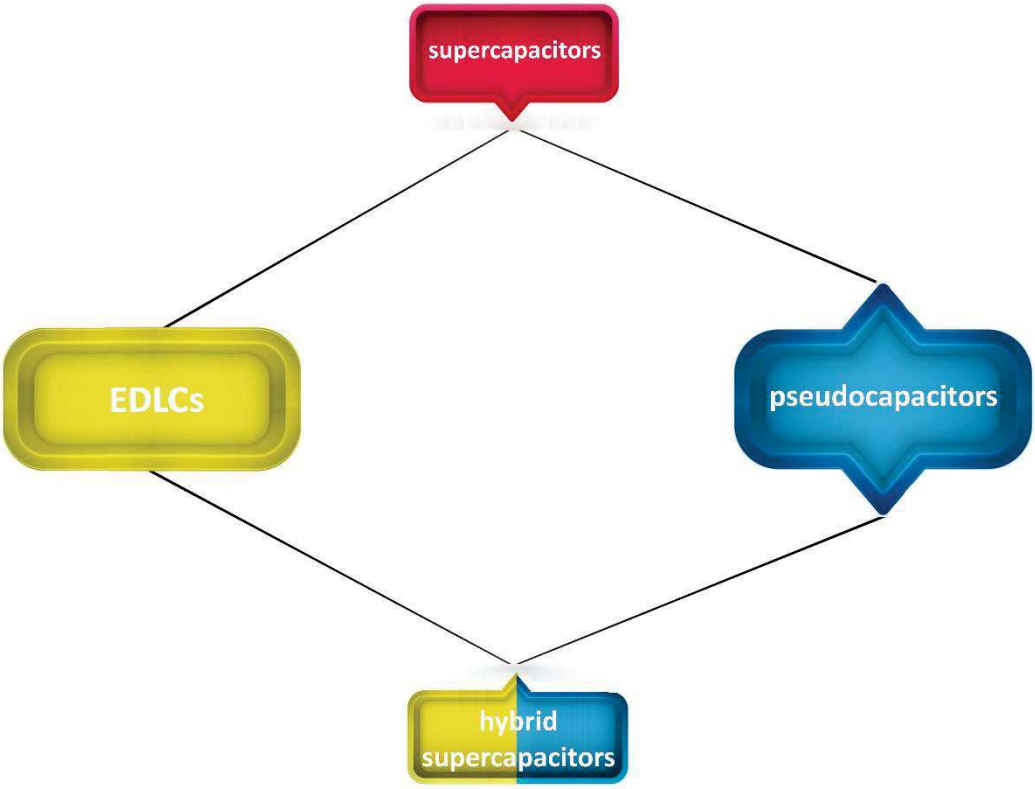

Figure 3. The main category of ECs, including electrical double-layer capacitors (EDLCs), pseudocapacitors, and hybrid capacitors [53].

Electrical double-layer capacitors (EDLCs) store energy exclusively by charge separation [54-55]. In other words, the cell does not undergo chemical reactions. Applying an external voltage difference between the negative and positive electrodes results in the migration and accumulation of ions at the electrode surface with an opposite charge [56]. During the discharge, ions return to the bulk electrolyte. By doing so, a small amount of energy in a quick interval is accessible. The energy storage mechanism of EDLCs can be defined by different theories, including Helmholtz [57], Gouy-Chapman [58], and Stern models [59]. The Helmholtz theory is the earlier explanation, and the term “double-layer” comes from this model. During charge, electronic and ionic layers at the electrode/electrolyte interface are formed. These layers are insulated by a single layer of solvent molecules, named the inner Helmholtz plane, and therefore, no charge transfer occurs between the electrode and electrolyte [60-61]. The ionic layer is called the outer Helmholtz plane, which includes solvated ions with the opposite charge than the electrode surface. Furthermore, a second layer

of solvated ions, named the diffusion layer, is formed far from the surface [62]. The EDL capacitance can be taken as the sum of capacitances originating from the outer Helmholtz plane and diffusion layer [63]. In Equation 1, ε_0 and ε_r are the permittivity of free space and relative permittivity of the electrolyte medium, A is the electrode surface area, and d stands for the thickness of electrode/electrolyte interface [63, 64].

$$C_{dl} = \varepsilon_0 \varepsilon_r \frac{A}{d} \qquad \text{Equation 1}$$

According to Equation 1, the magnitude of EDL capacitance has a direct relation with the surface area of electrode materials. Therefore, carbon materials with a well-developed micro and partly mesoporous structure are usually the best candidate as electrode materials for this application [65]. The second type of ECs, pseudocapacitors, indirectly store electrical energy by redox reactions at or near the electrode surface [66] rather than charge accumulation (EDLCs) or in-bulk redox mechanisms (batteries). The term “pseudo”, meaning false or fake, is being used as a prefix here to indicate the comparable but slower kinetics of interactions in comparison with EDLCs [67]. As faradaic reactions are responsible for the passage of charge, higher energy than EDLCs is stored, while the power performance of the cell may face a decline [68]. Up to now, three different types of pseudocapacitive interactions have been explored. The earlier one was introduced by Conway and Gileadi in 1962, where the quick electrochemical adsorption/desorption of hydrogen or hydroxides at the surface of platinum or metal oxide were responsible for charge storage [69]. These interactions were taken as “pseudocapacitive adsorption”, because the deviation of capacitance *versus* voltage was linear, and the adsorption of the aforementioned species was occurred exclusively at the surface. In 1997, the same assumption was used by the Conway group to hold “redox pseudocapacitive” currents responsible for the observed faradaic behavior of hydrous RuO_2 in an aqueous acidic medium [70]. Recently, MXene metal carbides/nitrides have shown pseudocapacitive response during the ionic insertion/deinsertion, although the electrode shows no structural changes. These interactions are named as “intercalation pseudocapacitance” [71-72]. However, the

term intercalation usually is used for describing the interactions of ions with anodic graphite in batteries [73]. Figure 4 schematically compares the difference between the three types of pseudocapacitive interactions and the intercalation behavior of battery-type electrodes. Noteworthy, all pseudocapacitive interactions are different from intercalation or insertion in battery materials, as during a pseudocapacitive response the electrode undergoes no phase or structural transformations due to faradaic reactions. Another misleading definition that must be highlighted here is that many researchers assign the term “pseudocapacitive” to the battery-like behavior of an electrode [74-76], but these two are different.

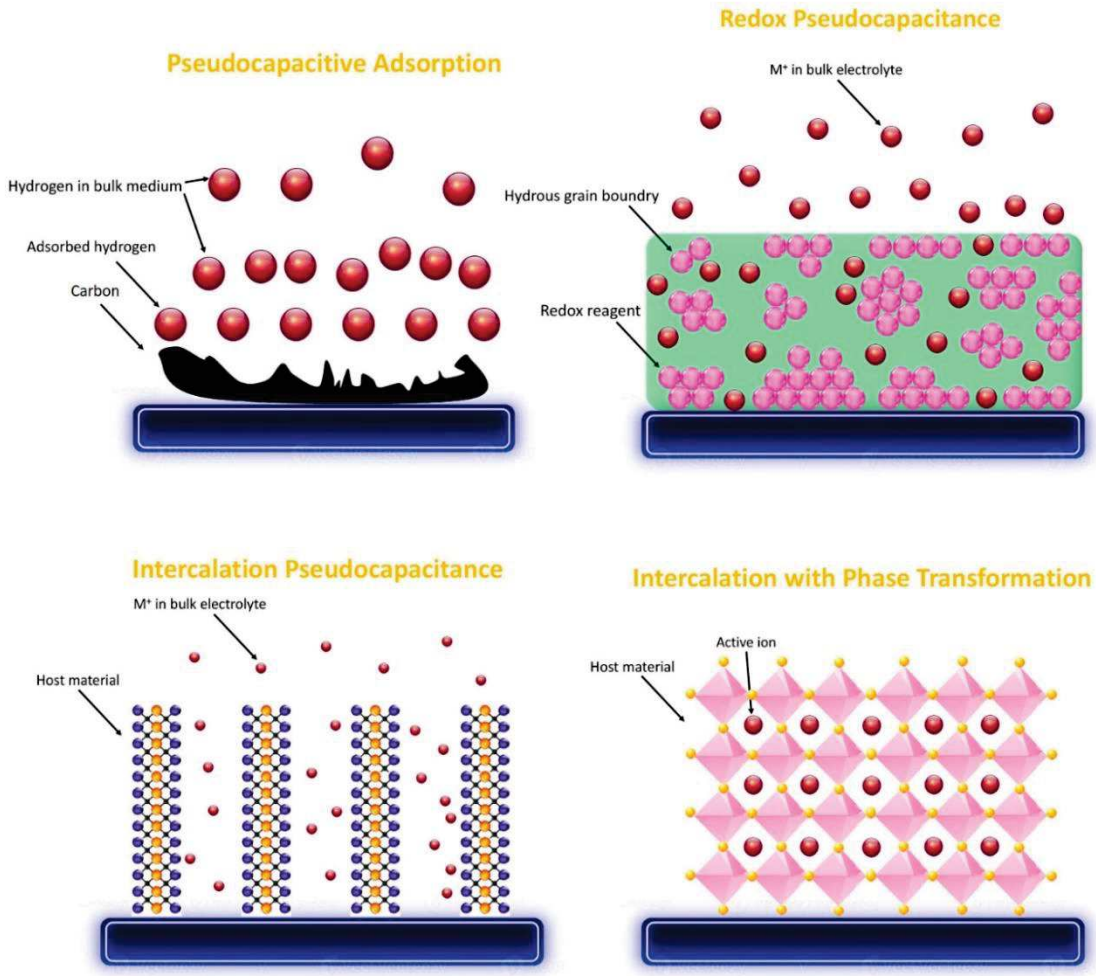

Figure 4. Comparison between different types of pseudocapacitive mechanisms in electrochemical capacitors and intercalation with phase transformation in batteries

Electrodes with a pseudocapacitive response usually suffer from a working in a narrow

potential ranges. Hence, materials with a pure capacitive behavior usually is employed as the counter electrode [77-79]. Integration of EDLCs and pseudocapacitors results in harvesting a high energy and power density simultaneously (hybrid supercapacitors) [80-81]. Improving the energy and power performance of the cell is also reachable by combining pseudocapacitive and EDL materials (hybrid electrodes) [82-84]. In particular, EDL materials such as nanotubes can act as a conductive additive, they also serve as a substrate for the deposition of pseudocapacitive materials.

2.3. Electrode materials for electrochemical capacitors

As it was mentioned, ECs store energy by ionic adsorption/desorption at the electrode surface, and therefore, high surface area materials are of interest. Traditionally, porous carbons have been used as active materials in EDLC applications [85-86]. Following the theoretical conceptualization of pseudocapacitance by Conway and Gileadi, various materials such as metal oxide/hydroxide [87,88], sulfide [89], carbide/nitrides [90] or conductive polymers [91] were employed as the electrodes to improve the energy performance of ECs. These materials can be classified based on the target application for which the electrode will be designed. Figure 5 presents different type of materials that is used as the electrode in ECs.

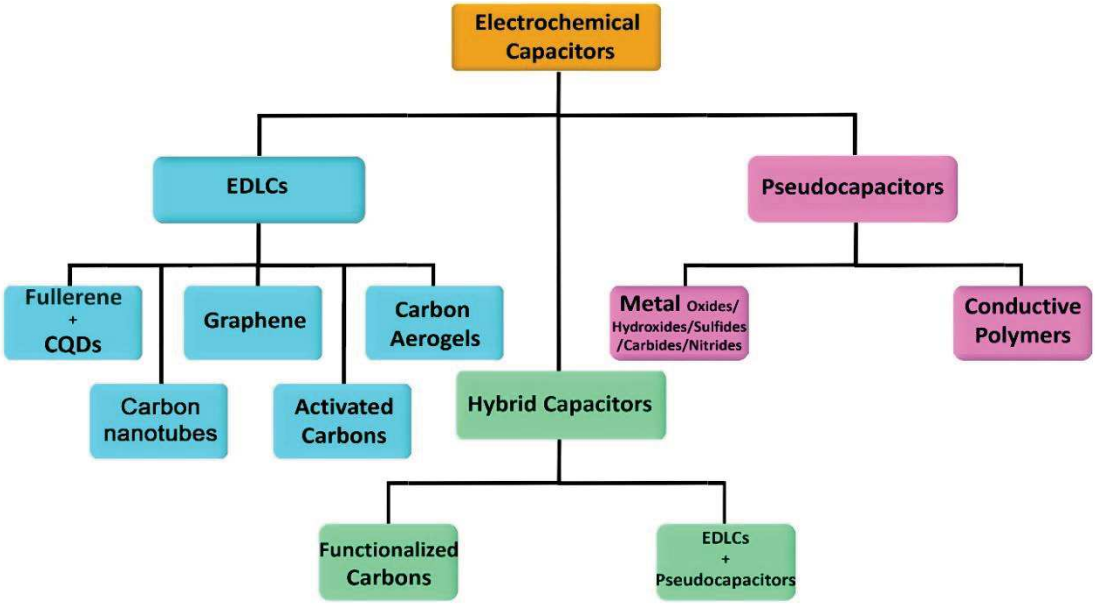

Figure 5. Classification of various active materials for EC application.

2.3.1. Carbon structures

Carbon materials are well known for their outstanding properties, including low price, versatility in form, easy processability, being environmentally friendly, high conductivity [92-95]. In addition, they have a high chemical [96] and electrochemical [97] stability. Therefore, carbons have been widely used as active materials for various energy storage applications. In particular, the energy performance of EDCLs strongly depends on the surface properties of active material, where carbon structures with controllable micro and mesoporosity and a large surface area are among the best candidate [98-100]. These materials can be categorized based on their dimension. Figure 6 indicates examples of already investigated carbon structures as active materials.

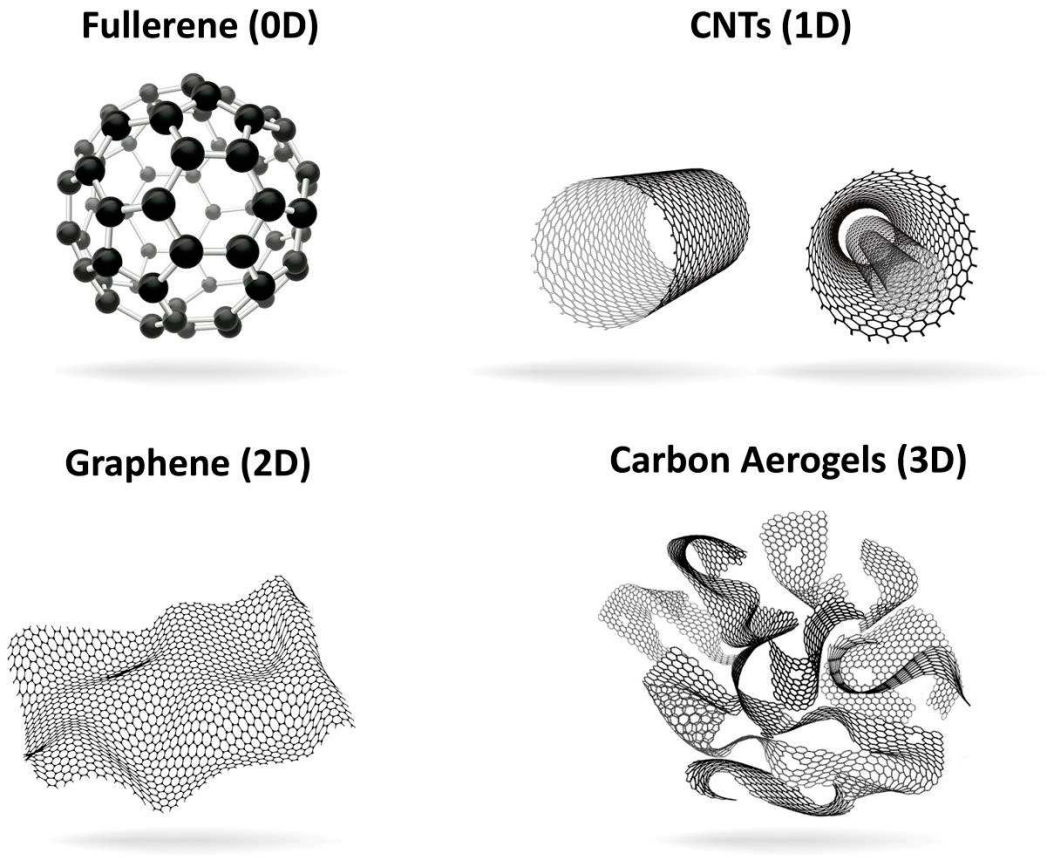

Figure 6. Carbon materials with various dimensions.

Activated carbons

The most commonly used electrode materials for EC applications are based on activated carbons (ACs) [101-102]. Various natural or artificial raw materials can be carbonized and subsequently activated to prepare ACs [103]. Controlling the physical and structural properties of the material is doable by manipulating the reaction parameters, type of precursors, or the synthesis route [104]. Following the carbonization of raw materials, an activation step will be taken to enhance the surface area of the final product (up to 2000 $m^2 g^{-1}$) [105]. Having such a developed surface area, AC-based ECs can deliver a specific capacitance between 100 to 150 F g^{-1} which depends on the type of electrolyte medium [106]. The high corrosion resistance of ACs guarantees the stable storage performance of the cell over a long-period of charge-discharge cycles. Physical activation of ACs can be done by applying microwave radiation [107] as well as CO_2 or steam treatments at high temperatures [108]. For the chemical activation, exposure of AC particles to acidic media (1M H_2SO_4 or H_3PO_4) [109] or basic solutions (KOH) [110] at high temperatures is carried out. The porous texture of ACs must be tuned carefully as it plays an important role in the ionic mobility within the electrode. Template-based techniques can be employed to tune the porosity of the target AC with a high precision [111].

Fullerene and carbon quantum dots

Fullerenes comprise a highly symmetric cage-like skeleton in which each carbon has a sp^2 hybridization and is connected to 3 other carbons. Owing to its promising structural, electrochemical, and photophysical characteristics, such as a low band gap (1.6 eV), high electron affinity (2.65 eV) [112], and a strong electron-accepting property, C_{60} is the most studied member of the fullerene family [113]. One of the key features of fullerenes is their facile functionalization and integration with a variety of bulk components, to give high electronic and conductive features onto the surface of

the material. As an example, Ji *et al.* reported the preparation of cobalt/nitrogen-doped fullerene electrode materials with a significant EC performance in 1M H_2SO_4, reaching a high capacitance of 416 F g^{-1} at the current density of 1 A g^{-1} [114].

Another example of 0D materials is carbon quantum dots (CQDs) [115], made of ultrafine and quasi-spherical nanoparticles with a π-conjugated system and a particle size ranging less than 10 nm. In addition, CQDs can be easily functionalized or even integrated with pseudocapacitive materials for high energy density applications. For instance, a designed core-shell structure based on carbon quantum dots and polyaniline was able to deliver a capacitance equivalent to 264 F g^{-1} at the current density of 2.5 A g^{-1} [116].

Carbon nanotubes and carbon nanofibers

Carbon nanotubes (CNTs) are hollow tubes (diameters 15 to 40 nm and a length of 5-20 µm) with single or multilayer sp^2 hybridized carbon sheets. They have low density, excellent conductivity, large specific surface area (50-1315 m^2 g^{-1}) [117], and high mechanical and chemical stability. Therefore, they are a suitable candidate for EC applications, especially for high power demands [118]. The tunable electronic and ballistic electron transport properties of CNTs and nanofibers drive researchers to design various composite electrodes. Xu et. al reported the preparation of CNT bundles coated with a thin layer of polypyrrole. The core-shell design in this study facilitated the charge transfer between the CNT and polymer. The assembled flexible EC cell based on this electrode showed a high specific capacitance of 350 F g^{-1} and good cyclic stability with preserving 75% of its initial capacitance after 5000 cycles [119].

Conductive carbon structures with a high accessible surface area guarantee the effortless electronic and ionic transportation [120]. Owing to characteristics such as porosity and electrical conductivity, CNFs have attracted much attention in designing electrodes for high power performance applications. CNFs can be synthesized by a facile electrospinning step, followed by carbonization of polyacrylonitrile (PAN). The self-standing electrode based on the CNFs shows good conductivity and ionic diffusion due to the available mesopores. Therefore, a high energy and power density in

aqueous and nonaqueous-based electrolytes is reachable [121]. In another study, a binary MnO_2/Co_3O_4 oxide was wrapped around carbon nanofibers by electrospinning technique. The uniform coverage of metal oxides at the CNF surface allows the EC-based cell to reach high pseudocapacitive and EDL capacitance, hence, a high energy density of 64.5 Wh kg^{-1} at the power density of 1276 W kg^{-1} was obtained. Furthermore, the cell showed excellent capacitance retention by losing only 28.2% of its initial capacitance over continuous 11000 cycles [122].

Graphene

Graphene is a remarkable 2D material composed of a single layer of sp^2-bonded carbon [123]. Perhaps it can be nominated as the most reactive form of carbon materials, as both surfaces in a layer are accessible. Since its discovery in 2004 by Andre Geim and Konstantin Novoselov, many investigations has been oriented to utilize the outstanding chemical, physical, and electrical properties of graphene for various applications (Figure 7). It has a high theoretical surface area of 2675 $m^2 g^{-1}$ (equivalent to a theoretical specific capacitance of 550 F g^{-1}) [124], excellent electrical and thermal conductivity, and great tensile strength ($\sim$ 1 TPa). Graphene can be synthesized by a variety of top-down and bottom-up approaches, including mechanical exfoliation [125], chemical vapor deposition (CVD) [126], liquid phase exfoliation [127], chemical oxidation/reduction [128-130], and epitaxial growth [131]. After the delamination, graphene layers tend to ripple to have higher stability in the environment [132]. The chemical oxidation/reduction method, which has been applied extensively by researchers, is a top-down approach consisting of two major steps. First, graphite is oxidized using acidic media in combination with oxidant agents such as potassium permanganate, and in the second step, chemical or thermal treatments will be carried out to reduce the resulting graphene oxide to graphene. Upon applying the process, structural defects may arise at the surface of layers.

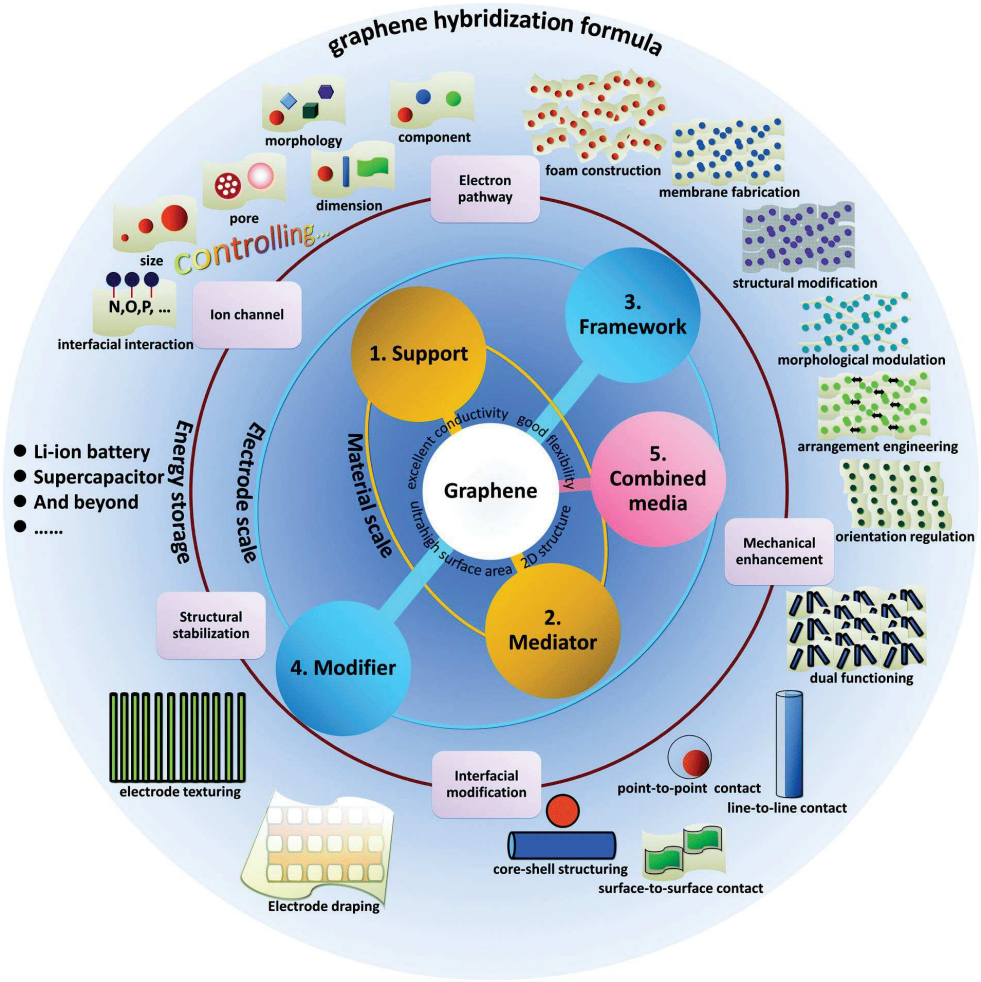

Figure 7. Properties of graphene, and its possible applications [133].

Figure 8 presents the formation of structural vacancies in a graphene oxide layer during the oxidation step in acidic media. Although the presence of vacancies may be taken as an advantage in some applications, they interrupt the charge mobility at the surface of graphene layers [134]. Hence, the energy storage performance of the cell can be degraded. In addition, structural defects may disrupt the continuity of the layer, and the resulting exposed edges may enhance the susceptibility of electrode material to corrosion reactions [135]. Subsequently, the long-term stability of the cell may decline.

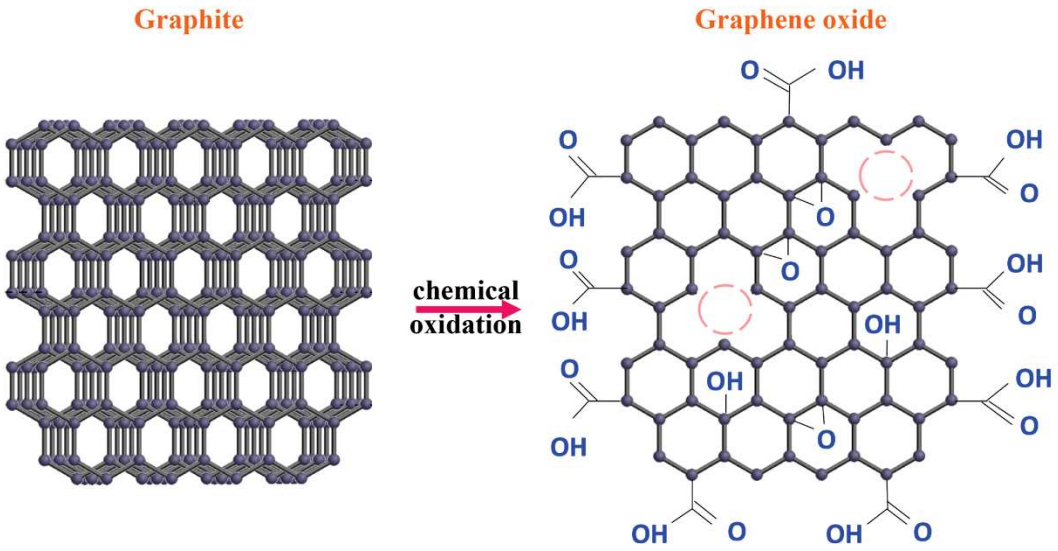

Figure 8. Transformation of graphite to graphene oxide during the first step of the oxidation/reduction process and the formation of structural defects (pink dashed circles) at the surface.

The high energy of the graphene surface makes it an ideal candidate for the decoration of pseudocapacitive materials or heteroatom doping. Liu et al. prepared nitrogen-doped graphene (NGS) by grafting ethylenediamine on the surface using the microwave method. The assembled cell based on NGS delivered a capacitance of 197 F g^{-1} at the current density of 0.5 A g^{-1} in an alkaline aqueous electrolyte. Furthermore, the cell showed 98% of capacitance retention after 5000 cycles [136]. In another work, a ternary electrode based on nickel foam/$NiCo_2O_4$ deposited on reduced graphene oxide was designed by the solvothermal method followed by a calcination step [137]. The EC-based hybrid electrode reached a promising energy density of 40.63 Wh kg^{-1} at a power density of 858.81 W Kg^{-1} and superior long-term cyclic stability by reaching 90.1% of its initial capacitance after 20000 charge-discharge cycles.

Despite such promising reports, graphene layers are suffering from a restacking tendency [138]. Agglomeration of graphene sheets to return to the former graphite structure results in a decrease in reactivity, initial surface area, and electrical conductivity.

In 2010, Shi et. al prepared a 3D graphene hydrogel (3DGH) by triggering the self-assembly interaction between the 2D graphene layers [130]. Upon applying certain temperatures and pressures on graphene oxide aqueous dispersion with a specific concentration (>2 mg ml^{-1}), the π-π attraction forces overcome the restacking tendency between graphene layers. At a critical point, the partial overlapping of layers results in a connection from the edges to produce a porous framework (Figure 9). By doing so, the agglomeration of graphene layers, which usually happens from basal planes is prevented. The resulting porous skeleton has pores with a wide range of size, a high electrical conductivity, very low density, and robust framework. Subsequently, the electrochemical performance of the prepared 3DGH was evaluated in a symmetric EC cell in aqueous electrolyte, where a specific capacitance of 160 F g^{-1} at the current density of 1 A g^{-1} was recorded. Elemental analysis showed the incomplete reduction of graphene oxide to graphene. Thus, the resulting 3DGH usually consists of untreated oxygen functionalities to some extent. Although the wettability of 3DGH electrodes in aqueous media considerably increases, the remained oxygen groups decrease the conductivity of the sample.

Tuning the porosity of graphene hydrogel can be an effective strategy for improving ionic electronic transportation, thereby increasing the capacitive performance of ECs. Duclairoir group evaluated the possibility of manipulating the pore size in 3DGH during the self-assembly process. For this purpose, they used hydrazine, ethylenediamine, and 1, 4-diaminobutane as the linkage to control the distance between graphene layers before becoming connected from the edges. The obtained images from SEM studies revealed porous 3DGHs with different pore size depending on the selected linking agent. In addition, the elemental composition of the resulting hydrogels was different, as the treated GO suspension with hydrazine showed a lower oxygen than the other two products. Finally, a high specific capacitance of 190 F g^{-1}, 152 F g^{-1}, and 136 F g^{-1} was recorded (current density of 0.5 A g^{-1}) for the obtained 3DGH by hydrazine, ethylenediamine, and 1, 4-diaminobutane treatments, respectively [139]. Noteworthy, the hydrazine-based 3DGH showed a pure capacitive response even at extremely high current densities (100 A g^{-1}). As these linkages have nitrogen in their

structure, one can claim that the higher content of nitrogen, and therefore, the higher pseudocapacitive response in the treated sample with hydrazine is the reason for the higher capacitance of the cell. However, elemental analysis of samples proves that the hydrazine-based 3DGH has a lower N content than the other two samples. The higher capacitance of this sample can be attributed to the higher electrical conductivity (1141 S m^{-1}) of the hydrogel (higher EDL capacitance) rather than its nitrogen content (higher pseudocapacitance).

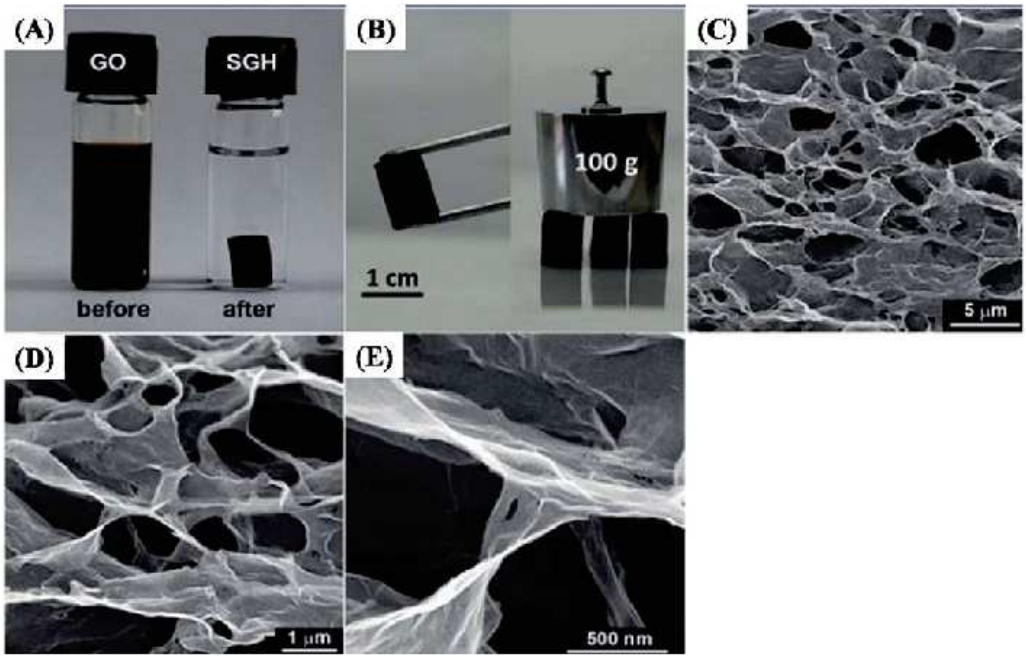

Figure 9. Image of the graphene oxide (GO) suspension and 3DGH as the precursor and the product of the self-assembly treatment (a). The high robustness of the freeze-dried 3DGH in preserving its structure against applying high pressure or weight (b). SEM images from the porous structure of the freeze-dried 3DGH (c-e) [130].

Owing to the high robustness of the framework, 3DGH can be used as a support for the decoration by other active materials, in particular, for high energy density applications. Sun et al. reported the formation of composite electrodes based on MnO_2 deposited on 3DGH by immersing the cylindrical graphene into a $KMnO_4$ solution, and subsequent thermal treatment. The assembled asymmetric cell based on 3DGH/MnO_2 showed a capacitive behavior in a wide voltage range (up to 2V). Moreover, an energy

density of 34.7 Wh kg^{-1} at the power density of 1 kW kg^{-1} was obtained [140]. In another study, Wu and his co-workers designed a hybrid electrode based on V_2O_5 nanofibers decorated on 3D graphene hydrogel [141]. For this purpose, the mixture of precursors was left under vigorous stirring till the gelation of the final product. Figure 10 presents the physical properties of the freeze-dried 3DGH-V_2O_5 monolith. The yellow color of the resulting cylindrical monolith reveals the integration of pseudocapacitive part with the graphene substrate. From the SEM images, homogenous dispersion of V_2O_5 nanofiber over the graphene walls is visible. An ideal pseudocapacitive response in 1M Na_2SO_4 aqueous electrolyte is reported using the symmetric cell.

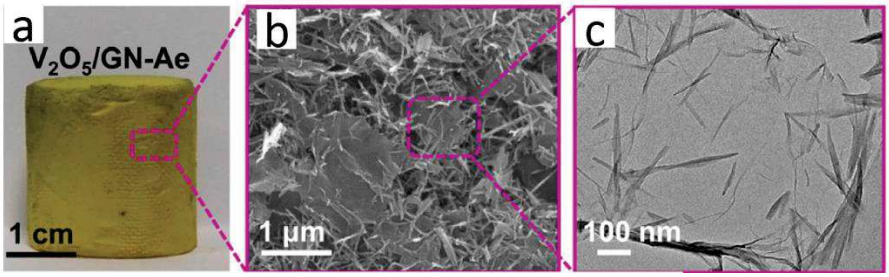

Figure 10. Structural properties of the freeze-dried 3DGH-V_2O_5 monolith, including a photo of the aerogel (a). SEM images from the interior framework of the composite (b-c) [141].

Another strategy to minimize the restacking tendency of graphene is by stabilizing the layers using spacers. Nanoparticles, conductive polymers, or carbon materials such as CNTs can be placed in the interlayer space between graphene layers to prevent their connection from the basal position. By doing so, the active surface area of graphene increases, as in this situation, both sides of the graphene layers are accessible to active ions. Mullen group engineered a composite electrode based on Fe_3O_4 nanoparticles and nitrogen-doped 3DGH, using a one-step hydrothermal self-assembly reaction [142]. Figure 11 indicates the morphological characterization of the prepared material. The SEM and TEM images revealed the presence of nanoparticles with a size ranging from 20-80 nm. Interestingly, it appears that some particles are encapsulated in between layers. A statistical analysis based on the obtained SEM images indicated that nearly 30% of the nanoparticles are sandwiched between two layers.

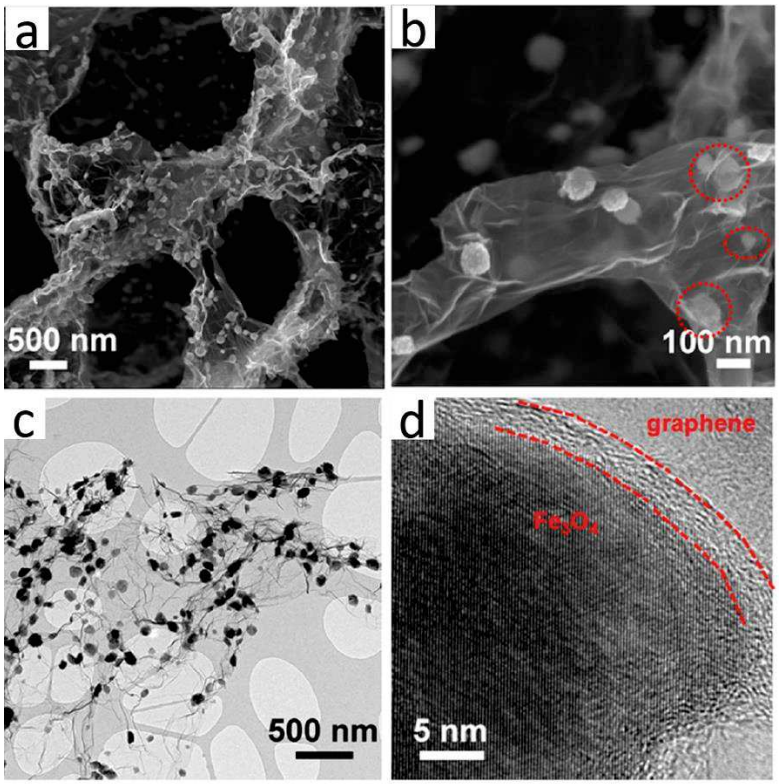

Figure 11. SEM (a-b), TEM (c), and HRTEM (d) images of the 3DGH/Fe_3O_4 hybrid material [142].

Carbon aerogels

Carbon Aerogels (CAs) are lightweight, interconnected macro/meso porous frameworks in which pores are filled with air [143]. With the possibility of undertaking high thermal treatments, in contrast to carbon hydrogels, CAs can deliver a very high electrical conductivity [144]. Hence, they are favorable as electrode material for EDLCs for high-power rate applications. CAs synthesis can be implemented through both top-down and bottom-up approaches [145-146]. In top-down methods, a thin layer of carbonaceous materials such as graphene and its derivatives are deposited at the surface of a porous substrate. Various techniques, including electrochemical deposition [147] and chemical vapor deposition (CVD) [148], can be used for this purpose. The thickness of the deposition can be controlled by the repetition of the process. Afterward, the substrate can be removed using a proper etchant [149]. The remained self-standing carbon may undergo further treatments for the decoration of

secondary active material. Wei et al. reported the synthesis of a hybrid electrode based on reduced graphene oxide (RGO) by deep-coating, using nickel foam (NF) as the substrate. Afterward, the NF/RGO was decorated with Ni_3S_2 and MoS_2 in a one-step hydrothermal reaction to enhance the energy performance of the electrode. An asymmetric cell based on the prepared composite showed a pseudocapacitive behavior in a wide voltage range (up to 1.6V) as well as high-rate capability and cycle performance [150]. The bottom-up routes for CAs production usually is divided into three stages. After gelation and subsequent aging, the material undergoes a solvent exchange step, followed by the final formation of the aerogel using various techniques such as pyrolysis, calcination, or carbonization. The resulting carbonaceous templates can act as the substrate for the deposition of pseudocapacitive materials. Bando and his co-workers reported the realization of self-standing 3D strutted graphene by a sugar-blowing approach [151]. The initiation of the gelation process was set by combining glucose with ammonium chloride. Furthermore, a specific temperature-programmed calcination step under an inert gas allowed to control the properties of the foam-like graphene (Figure 12). The calculated porosity of 99.85% and a very low density (3 mg cm^{-3}) for the product was calculated. The assembled CA-based EC has reached a power density of 893 kW g^{-1} at a very high current density of 100 A g^{-1}. However, it is necessary to underline that volumetric capacitance for such a low density material will be extremely low that can exclude EC from practical application where a volume for energy device is limited.

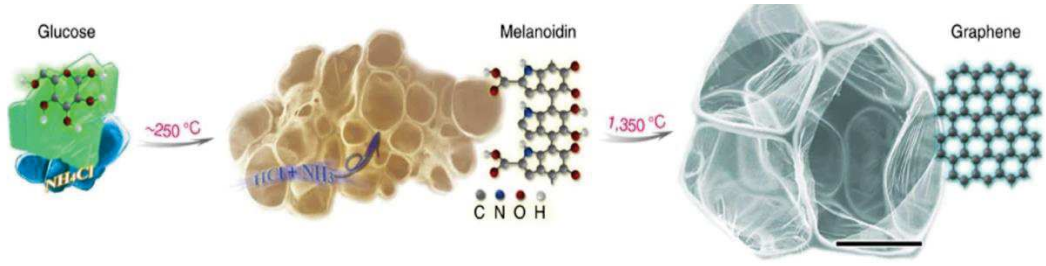

Figure 12. Schematic presentation of graphene-based CAs prepared by sugar-blowing process [151].

Designing electrodes that are thermally resistant and stable against corrosion improves the favorable capacitive behavior of the electrode. Activated carbon

electrodes provide a stable charge storage in a wide voltage range to 2.8 V in organic electrolytes. In practical applications, however, reaching a 300 to 500 V working voltage requires the stacking of a high number of ECs. To address this issue, Nishihara *et al.* suggested to increase voltage of a single cell by the preparation of mesoporous carbon sheets, using sacrificial alumina template [135]. In this design, the ratio of free edges to basal sites was reduced (Figure 13a). By doing so, the stability of the electrode, especially in high potential, was increased. The assembled cell based on this sample reached a very high voltage of 4.4 V with no obvious sign of electrolyte decomposition or electrode corrosion. Increasing the temperature of the study to 60 °C, the cell was able to operate up to 3.5 V. In fact, a small content of free edges slightly decreases the stability of the electrode material. The low ratio of D to G band which can be further translated to the small portion of free edges to basal planes already was reported in study of grain boundaries during the growth of graphene. Chen *et al.* compared the Raman mapping of different graphene structures, and he observed high intensity of D band because of not only structural defects but also due to grain boundaries (Figure 13b-c) [152].

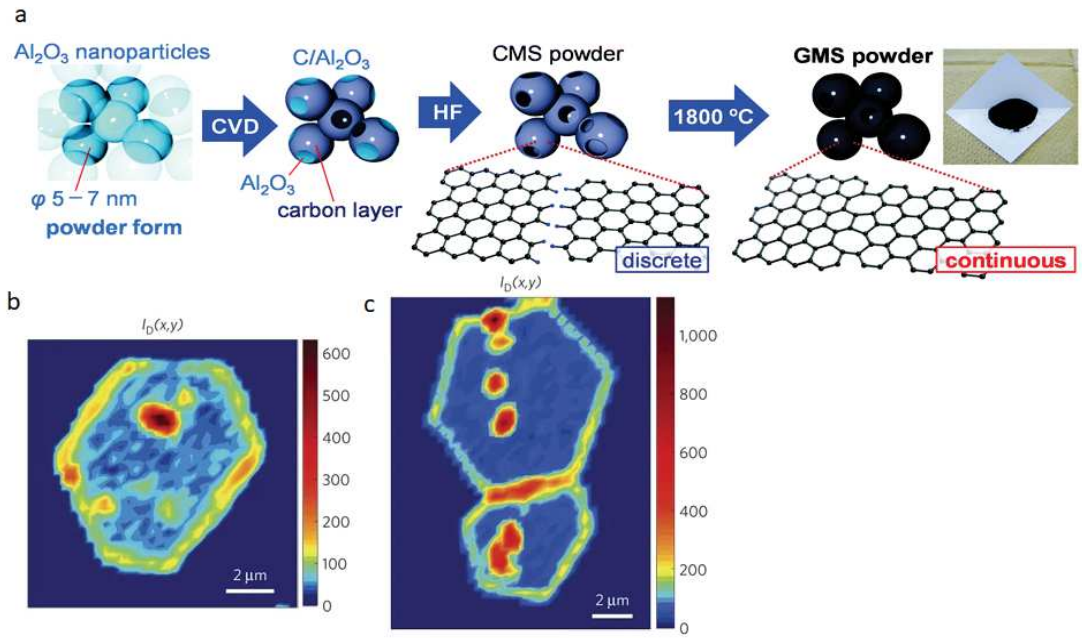

Figure 13. Step by step synthesis procedure of graphene mesosponge (GMS) powder (a). Raman mapping of a single (b) and connected GMS layers (c) [152].

In this dissertation, the following carbon materials have been used: Three-dimensional graphene (3DG), activated carbon Black Pearl (BP2000), activated carbon (YP80F), carbon nanotubes (CNTs). 3DG material served as the component of composites (3DG-FeS_2 and 3DG-VS_2), prepared by hydrothermal technique.

2.3.2. Transition metal dichalcogenides

Transition metal dichalcogenides (TMDs) are an appealing family of two-dimensional layered materials with a general formula of MX_2, in which M represents transition metals (from group 4 to 10 in the periodic table), and X stands for chalcogens (S, Se, and Te) [153-154]. In these materials, the covalently bonded atomic layers of chalcogen/metal/chalcogen form a sandwich structure which is taken as a layer of MX_2. The metal atom share electrons from their d orbital (oxidation state +4). Coverage of both surfaces of the metal layer with two layers of chalcogens in the absence of dangling bonds provides good stability for the TMD layer against reacting with the air and the environment. TMDs naturally exist in the bulk state and are made of a few layers that are connected by Van der Waals forces. Based on the coordination of transition metal with chalcogen atoms, multi-layered TMDs can be found in different polymorphic phases, including trigonal prismatic (2H or 3R) and octahedral (1T) [155]. These phases can be differentiated based on the stacking order of atomic layers in each MX_2 unit (Figure 14a-c). Considering the first chalcogen layer as X_1, the metallic plane as M, and the second chalcogen layer as X_2, it can be stated that in a 2H phase the chalcogen planes in X_1-M-X_2 combination are faced exactly in front of each other, while in the 1T and 3R phases, X_1 and X_2 occupy different positions. Regardless of polymorphic arrangements, each transition metal atom is coordinated with 6 chalcogen atoms. For example, MoX_6 in 2H, 3R, and 1T phases has a hexagonal, rhombohedral, and tetragonal geometry, respectively. In the bulk state, MX_2 layers are connected by Van der Waals (VdW) forces (Figure 14d), that brings important physical properties to TMDs such as forming van Hove singularities [156], band gap evolving [157], lattice vibration [156], and the quantum Hall effect [158-159]. Furthermore, the weak nature of VdW forces facilitates the cleavage of layers from the

bulk to the single monolayers. However, TMDs have the same tendency as graphene layers to restack to each other in order to have a higher stability [160].

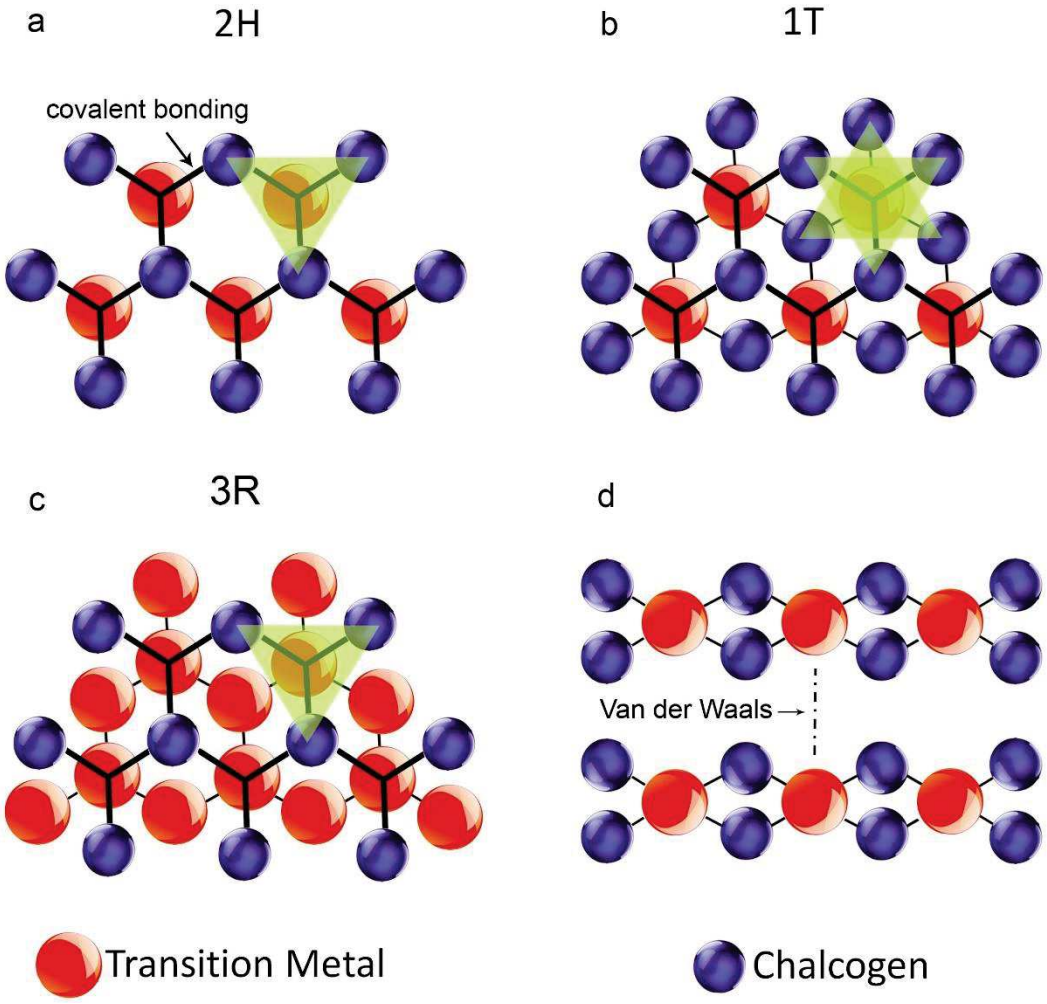

Figure 14. Top view schematic of 2H (a), 1T (b), and 3R (c) coordinations of transition metals and chalcogens in TMDs. Side view representation of two MX_2 planes that are bonded by Van der Waals interactions (d).

Having unique physical, chemical, and electrical characteristics, TMDs have found their pathway in a variety of applications ranging from electronics, optoelectronics, and valleytronics. Molybdenum disulfide is the first member of this family that was produced by Frindt in 1963. He used an adhesive tape to peel off a 100 Å-thick layer from its bulk phase [161]. In addition to molybdenum disulfides, there are various

TMDs such as WS_2 , TiS_2, NbS_2, VS_2 FeS_2 that have been extensively studied during recent years. Polymorphs in TMDs have an influence on topology, thermodynamic stability as well as electronic and structural properties [162]. For instance, the most abundant form of MoS_2, the 2H phase, shows a higher stability and but lower conductivity than 1T coordination. As another example, 3R-MoS_2 is promising in catalytic or photonic applications as there is a lack of inversion symmetry in their crystal phase in contrast to the 2H phase [163]. However, we cannot conceive a direct relation between the type of polymorph and the properties of TMDs. For example, WS_2 with a 1T phase has a metallic and distorted lattice, while its 2H phase has a higher conductivity. On the other hand, the 1T TiS_2 or 1T and 2H NbS_2 are superconductive. Figure 15 indicates the variation of TMD properties based on their polymorphic state.

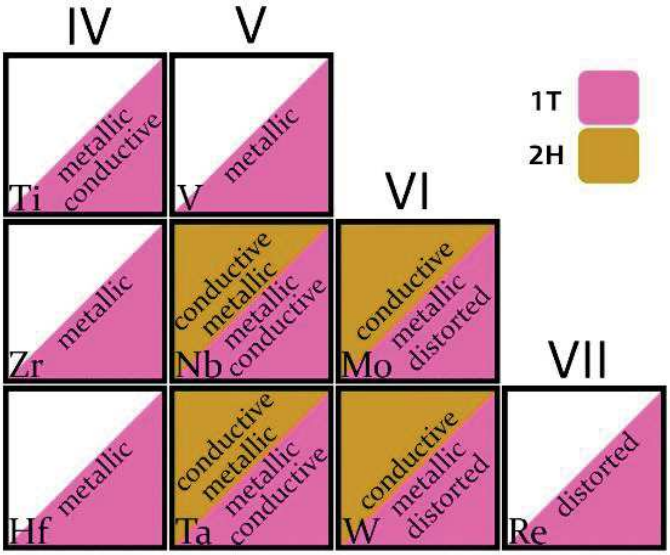

Figure 15. Most studied TMDs, which are based on transition metals from group 4 to 7, and their properties with respect to the 1T and 2H phases.

TMDs can be synthesized by various physical and chemical approaches. The top-down preparation of these structures by mechanical exfoliation using scotch tape is of interest as it results in high-quality single layers, which are ideal for surface application. Such delamination is also feasible in the liquid solution through sonication of the bulk sample in a proper solvent such as N-methyl-2-pyrrolidone. This technique is suitable for large scale production of TMDs. Nevertheless, precise sonication parameters must

be applied to avoid the breakage of layers. Also, the exfoliation and expansion of bulk TMDs is possible by intercalating proper ions such as lithium. In most cases, the resulted product is composed of pure monolayers with a high yield. However, the process is time consuming and it requires high temperatures. Therefore, the properties of the final product can be affected. To overcome this issue, electrochemical intercalation by galvanostatic charge-discharge technique, followed by a subsequent exfoliation step in H_2O or CH_3OH can be employed. By doing so, a better control over the sample is reachable, as the ion intercalation step can be monitored. Although top-down approaches are simple and inexpensive, they fail to provide monolayers with large lateral sizes like graphene. To solve this challenge, a proper substrate is submerged in a precursor solution to deposit a thin layer of TMD. The quality of the precipitated film can be improved by the calcination treatment in high temperatures. Preparation of large-area TMDs is doable by using the chemical vapor deposition (CVD) technique, which includes two stages of thermal treatments for converting precursors to the desired TMD and further heating to enhance the properties of the sample. Hydrothermal and solvothermal treatments are another bottom-up routes that have been used extensively for preparing TMDs.

In these approaches, a high temperature and pressure are applied to combine and form TMDs with controllable morphology and size from their transition metal and chalcogen precursors. For example, the possibility of tuning the morphology of the MoS_2 prepared in different solvents was evaluated by Wang [164]. They found that adding ethanol in a small amount to octylamine solvent during the solvothermal reaction alters the dimension of 2D TMDs nanosheets to a 3D hollow tubular arrangement that provides a higher ionic diffusion rate. In particular, ethanol molecules prevent nanosheets from interacting, which results in forming a tubular 3D morphology. The properties of TMDs can be tuned based on the target application. For example, reducing the thickness of the 2H-MoS_2 results in changing the position of the valence and conduction band. Subsequently, the band gap is converted from an indirect state to a direct one, thereby improving the conductivity of MoS_2 [165] for optoelectronic applications. Moreover, TMDs generally show a low overpotential for

hydrogen evolution reactions, which makes them an ideal candidate for catalytic application [166]. Various parameters that are involved during the preparation of TMDs result in the formation of structural defects or an increase in the portion of high energy edge sites. One of the consequences in this case is an increase in the rate of catalytic activities [167].

TMDs have attracted much attention in energy storage applications mainly due to their extremely high theoretical capacity, fast and highly reversible surface redox chemistry, and tunable interlayer spacing which can serve as the host for intercalation of active ions. This requires the exfoliation of bulk TMDs to their nanosheet structure, which improves the degree of surface interactions and reduces the charge transport pathway. From theoretical studies, TMDs such as thin layer MoS_2 can reach a very high capacity which is comparable to that of carbon nanotubes [168]. For fast surface charge storage, in particular, monolayer TMDs with 1T phase shows a promising electrical conductivity between 10-100 S cm^{-1}, considerably higher than that of 2H phases [169]. TMDs have attracted much attention from 1960s to 1970s for their energy storage performance, especially as the electrode in Li-ion batteries. However, major progress was initiated by the discovery of graphene in 2004, and since then, various efforts have been made to convert and isolate 3D TMDs into single layers. By doing so, better control on key physical and structural parameters, such as the changes in interlayer coupling and the degree of quantum confinement, was possible [170]. In recent years, there have been many studies on designing TMDs with a reduced dimension. One of the earliest investigations on TMD-based supercapacitors was carried out by Xie group. Briefly, the bulk vanadium disulfide was exfoliated to thin nanosheets by an ammonia-assisted approach. For this purpose, the bulk phase was undergoing a sonication step under the inert atmosphere [171]. Exfoliated VS_2 films with a high conductivity were obtained. The assembled EC cell reached a high capacitance of 4760 µF cm^{-2} and a stable cyclic performance, showing no capacitance degradation after 1000 charge-discharge cycles. In 2015, Chhowalla *et al.* used the chemical exfoliation method to turn the bulk MoS_2 into monolayers, where a mixture of 2H and metallic 1T phases with a proportion of 3 to 7 was obtained. The deposited

flexible electrode on the polyimide substrate (Figure 16a) was assembled into an EC cell in both aqueous and organic electrolytes. The MoS_2-based EC (mainly 1T phase) showed a higher capacitive response than that of 2H MoS_2 in all aqueous media. The higher conductivity of the 1T MoS_2 improved the EC power output such that the cell maintained its capacitive performance at high CV scan rates of 200 mV s^{-1} (0.5M Na_2SO_4). A high volumetric capacitance up to 700 F cm^{-3} and a satisfactory capacitance retention (95%) was recorded after 5000 continuous charge-discharge cycles in 1M H_2SO_4 [172]. Nevertheless, the high rate of catalytic electrolyte decomposition was revealed at around 0.8V and 0.6V *vs.* NHE in neutral and acidic media, respectively (Figure 16c).

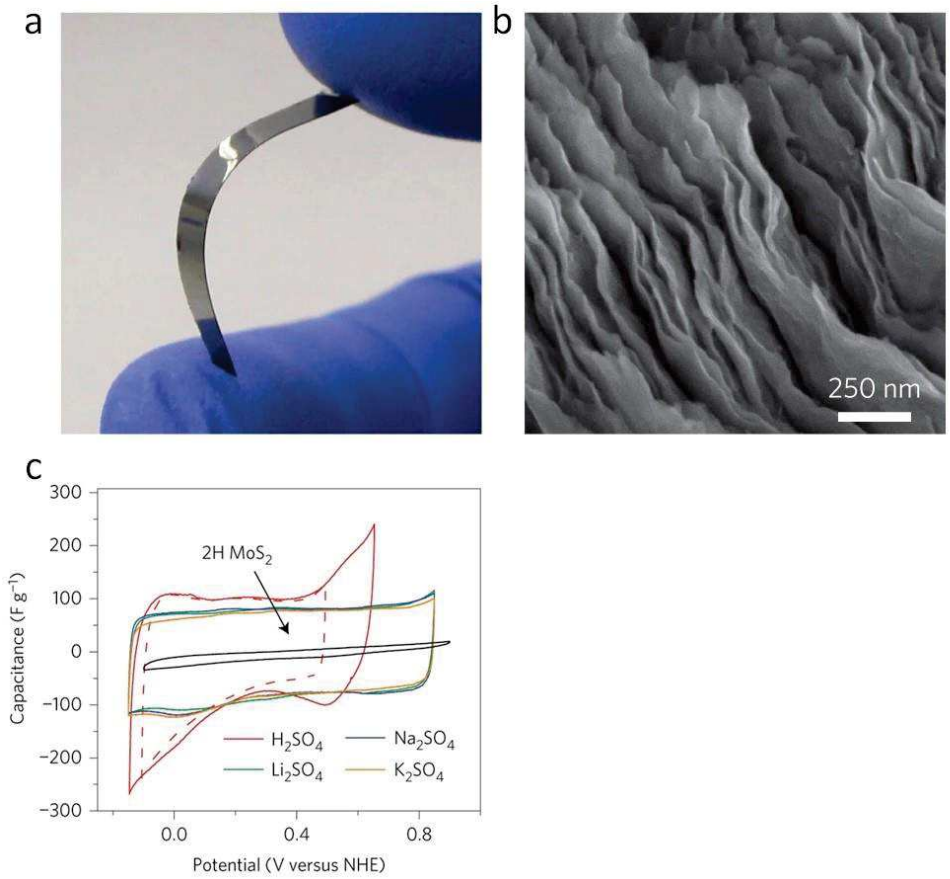

Figure 16. The image of the prepared flexible electrode based on 1T MoS_2 (a). The SEM image of the exfoliated 1T MoS_2 (b). The CV response of the electrode in various aqueous media (c) [172].

Wider voltage stability, by replacing the aqueous media with organic electrolytes, was observed (up to 3.5V). The higher viscosity and lower conductivity of organic solvents in comparison with aqueous media affect the power output of ECs. However, the cell based on 1T MoS_2 in organic media showed a stable CV response up to 100 mV s^{-1}. Dryfe compared the energy storage performance of various TMDs, named MoS_2, $MoSe_2$, WS_2, and TiS_2 to provide a better understanding of the mechanism involved in their charge storage [173]. For this purpose, a stable dispersion of each sample was prepared by sonication in N-methyl-2-pyrrolidone (NMP), followed by casting the dispersion on a PVDF membrane. A series of symmetric coin cells based on each sample were assembled in 1M Na_2SO_4. It was indicated that TMDs such as TiS_2 show higher conductivity and charge storage properties than MoS_2. In addition, they found that a combination of both EDL and pseudocapacitive currents are involved.

Expanding the working voltage of TMD-based ECs is feasible by realizing asymmetric cells. Manyala et al. prepared VS_2 nanosheets with a simple hydrothermal method, which further was assembled in a cell as the positive electrode versus activated carbon as the negative electrode [174]. A wide voltage range to 1.4V and a capacitance of 144 Fg^{-1} at the current density of 1 A g^{-1} (in 6M KOH) was recorded. However, the cell showed a high ohmic drop and quite low energy efficiency.

Integration of TMDs and carbon supports improves the electrochemical performance of the hybrid electrode. Pauzauskie reported the preparation of a composite electrode based on carbon aerogel decorated with 5-100 nm tungsten disulfide crystals [175]. Besides improving the conductivity and robustness of the hybrid electrode, the synergetic effect of the carbon framework led to an increase in the volumetric capacitance to 127%. The cell showed no capacitance degradation up to 2000 charge-discharge cycles.

2.3.3. Transition metal carbides/nitrides

Transition metal carbides (TMC) are carbon atoms bonded to transition metal from groups 3 to 6 of the periodic table with an empty d orbital [176]. Basically, they can be

counted as a combination of covalent solids and ionic crystals, as TMCs show a mixture of physical and chemical characteristics such as hardness, good electrical and thermal conductivity, and high melting point.

MXenes, are a new family of 2D materials with a layered structure. MAX phase is the parental structure of MXenes, which is made of covalently bonded transition metals (M), metals from group 13 or 14 such as Al, Ga, or Si (A), and carbon/nitrogen (X). MAX phases are generally prepared by thermal reactions, where elemental precursors in a stoichiometric ratio are mixed and reacted. The general formula of this phase is $M_{n+1}AX_n$, where the removal of the A element by various approaches results in the production of MXenes. During the etching process, the outer surfaces of each MXene unit will be covered by different functional groups such as –F, -Cl, and –OH, which give a hydrophilic nature to the material. Since early 2011 and by introducing $Ti_3C_2T_x$, as the first member of the MXenes family, there have been numerous reports based on other elemental combinations, including synthesized structures or predicted ones.

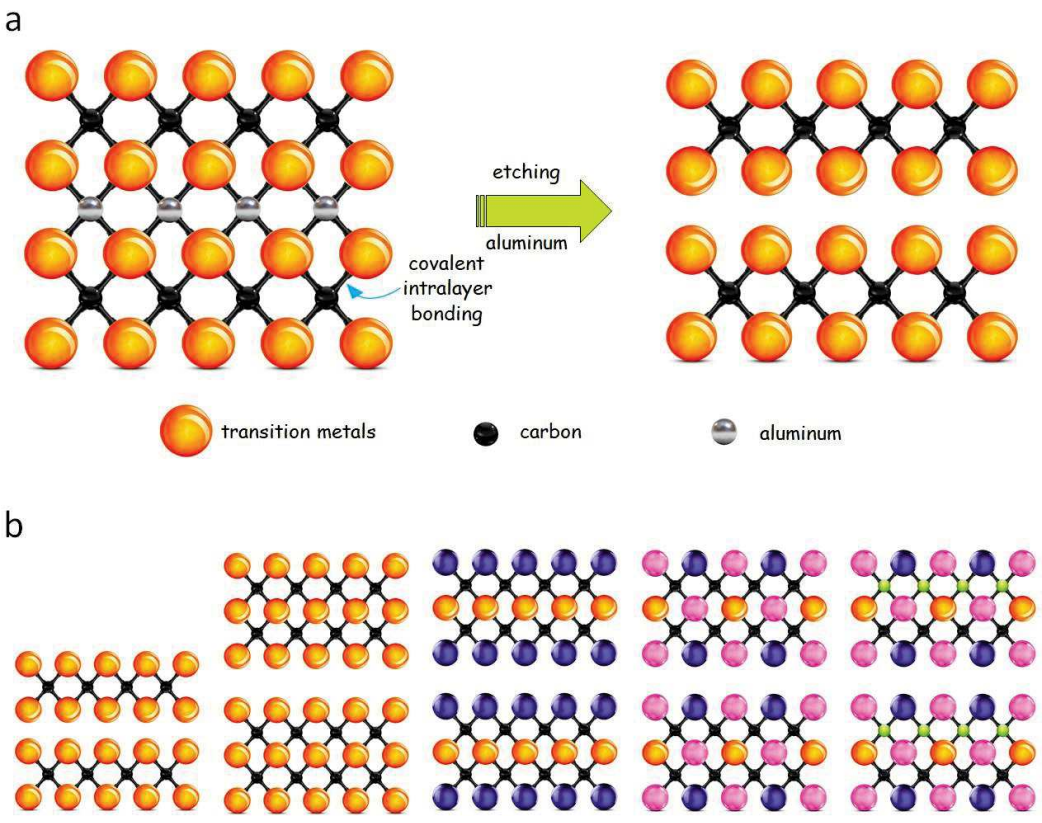

Figure 17. Schematic representation of MAX and MXene phases (a), and the diversity of the elemental combination in MXene materials (b).

Figure 17 demonstrates the chemical structure of MAX phases and MXenes as well as their elemental composition. MAX phase versatility in terms of elemental combination allows scientists to design MXenes with desired properties. A high electrical conductivity, hardness, mechanical robustness, high negative zeta potential, and efficient electromagnetic wave adsorption can be reached by tuning the elemental composition of this material.

Therefore, MXenes and their related composites have been employed in a variety of applications, such as energy storage, water desalination, catalysis, and drug delivery. There have been many reports on the synthesis of MXenes by wet-chemical approaches, which is also the earliest preparation method. The first attempt can be traced back to 2011, when Naquib *et al.* suggested the acidic etching of Ti_3AlC_2, using 50% concentrated hydrogen fluoride solution at ambient temperature and for a duration of 2 h. In addition, they suggested a chain of reactions involved in the MXene preparation [177]. After removing the aluminum layer, an accordion-like structure with an uneven interlayer spacing remains (Figure 18). By doing so, the surface accessibility increases, although most MXenes have a very low surface area (66 $m^2\ g^{-1}$ for titanium carbides or 19 $m^2\ g^{-1}$ in the case of V_2CT_x), which is lower than the theoretical values (for example, 496 $m^2\ g^{-1}$ for $Ti_3C_2T_X$) [178].

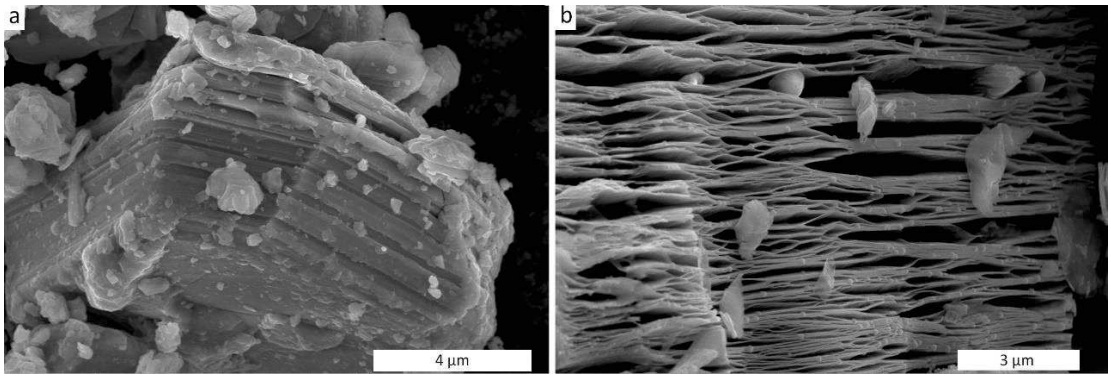

Figure 18. SEM of a MAX phase (a) and the resulted MXene (b) by HF treatment.

Another mild approach to preparing MXene is treating the MAX phase with a mixture of concentrated HCl and lithium fluoride salt. Formation of HF after 20 min of mixing results in the cleavage of the aluminum layer. Besides the acidic media, the exfoliation of the MAX phase is carried out in concentrated basic solutions such as KOH, NaOH, and NH_4Cl. The surface functional groups can be optimized by selecting the proper etchant. Yoon *et al.* used 6M KOH at a high temperature and pressure for the Al etching [179]. After 24 h of hydrothermal treatment, $Ti_3C_2T_X$ with a surface covered by oxygen and hydroxide functionalities was obtained. Interestingly, the aluminum content after the etching process was considerably decreased, which was comparable to that of acid-treated MXenes. Zhang and his coworkers prepared a fluorine-free titanium carbide with high quality by NaOH treatment. Under different temperatures, the MAX phase showed an exfoliation to some extent. An effective removal of aluminum with a high efficiency was obtained by applying thermal treatments up to 270 °C. Furthermore, the electrochemical performance of the prepared MXene was analyzed in a symmetric EC cell. From the CV analysis in 1M H_2SO_4, a gravimetric capacitance of 314 F g^{-1} at 2 mV s^{-1} was recorded. Comparing voltammograms of HF and NaOH-treated MAX phases (Figure 19), different interactions are involved in charge storage of these two samples.

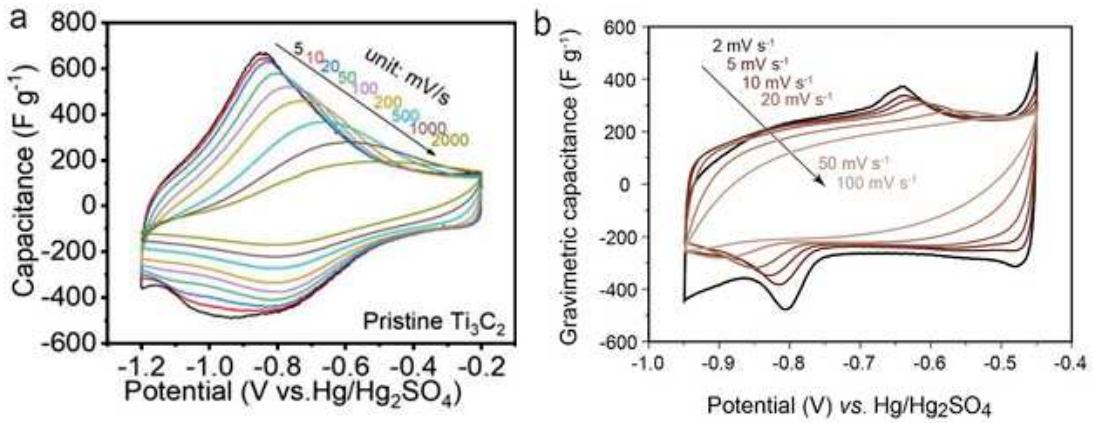

Figure 19. The electrochemical performance of $Ti_3C_2T_x$ synthesized from treating the MAX phase by HF (a) and NaOH (b) [180].

The prepared titanium carbides in acidic media showed a substantially higher hydrogen storage ability, which is visible as a pair of redox couple at around 0.6-0.8 V

vs. Hg/Hg_2SO_4 (Figure 19a) [180]. On the other hand, the prepared sample by the NaOH treatment presented a lower faradaic response. However, the power performance of cells was comparable (Figure 19b). In general, structural and chemical differences, in particular the type of functional groups with which the surface of the outer layered is covered, can be taken as a reason for such variation in charge storage.

In another study, a mixture of diluted ammonium chloride (1M) and tetramethylammonium hydroxide (0.2M) was employed for preparing single-layer $Ti_3C_2T_x$ from its MAX phase [181]. Compared to acidic etching, in general, alkaline-based aluminum removal results in a bigger expansion between MXene layers, and usually, a higher gravimetric capacitance can be obtained [182]. Recently, solid solution-based approaches have been employed to prepare MXenes. These approaches are of interest, especially for being environmentally friendly compared to wet chemical acidic routes and for having better control over the functional groups at the MXene surface. Gogotsi *et al.* reported the preparation of layered titanium nitride ($Ti_4N_3T_x$) from its parent phase, using a one-step thermal treatment (550 °C) under inert gas at the presence of a mixture of fluorine based salts such as KF, NaF, and LiF [183]. Few-layered particles were further delaminated by sonication in a tetrabutylammonium hydroxide solution. Interestingly, analysis revealed that the surface of the sample is covered mainly by oxygen (more energetically favorable) rather than fluorine or hydroxide functionalities. Simon *et al.* used the same approach in the presence of chlorine-based salts to etch the titanium aluminum carbide [184]. For this purpose, a compact tablet was made of MAX phase in combination with a eutectic salt, including NaCl and KCl. No inert atmosphere was used and to prevent the resulted MXene from oxidation, the prepared tablet was sealed and covered with a high amount of $ZnCl_2$ during the reaction. The assembled half Li cell based on this sample showed a pseudocapacitive insertion response in a wide potential range and a high discharge capacity around 300 mAh g^{-1} at the current density of 0.1 A g^{-1} was obtained. However, the power performance of the cell was limited in organic electrolytes. To solve this problem, Gogotsi *et al.* was used polystyrene (PS) spheres for the preparation of porous titanium carbide [185]. A colloidal dispersion of few-layer

titanium carbide and PS spheres was taken under the sonication. Afterward, the supernatant was vacuum filtered, and the remained film was peeled off from the filter paper. To remove the template, the sample was annealed at 450 °C under an inert gas. The remained free-standing film was assembled into a three-electrode cell. 1M LiTFSI dissolved in different organic solvents, including carbonates, acetonitrile, and dimethyl sulfoxide, and they were used as the electrolyte. During cycling between 0 to -2.5V *vs.* Ag wire, the electrode showed a good power response by increasing the CV scan rate from 2 to 1000 mV s^{-1}. Besides the aforementioned routes, other approaches including, microwave synthesis, chemical or physical vapor deposition [186-187], spark-plasma sintering [188], and sol-gel methods [189] have been employed for the preparation of MXenes. In some cases, adopting these procedures may result in defect-free MXene layers, in contrast to the wet chemical process.

MXenes store energy by a combination of EDL and hydrogen storage. Nevertheless, there is a lack of explanation about the interactions or, in general, the chemistry behind the energy storage performance of MXenes. Most of the reported investigations, if not all, have presented the electrochemical performance of titanium carbide and other MXenes as a single electrode in a limited potential range (Figure 19). Hence, the performance of full EC cell built from MXene-based electrodes was remained unaddressed.

A thorough investigation targeting fundamental aspects of charge storage in MXenes is presented in the second chapter of this dissertation (Article 3 and Article 4). For this purpose, Titanium Carbide ($Ti_3C_2T_x$) and Molybdenum Titanium Carbide ($Mo_2Ti_2C_3T_x$) were prepared by two different etchants (HF and HCl/LiF) from MAX phases. Electrochemical investigations were carried out in aqueous media (H_2SO_4, Li_2SO_4, $BeSO_4$, KOH) (Article 3) and ionic liquids ([EMIm][TFSI], [BMP][TFSI], [C3mpyr][FSI] (Article 4).

2.4. Electrolytes for electrochemical capacitors

The interaction of electrolyte ions and the surface of electrode materials plays a significant role in the electrochemical performance of ECs. Generally, electrolytes can

be categorized based on their physical state which are aqueous, organic, ionic liquids, and solid-state. Depending on their chemical and physical properties, each category shows promise in designing electrochemical capacitors with a specific electrochemical energy and power response.

2.4.1. Aqueous electrolytes

The properties of aqueous electrolytes are significantly governed by the polarity of the solvents in which the salt is dissolved. These media offer excellent ionic conductivity due to their low viscosity, which makes them a perfect candidate for high-power applications. On the other hand, their stability is considerably limited by the decomposition of water, and therefore, they have a relatively narrow theoretical working voltage range (1.23 V). During the negative polarization, aqueous solvents are decomposed and hydrogen molecules are released. The positive polarization beyond the theoretical line leads to the formation of oxygen molecules. An effective approach for mitigating such drawback is reducing the amount of the water molecules inside the electrolyte. Increasing the concentration of salts, water molecules are tightly surrounded by ions, and therefore, the solvent shows higher stability against catalytic decomposition. For high energy density aqueous-based applications, “water-in-salt” electrolytes improve voltage stability of ECs beyond 2V. However, having a lower ionic conductivity in this case is inevitable. In most cases, aqueous electrolytes are environmental friendly, cheap, and they require no inert atmosphere for handling or doing the cell assembly. For long-term cycling, however, aqueous electrolytes are not in favor, as they reduce the stability of the cell due to the parasitic reactions. In particular, the cycle life declines and self-discharge of ECs increases. Aqueous electrolytes can be categorized based on their pH. Acidic electrolytes such as H_2SO_4 are highly conductive (0.8 S cm^{-1} at room temperature) [190]. The conductivity of an electrolyte depends on its concentration. In the case of sulfuric acid, a 1M solution provides the highest ionic mobility, which is greater than that of neutral media. For the cell assembly, however, current collectors based on noble metals such as platinum or gold are required. Alkaline electrolytes such as KOH with a proper concentration (6M)

can offer a superior ionic conductivity, as well. Interestingly, they have no corrosive effect on typical current collectors such as stainless steel. Similarly to highly acidic media, EC-based alkaline media usually offer a high capacitance but in a narrow voltage range. Neutral aqueous electrolytes, e.g., Li_2SO_4, $NaNO_3$, are more attractive than acidic or basic media due to their higher electrochemical stability up to 1.8V. Redox-active electrolytes are used to improve the energy density of ECs. The added faradaic activity may degrade some important parameters including the cyclic stability of the cell. However, such faradaic reactions that usually are localized within a specific potential range of one electrode, can be used as an effective strategy for regulating the charge balance between the negative and positive electrodes.

2.4.2. Organic electrolytes

Organic solvents provides a wide voltage stability (up to 2.6V) and a long cycle life as their performance is not affected by parasitic reactions. These factors make organic electrolytes a good option from the industrial point of view. Nevertheless, the high viscosity of organic electrolytes reduces their conductivity, and therefore, the charge storage performance, and importantly, the power rate of the cell diminishes. Besides being expensive, their flammability and toxicity raise much concerns for the environment. They are expensive, as inert atmosphere and special equipment for drying and storage as well as cell assembly are required.

2.4.3. Ionic Liquids

Ionic liquids (ILs) can be defined as organic salts composed of cations and anions with a low melting point (around 100 °C). Basically, the big dimension of cations results in inefficient packing of ions in the structure which results in decreasing the melting temperature of ionic liquids [191]. Room temperature ionic liquids are a category of this family which can remain in the liquid form at ambient conditions. ILs are environmentally friendly, nonvolatile, and air/water stable, which makes them a promising candidate for different applications such as energy storage. In contrast to two aforementioned category of electrolytes, there is no solvent in the composition of

ionic liquids (ILs), which brings both positive and negative features for this class of electrolytes. ILs can be categorized further into two main groups, including protic and aprotic. The most important characteristic of ILs is their superior electrochemical stability (lack of solvent decomposition), which allows them to operate in a wide range of voltage (up to 3V). Due to the very high decomposition temperature, around 300 °C, ILs based ECs can be employed for a wide range of temperature for sensitive energy storage applications. Versatility in term of ionic size, the charge storage behavior of ECs can be optimized by selecting proper ILs. IL-based ECs show a superior cycle life performance in the absence of susceptible solvents. Nevertheless, their high viscosity results in a poor ionic conductivity (a few mS/cm) as well as limited power performance. Noteworthy, the conductivity of ILs is related to more than sole viscosity, because other parameters such as charge delocalization and density are involved. For example, [EMIm][BF_4] has a viscosity equivalent to η = 41.2 mPa, which is higher than that of [EMIm][TFSI]. However, [EMIm][BF_4] shows a higher conductivity.

2.5. Electrochemical cells

In this thesis, three different cells have been used for the purpose of electrochemical characterizations. The first one is named Swagelok® cell, which is designed in a two-electrode symmetric system with the possibility of connecting the reference electrode for three-electrode cell experiments. Figure 20a represents the schematic of this cell, which is made of two current collectors from stainless steel or titanium/gold for the sake of running experiments in neutral/basic or acidic media, respectively. The main body of the cell is made of PTFE (Teflon) to prevent from the short circuit between electrodes. In this configuration, electrode materials usually are cut in a round shape with a diameter of ≤ 10 mm. A microfiber cellulose paper (GFD, Whatman GmbH) with a 12 mm diameter was used as the separator to prevent from the contact between electrodes. The amount of injected electrolyte was around a few hundred microliters (**Article 1, 2, and 3**).

Another cell that was employed for evaluation of electrode materials in ionic liquids (**Article 4**) is named ECC-Ref cell from EL-CELL GmbH, which can be used in both two

and three-electrode fashion (Figure 20b). For this purpose, electrodes with a diameter of 16 mm were used in a symmetric way, where two cellulose papers (GFA, Whatman GmbH) with an 18 mm diameter served as the separator. A 700 microliters portion of different ILs was used as the electrolyte for these investigations. For three-electrode experiments, a small piece of carbon was used as the reference electrode. Finally, a dilatometer cell named ECD-3-nano from EL-CELL GmbH was employed to track the *operando* volumetric expansion of electrodes in ILs (**Article 4**). The dilatometer cell (Figure 20c) was assembled in a three-electrode configuration, where an oversized counter electrode is placed against the working electrode (10 mm diameter, 120 µm thickness). A small piece of carbon electrode was used as the reference electrode in these studies. The cell is equipped with a sensor to measure displacement in the z direction within the electrode structure.

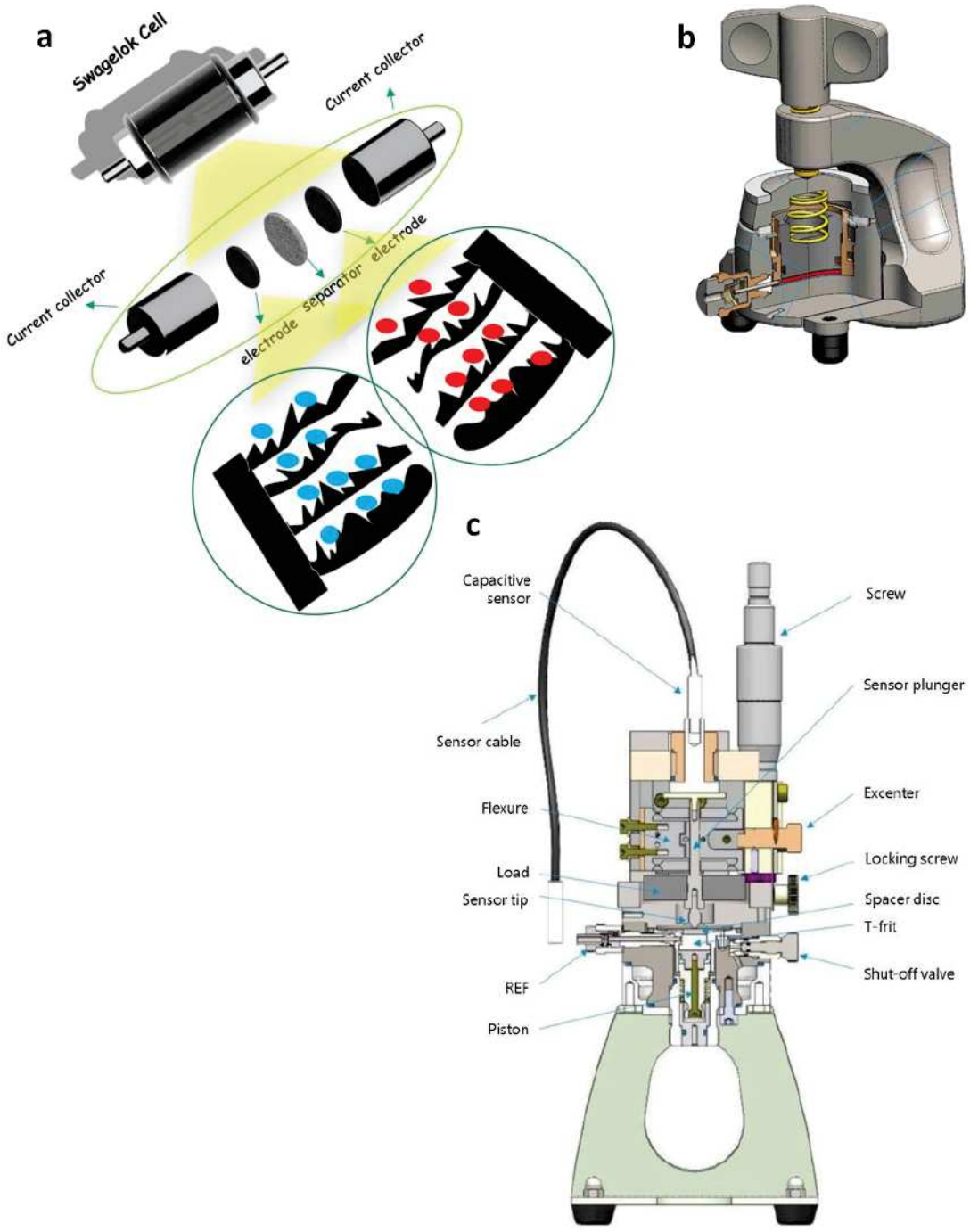

Figure 20. Schematic representation of the electrochemical cells that were employed in this dissertation, including Swagelok® (a), ECC-Ref (b), and dilatometer ECD-3-nano (c) cells.

2.6. Electrochemical techniques

Cyclic voltammetry (CV), Electrochemical Impedance Spectroscopy (EIS), Galvanostatic charge-discharge (GCD), are three main techniques that were employed for the electrochemical investigations in this dissertation.

2.6.1. Cyclic Voltammetry

In CV experiment of two-electrode or three-electrode configuration, the variation of current against voltage/potential is recorded at constant scan rate. Based on the shape of the obtained profile, important information about charge storage behavior of a single electrode or a cell is accessible. For instance, an ideal electrochemical capacitor should be characterized by a rectangular shape voltammogram and be able to preserve its rectangular response by increasing the scan rate during charge and discharge of the cell. Applying high scan rates in a CV experiment allows us to detect the capability of an EC for a stable energy storage response even at high charge/discharge kinetics. The electrochemical behavior of single electrodes can be monitored exclusively by switching from two-electrode to three-electrode configuration. For this purpose, CV measurements can be used to determine the charge storage as well as the limits of stable working potential of electrodes. Finally, differentiating between the proportion of capacitive and faradaic currents is doable by running CV analysis at different scan rates.

2.6.2. Electrochemical Impedance Spectroscopy (EIS)

The EIS method provides important information regarding the resistivity and conductivity of an electrode material or a cell. Evaluation of electrochemical responses in a broad range of time from microseconds to hours allows us to make a separation between various charge storage processes based on their time constant. This technique can be performed either by controlling the voltage or current. For instance, a sinusoidal signal with a small amplitude is carried out at different frequencies, while

the voltage of the system is fixed. Then, a profile, called Nyquist plot is obtained. The intersection of profile with the X axis reveals the Electrical Series Resistance (ESR) of the cell. This parameter represents the resistance that exist within the bulk of the electrolyte medium. The EIS plot of an ideal EC is characterized by a vertical line, although in practice there is a semi-circle part, which indicates charge transfer resistance (R_{ct}). The last element provides information about the resistivity of the cell *versus* ionic diffusion, which can be interpreted based on the angle of the observed vertical line after the semi-circle part. This part which is also called Warburg diffusion usually has an angle close to 90^{o} in ECs. Another important data which can be extracted indirectly from the EIS spectra is the relation between the capacitive responses *versus* the applied frequency of the cell. An ideal EC usually shows the same capacitive response in wide frequency range.

2.6.3. Galvanostatic Charge-discharge (GCD)

This technique is considered as the main evaluation experiment for targeting energy and power outputs as well as long term stability of an EC cell. Generally, the variation of voltage/potential *versus* the time, under a specific applied current, results in a profile with a triangular shape for an ideal EC. In comparison with CV, this analysis provides a more reliable information related to the practical working voltage of a cell. Usually the performance of electrochemical cell is affected by a resistance called ohmic drop or IR drop. As this parameter can be easily distinguished in a GCD profile, the correct working voltage range of a system should be selected for calculation energy/power of EC. Similar to the CV experiment, applying high current densities in a GCD measurement allows us to determine the stability of cell. The cycle life of cell is mainly determined by GCD test. For this purpose, the cell faces continuous and repetitive charge-discharge cycles in a designated working voltage until its capacitance drops by 20% with respect to the value from the initial cycle. The cyclability of a cell can also be evaluated by a technique called floating (accelerated ageing).

Chapter 2

Experimental work

3. Article 1

Title: ***Electrochemical Capacitor Performance of Nanotextured Carbon/Transition Metal Dichalcogenides Composites***

Authors: Elżbieta Frąckowiak*, Masoud Foroutan Koudahi, Maciej Tobis

Journal: Small

DOI: https://doi.org/10.1002/smll.202006821

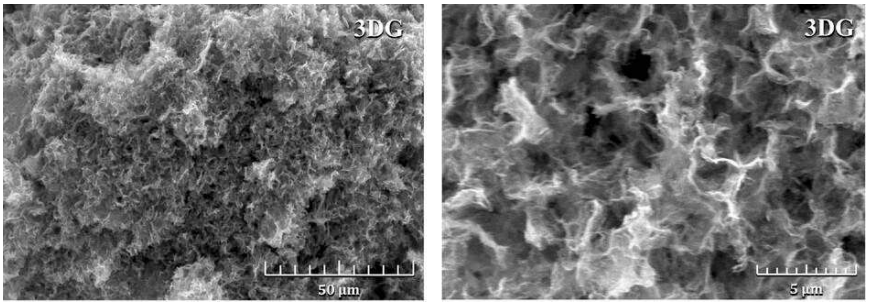

Motivation

Integrating carbon substrates and redox-active materials is an interesting approach for enhancing both energy and power density of ECs in aqueous media. Based on the electrochemical response of the active material, a carbon can play a role as either the substrate or the conductive additive. In the case of highly conductive TMDs with a box-like CV profile, it is possible to increase the loading of redox-active materials and employ carbons only as the conductive agent.

The main goal of this article was to improve the electrochemical performance of TMD-based ECs by designing electrode materials with a wide working potential and fast frequency response. Various composite electrodes based on different TMDs (FeS_2, ReS_2) and carbons (3DG, CNTs) were prepared. To optimize the proportion of TMD-to-carbon, hybrid electrodes based on interconnected porous 3DG and FeS_2 with 5, 10,

15, and 20 wt% were prepared using a one-step hydrothermal reaction. Successful preparation of composites was confirmed using XRD analysis. SEM studies revealed that the surface accessibility of 3DG strongly depends on the amount of the deposited TMD. Loading up to 15 wt% FeS_2 does not have a significant impact on the porosity of 3DG (no significant agglomeration was detected), while further deposition results in blockage of micropores. The electrochemical performance of composites was studied both as the single electrode and in a full EC cell. 1M NaSO4 was used as the electrolyte. Comparing the CV response of the symmetric cells based on composites showed that increasing the loading of FeS_2 to 15% results in an improvement in the energy storage. However, 3DG-20 wt% FeS_2 presented a limited charge response.

Furthermore, the cell based on 3DG-20 wt% FeS_2 (the optimal sample) demonstrated a wide working voltage (1.5V), indicating its potential for further investigation. Three-electrode cell characterization revealed the relatively low catalytic activity of FeS_2 for hydrogen evolution, as the electrode can operate well below the theoretical HER value. On the other hand, the positive electrode was polarized no further than the theoretical O_2 line. This finding has significant implications for the design of TMD-based ECs, it suggests that FeS_2 can be used to enhance the energy storage of ECs with the neutral aqueous electrolyte. Another key factor is the roughness of electrode materials, which can accelerate the rate of catalytic water decomposition.

The power response of cells was determined by EIS analysis, in which their charge storage was monitored in a broad frequency range from 100 kHz to 1mHz. The EC cell based on 3DG presented better frequency response than 3DG-15 wt% FeS_2. CV and GCD results agreed with the EIS data, as the charge storage of EC based on this composite showed a decline by increasing the scan rate to 100 mV s^{-1} or the current density to 2 A g^{-1}. However, the cell exhibited good cyclability maintaining 80% of its initial capacitance up to 8000 cycles.

Another reason for conducting this study was to evaluate the effect of morphology and structural defects on the charge storage of TMDs. Materials with high roughness and defect-rich surface degrades the working voltage of the cell by promoting the rate of catalytic water decomposition.

FULL PAPER

NANO · MICRO small
www.small-journal.com

Electrochemical Capacitor Performance of Nanotextured Carbon/Transition Metal Dichalcogenides Composites

Elżbieta Frąckowiak, Masoud Foroutan Koudahi, and Maciej Tobis*

Transition metal dichalcogenides (TMDs) are emerging low-dimensional materials with potential applications for electrochemical capacitors (EC). Here, physicochemical and electrochemical characterizations of carbon composites with two sulfides ReS_2 and FeS_2 are reported. To enhance conductivity, multiwalled carbon nanotubes (NTs) serve as a support for ReS_2 while 3D graphene-like network (3DG) is utilized for FeS_2 deposition. Unique structure of carbon/TMDs composites allows a faradaic contribution of sulfides to be exploited. Capacitance values, charge/discharge efficiency, capacitance retention, charge propagation, cyclabilty, and voltage limits of EC with carbon/sulfide composites in aqueous neutral solutions (Li_2SO_4, Na_2SO_4) are analyzed. Special attention is devoted to energetic efficiency of capacitive charge/discharge processes. Structure-to-capacitance correlation for the composites with various TMDs loading is thoroughly emphasized. The more defected structure of layered NTs/ReS_2 composite is responsible for the lower capacitor voltage (0.8 V) owing to quicker electrolyte decomposition. Additionally, the catalytic effect of Re for hydrogen evolution reaction plays a crucial role in EC voltage restriction. Contrary, the operating voltage of capacitor based on 3DG/FeS_2 is able to be extended until 1.5 V in sodium sulfate electrolytic solution.

1. Introduction

Electrochemical capacitors (ECs) are high-power energy storage devices that are expected to play a significant role in various future applications, for example, electrical cars, shuttles, cell phones, or power plants. It is worth noting that EC escape battery safety and disposal issues. The energy storage in ECs occurs mainly through the electrostatic accumulation of charges at the electrode/electrolyte interface, hence, it is required that the electrode materials should possess a developed specific surface area and high conductivity.[1–3] Many representatives of carbons such as activated carbon, carbon fibers, carbon NT/composites, or graphene fit those characteristics and are mostly used in ECs. However, they offer moderate capacitance due to the limited specific surface area and non-uniformly distributed pores which hinder the accessibility of the vacant sites for ions. Therefore, more efforts are directed into developing new composites with redox phenomena which will meet the requirements of high energy and power density as well as high cyclability.[4–6] 2D transition metal dichalcogenides (2D-TMDs) are promising candidates due to their layered structure, a large variety of metal-dichalcogenide combinations, and exposed active sites.[7–12] Yet, they offer moderate conductivity and stability which limits their application in long-term operating devices. So far, molybdenum disulfide (MoS_2) and tungsten disulfide (WS_2) are the most often reported as EC electrode materials.[13–15] Application of carbon materials as a conducting substrate for TMDs is indispensable. Deposition of a thin layer of TMDs on carbon scaffold (e.g., carbon nanotubes (NTs), graphene) improves not only the power rate but also capacitive behavior of the composite. For example, electrode based on MoS_2-carbon nanoplates have been prepared by hydrothermal-calcination method and symmetric capacitor cell with such composite demonstrated a specific capacitance of 248 F g^{-1} at a current density of 0.1 A g^{-1}.[16] Moreover, the aforementioned electrode showed a fast response, that is, even at high scan rate of 300 mV s^{-1} the electrode preserved its rectangular shape. In another study, Chen et al. designed a composite based on carbonaceous materials such as CNTs, graphene, and carbon black as the substrate and MoS_2 as the redox active material. Among the synthesized electrodes, CNTs/MoS_2 showed a high specific capacitance of 402 F g^{-1} at a current density of 1 A g^{-1}. Also, this electrode exhibited a good cyclability by maintaining nearly 80% of its initial capacitance after continuous 10 000 charge–discharge cycles at a current density of 1 A g^{-1}.[17] WS_2/composites have been widely investigated in EC application. For instance, Rout et al. tailored a hybrid electrode based on reduced graphene oxide (GO) and WS_2 through one-step hydrothermal procedure. A high specific capacitance of 350 Fg^{-1} was achieved at a scan rate of 2 mV s^{-1}.[18] Additionally, other types of TMDCs such as CoS_2,[19] SnS_2,[20] and VS_2[14] were utilized for EC application. For example, Jun et al. synthesized electrode materials based on CoS_2 deposited on S and N co-doped nanosheets and such electrodes delivered a high specific capacitance of 283 F g^{-1} at a current density of 1 A g^{-1}. Furthermore, this

Prof. E. Frąckowiak, M. Foroutan Koudahi, M. Tobis
Institute of Chemistry and Technical Electrochemistry
Poznan University of Technology
Poznan 60965, Poland
E-mail: elzbieta.frackowiak@put.poznan.pl

The ORCID identification number(s) for the author(s) of this article can be found under https://doi.org/10.1002/smll.202006821.

© 2021 The Authors. Small published by Wiley-VCH GmbH. This is an open access article under the terms of the Creative Commons Attribution License, which permits use, distribution and reproduction in any medium, provided the original work is properly cited.

DOI: 10.1002/smll.202006821

ADVANCED SCIENCE NEWS
www.advancedsciencenews.com

NANO · MICRO small
www.small-journal.com

electrode showed no capacitance decrease after 5000 cycles of constant charge–discharge at a high current density of 20 A g^{-1} which indicates its favorable stability at harsh conditions.

Even if in the literature cited above, the high capacitance values are indicated, very often only cyclic voltammetry (CV) results in a three-electrode cell are shown without comparison to galvanostatic data from a two-electrode cell (real system). Additionally, capacitance values are frequently calculated taking only Coulombic efficiency (discharge time) but not energetic efficiency where capacitance is estimated from integrating the galvanostatic discharge curve. Especially if discharge curve is concave, the capacitance value calculated from discharging time is highly overstated. Some studies are performed with the electrode mass below or equal to 1 mg what is practically not applicable, long-term cycling by CV in a three-electrode cell has no sense as well. Hence, the critical point of view is necessary during literature analysis.

Aside from the most popular TMDs mentioned, rhenium disulfide (ReS_2), which has rarely been explored in the case of energy storage devices has recently gained significant attention in metal-ion batteries (MIBs).[21–23] ReS_2 is popular in MIBs due to similar interlayer spacing to MoS_2 (0.614 to 0.615 nm) and more than 25 times weaker interlayer energy coupling.[24] However, in the case of EC, it has been never reported.

Here, the original composites with a various proportion of multiwalled carbon NTs and ReS_2 have been prepared by hydrothermal method to study capacitor performance. Additionally, novel material based on 3D graphene network (3DG) like structure as a matrix for iron sulfide has been designed. Interestingly both carbon networks (CNTs and 3DG) are characterized by different structure/texture, hence, composites supplied distinct electrochemical performance. The target of this research is to synthesize the composites which show synergistic properties of both materials, that is, carbons and TMDs, to exploit their electrochemical performance, conductivity, and unique structure. The reason of different operating voltage limits for both composites has been revealed. Voltage range, in turn, is an important metric that affects the energy of capacitor device.

2. Results and Discussion

Low-dimensional materials such as graphene and TMDs have been under significant consideration as novel materials for the ECs. Herein, we report on the hydrothermal synthesis of composites based on rhenium disulfide with multiwalled carbon NTs and iron disulfide with 3DG. The scheme of TMD/carbon composite preparation via a hydrothermal synthesis is presented in **Figure 1**, where carbon NTs and 3DG materials play a scaffold role for deposition of Fe and Re sulfides.

First, different proportions of NTs and Re sulfide in composite were studied to find the optimal composition. It is well known that carbon NTs, as highly mesoporous material, provide negligible capacitance (a few F g^{-1}); generally the more pure and well organized structure of NTs, the lower capacitance values.[25,26] Hence, the very moderate amount of NTs (7 wt%) was the most beneficial. In fact, ReS_2 was the main component (93 wt%) in this composite. Mesoporous character of the nanotextured ReS_2/7 wt% NTs and NTs was proven by N_2 adsorption/desorption. Figure S1, Supporting Information presents the isotherms and inset with a pore size distribution. Isotherms show a steep increase of N_2 adsorbed at low relative pressure exhibiting limited presence of micropores and a peak at high relative pressure region indicating presence of bigger pores. During desorption a significant hysteresis is observed. Type IV isotherms demonstrate clearly a mesoporous character of both materials. The volume of N_2 adsorbed/desorbed by ReS_2/7 wt% NTs is significantly lower than for the pure NTs. It means that the deposited TMD layers have decreased the overall surface area mainly in the range of mesopores. Specific surface area and porosity features are compiled in Table S1, Supporting Information.

The distribution of elements and the morphology/texture of such composite (**Figure 2**) was studied by scanning electron microscopy (SEM) combined with energy dispersive spectroscopy (EDS).

The SEM images with different scales show that the composite exhibits derivative morphological shape to the NTs with

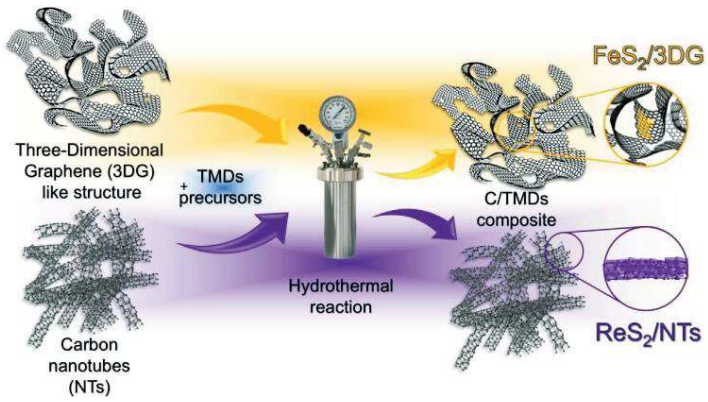

Figure 1. The simplified scheme of synthesis for two different composites: 3DG/FeS_2 and CNTs/ReS_2.

 © 2021 The Authors. Small published by Wiley-VCH GmbH

ADVANCED SCIENCE NEWS
www.advancedsciencenews.com

NANO · MICRO small
www.small-journal.com

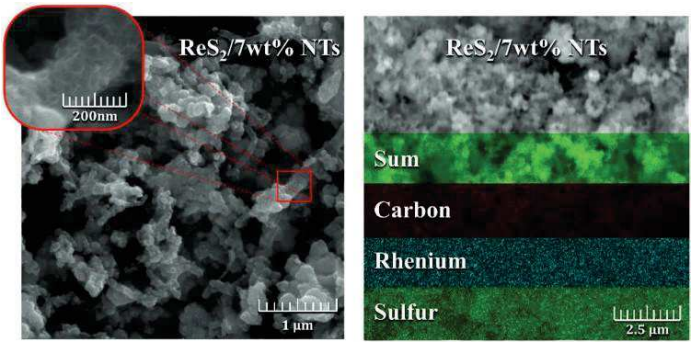

Figure 2. SEM images (left) and EDS mapping (right) of ReS_2/7 wt% NTs composite.

cauliflower-like structure. However, at high magnification the perpendicular flakes with exposed edges are well visible. EDS mapping shows that the individual atoms of ReS_2 are well distributed on the surface of the NTs, it means that the carbon NTs are firmly covered by ReS_2 layers. During the synthesis of the composite, ReS_2 layers are being formed on the surface of the NTs favorably at the structural defect sites. Typically, during deposition process the defect sites play a nucleation role. This unique morphology allows the electrolyte to penetrate through the whole electrode. Thus, the dense layered structure creates many active sites for ions to be freely adsorbed and desorbed during ECs charge/discharge. Generally, the layers can be directed perpendicularly or parallel to the NTs plane.[27] In this case, due to the low controllability of the hydrothermal synthesis process the layers are distributed randomly and most likely vertically to the NTs surface as it can be observed in the inset of Figure 2.

To analyze the crystal structure of the powdered materials, both samples (ReS_2 and ReS_2/7 wt% NTs composite) were investigated by the X-ray diffraction (XRD) technique. As shown in the **Figure 3**, peaks at 14.5°, 32.5°, 43.5°, and 60.9° (2θ) are

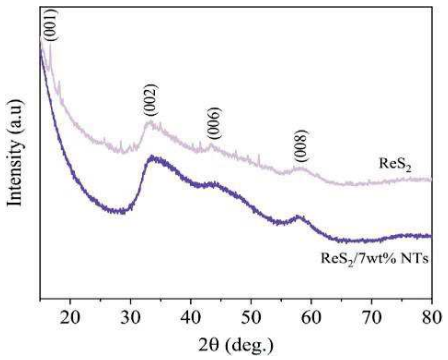

Figure 3. XRD diffractograms for ReS_2 and ReS_2/7 wt% NTs composite.

observed and can be attributed to ReS_2 (JCPDS # 00-063-0205) namely (100), (002), (006), and (008) planes, respectively. The lack of intense peak confirms the disordered layered structure of the composite.

After a detailed physicochemical characterization, synthesized materials were successfully employed as electrodes in electrochemical capacitor (EC) cells and investigated by CV, galvanostatic charge/discharge with potential limitation (GCPL), and electrochemical impedance spectroscopy (EIS). For the two-electrode electrochemical investigations, Swagelok cell with two stainless steel pistons was used. Two separated electrodes of similar mass were soaked with 1 mol L^{-1} Li_2SO_4 electrolyte. Detailed investigation of the individual electrodes was performed utilizing a cell combined additionally with Hg/Hg_2SO_4 reference electrode.

Deposited ReS_2 onto carbonaceous materials improved the overall performance of the assembled EC system due to the exhibition of faradaic reactions. Cells prepared with ReS_2/7 wt% NTs demonstrated a capacitance of 108 F g^{-1} (**Figure 4**). For comparison, the cells with pure carbon materials (NTs) were also investigated.

The performances of the ECs cells were evaluated accordingly to the very well-known methodology.[28] At the beginning, the symmetrical cell assembled with ReS_2/7 wt% NTs was studied by CV. The window voltage was extended by 0.1 V beginning from 0.5 V with the 1 mV s^{-1} sweeping rate (Figure 4a). The performance of the full cell with the separate behavior of positive and negative electrodes is presented in Figure 4b. It can be observed that at low scan rates the electrodes exhibit nearly rectangular square shape which is characteristic for the capacitive behavior of electric double-layer capacitors. Further voltage extension shows no faradaic contribution until 0.8 V where the characteristic peaks, which can be attributed to oxygen and hydrogen evolution are appearing on the positive and the negative electrode, respectively. While it is understandable that the oxygen evolution appears close to the calculated potential value for the water decomposition, the hydrogen evolution limit is much further from what is observed experimentally. Layered ReS_2 and most of other representatives of 2D-TMDs family, are consisting of inert basal plane and active edge sites.[29–31] TMDs

 © 2021 The Authors. Small published by Wiley-VCH GmbH

ADVANCED SCIENCE NEWS
www.advancedsciencenews.com

NANO · MICRO small
www.small-journal.com

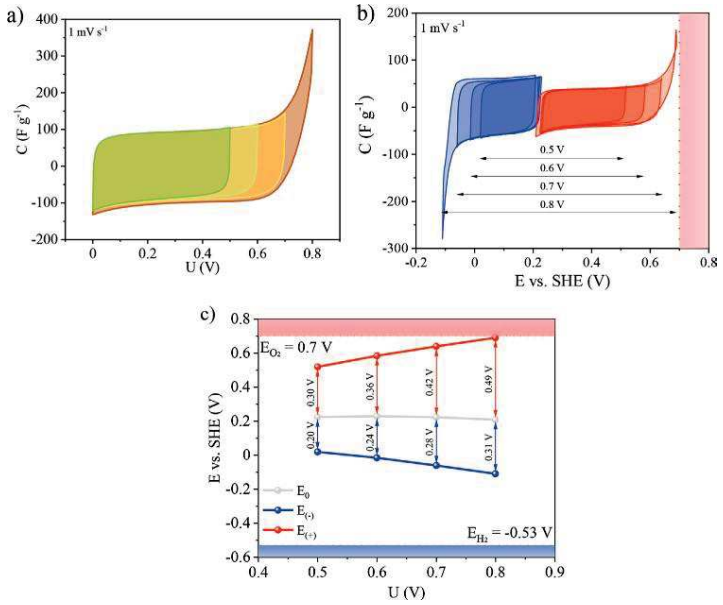

Figure 4. a) Electrochemical characterization of symmetric EC with ReS_2/7 wt% NTs by cyclic voltammetry (1 mV s^{-1}) with a gradual voltage extension. b) Electrochemical behavior of individual electrodes is depicted, c) with the thermodynamic limit of O_2 and H_2 evolution. Electrolyte—1 mol L^{-1} Li_2SO_4.

will promote hydrogen evolution, dependent on the amount of edge site exposed.[32–33] Additionally, Figure 4c shows that the positive electrode works on a wider potential window than the negative one. From characteristics of the negative electrode, it looks that the hydrogen storage does not proceed at all, just contrary this material has a tendency to catalyze hydrogen evolution reaction (HER) during the voltage extension. It should be considered that the NTs as typical mesoporous material cannot store hydrogen, additionally NTs amount is very low. On the other hand, hydrogen evolution is governed by a balance between the surface coverage and reactivity illustrated by the so called volcano plot, that is, M—H bond strength versus log i_0 (exchange current). Re as metal occurs close to noble metals (Pt, Pd) which greatly catalyze HER. Due to the high evolution peaks indicating oxygen and hydrogen evolution at higher voltage, it was decided to perform other electrochemical investigations at 0.8 V.

The voltammetry characteristics of cells assembled with ReS_2/7 wt% NTs at various scan rate from 2 to 200 mVs^{-1} are shown in **Figure 5**a. The rectangular shape of the voltammograms at all sweeping rates indicates the capacitive behavior of the electrodes. Thanks to the intimate interconnection of the ReS_2 nanolayers to the NTs, the composite electrode exhibits higher conductivity from NTs and increased capacitance due to the TMD presence as well as because of the higher specific surface area of composite. It can be stated that the composite possesses the intermediate properties to the parent materials. NTs significantly improve the charge propagation of the electrode. GCPL characteristics for the cells with ReS_2/7 wt% NTs limited to 0.8 V at different current loading from 0.2 to 2 Ag^{-1} are shown in Figure 5b. The curves represent close to ideal triangular lines which are associated with capacitive behavior. The integrated capacitance values for ReS_2/7 wt% are 108, 94, 82, and 73 F g^{-1} at 0.2, 0.5, 1, and 2 A g^{-1}, accordingly.

The same voltammetry test was conducted for the cell with pure ReS_2 (Figure S2, Supporting Information). The ReS_2 alone showed a high capacitance but with much lower charge propagation and inferior conductivity. Cell with ReS_2 comparably to composite shows nearly squared shape profile but only at lower scan rates. At higher sweeping rates, the voltammograms lose the squared shape because of the diffusion limits. The EC in both cases (ReS_2 and ReS_2/NTs) did not show redox peaks. It is well known that some electrochemically active materials do not show redox peaks (e.g., ruthenium oxide, nitrogenated carbons). Hence, in that case, the faradaic reactions of TMD should not be excluded. The following reaction can be considered: $ReS_2 + Li^+ + e^- \leftrightarrow ReS - SLi$

EIS is very valuable, complementary technique for capacitor investigation. Nyquist plots and the analog circuit diagrams for capacitor built with all materials, that is, NTs, ReS_2, and ReS_2/7 wt% are presented in Figure S3, Supporting Information. EIS results were measured within the frequency range of 1 mHz–10 kHz. Pure NTs in comparison to composites showed significantly smaller capacitance but exhibited superior charge propagation and great conductivity. The capacitor working with NTs exhibited

 © 2021 The Authors. Small published by Wiley-VCH GmbH

ADVANCED SCIENCE NEWS
www.advancedsciencenews.com

NANO · MICRO small
www.small-journal.com

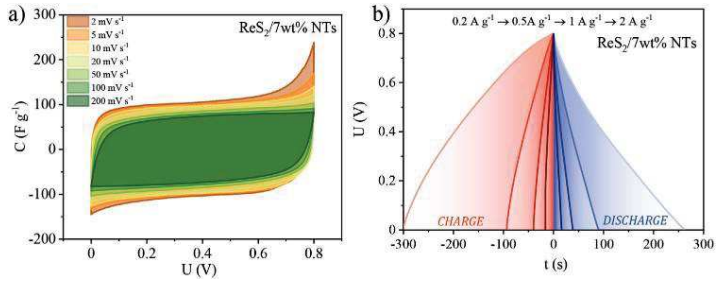

Figure 5. a) Voltammetry and b) galvanostatic characteristics for the capacitor built from ReS_2/7 wt% NTs composite. Electrolyte—1 mol L^{-1} Li_2SO_4.

negligible values of ESR and EDR (0.77 and 1.58 Ohms). The imaginary part of the impedance characteristics grows in parallel to the *y*-axis meaning that there is no effect of redox reactions especially for NTs. However, for the composite clear diffusion limitation is observed. In case of the cell constructed with ReS_2/7 wt% NTs, the system showed comparable values of ESR and an increase of EDR value (0.8 and 8.2 Ohms, respectively). Such an increase in resistance of the cell comes from the addition of ReS_2 to the composite material. Also, the shape of the impedance curve is no longer parallel to the *y*-axis. Cell assembled with ReS_2 exhibited distinct semi-circle due to the redox reactions and lower conductivity of the material. Charge propagation is an important EC metric. EIS technique is perfectly adapted for monitoring this property. In addition to Nyquist plots, the capacitance versus frequency chart has been presented in **Figure 6**. Due to a significant difference between the capacitance values depicted for NTs in comparison to other materials, capacitance has been replaced with capacitance retention. Fast response of the NTs cell can be explained by the very high conductivity of the material. For NTs the capacitance remains stable up to 3 Hz while gradually drops for ReS_2, the composite still preserves 50% value at 1 Hz. As

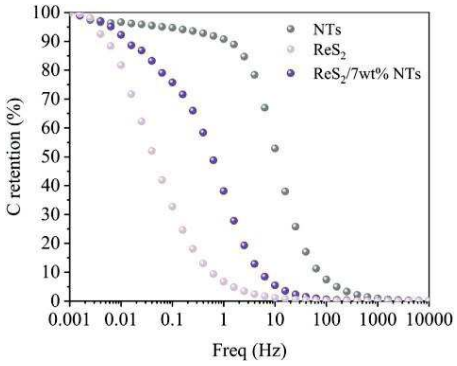

Figure 6. Capacitance retention versus frequency for ReS_2/NTs composite and its components.

expected, the composite possesses the intermediate characteristics. In conclusion, a proportion of components in composite has a fundamental influence on charge propagation.

The cyclability of the ReS_2/7 wt% NTs were also studied (Figure S4, Supporting Information) by performing 13 000 galvanostatic cycles at 0.8 V with current rate of 1 A g^{-1}. Capacitance retention was found to be 85% of the initial value.

The second TMD/composite material studied in this work is graphene-like 3DG/FeS_2. This unique carbon skeleton characterized by an interconnected, porous structure including pores with various size, ranging from a few micrometers to nanometers, provides excellent electron and ion conductivity.[34] Considering the chemical stability and physical robustness of 3DG-like structure, it can be used as the promising scaffold for deposition of other active material[35–39] such as FeS_2. The structure of 3DG is affected by its precursor, that is, graphite oxide. The proper oxidation of graphite powder to graphite oxide is important, since it affects the dispersion of GO layers inside the solution.[40] Graphite oxides with high content of different oxygenated functionalities guarantee the creation of 3DG matrix with interconnected porous structure. Subsequently, the dispersion level of GO layers has the main influence on the size of the pores, in the porous skeleton of 3DG.[41] Deposition of a thin layer of the TMDs on 3DG network improves not only the power rate but also the capacitive behavior of the TMDs-based electrodes, since all of the TMDs content will be accessible to ions for surface electrochemical interactions.

For physicochemical characterization of graphene-like 3DG/FeS_2 composite, N_2 sorption measurements were performed. Figure S5, Supporting Information presents the isotherms and the pore size distribution for the nanotextured 3DG/FeS_2. Specific surface area and the porosity properties are displayed in Table S1, Supporting Information. A moderate drop of porosity is observed for composite material. **Figure 7** shows the SEM images of freeze-dried 3DG and 3DG/FeS_2 composites. 3DG sample consists of a hierarchical highly porous structure. The pores are connected to each other and are spread in the internal structure of this substrate. The walls of the graphene-like network are thin and majority of the internal space is occupied by void, which implies the minimal aggregation of graphene layers.[42] Deposition of the active materials on such a porous structure, including pores with

 © 2021 The Authors. Small published by Wiley-VCH GmbH

ADVANCED SCIENCE NEWS
www.advancedsciencenews.com

NANO · MICRO small
www.small-journal.com

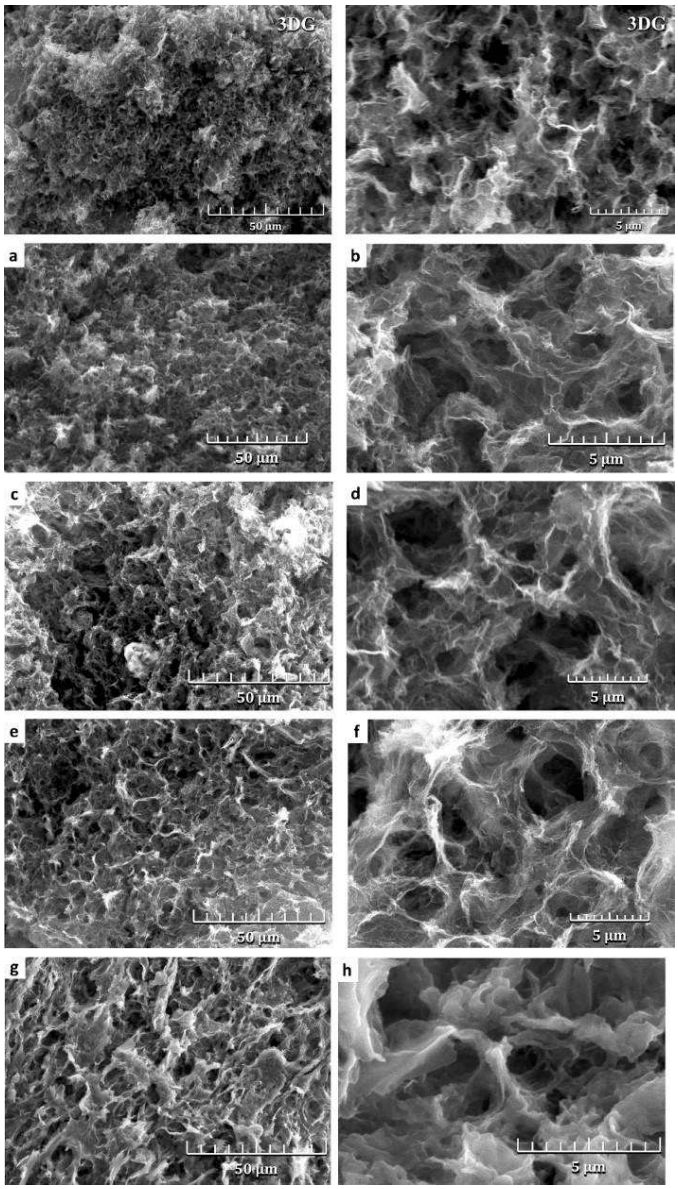

Figure 7. SEM images of freeze-dried 3DG and 3DG/FeS_2 composites at different magnifications a,b) 5, c,d) 10, e,f) 15, g,h) 20 wt% FeS_2.

 © 2021 The Authors. Small published by Wiley-VCH GmbH

ADVANCED SCIENCE NEWS
www.advancedsciencenews.com

NANO · MICRO small
www.small-journal.com

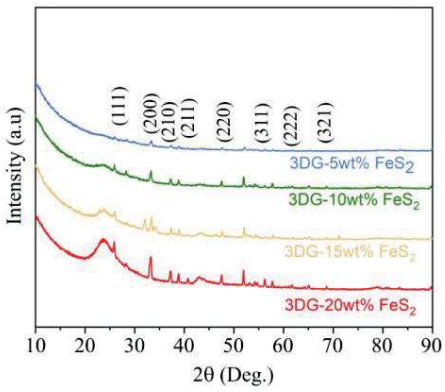

Figure 8. XRD structural characterization of 3DG/FeS_2 composites with various content of sulfide.

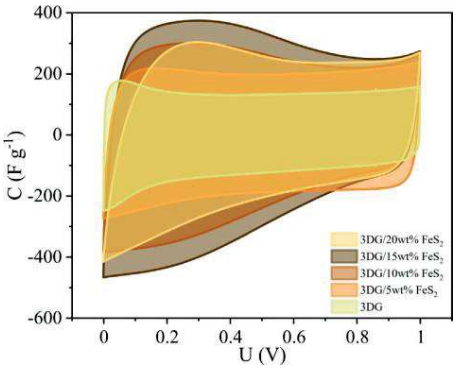

Figure 9. Comparison of CVs at 2 mV s^{-1} for composites with a different FeS_2 content. Electrolyte—1 mol L^{-1} Na_2SO_4.

a wide range size, can be challenging, since high percentage of loading will result in losing a majority of small pores which plays a crucial rule in capacitive applications based on sorption/desorption. Figure 7 displays the images taken from the inner space of 3DG-5 wt% FeS_2 (a,b), 3DG-10 wt% FeS_2 (c,d), 3DG-15 wt% FeS_2 (e,f), and 3DG-20 wt% FeS_2 (g,h), respectively. All the samples are highly porous and they are comparable to the internal structure of 3DG skeleton. Inhomogeneous deposition of FeS_2 is observed especially for higher sulfide percentage with a thickness of ≈30–50 nm. It can be suggested that too high loading of active material (20%) can severely deteriorate the transportation of adsorbed ions into the bulk of capacitor electrode. This fact was proven further by the electrochemical evaluations.

Figure 8 reveals the XRD pattern of 3DG-FeS_2 with different percentage of loaded active materials. The characteristic peaks which appear at 26°, 34°, 39°, 44°, 57°, 62°, and 65° (2θ) are allocated to (111), (200), (210), (211), (311), (023), and (321) planes of FeS_2 with JCPDS Card Number of 98-005-9067. The peaks are quite sharp, it means that all the samples have a well-structured crystal lattice. From 3DG-5% FeS_2 to 3DG-20% FeS_2, the intensity of the characteristic peaks increases, that confirms the different amounts of deposited active materials over the surface of the 3DG substrate.

EDS mapping of C, Fe, and S elements for 3DG-5 wt% FeS_2 to 3DG-20 wt% FeS_2 proved a gradual increase of sulfide in composite. All elements have been uniformly scattered at entire surface of the surveyed area, which verifies the hierarchical structure of the composites. No significant agglomeration was spotted while monitoring a broad area of the surface. Moreover, the elemental characterization of the EDS spectrum is aligned with the observations from the maps, and further indicates the presence of Fe, and S elements at the surface of graphene substrate. Figure S6, Supporting Information shows example of EDS results for 3DG-15 wt% FeS_2.

The capacitive performance of the porous carbonaceous electrodes can easily be affected by structural transformation. As already discussed, deposition of active materials higher than an optimum amount decreases the accessible surface area of the substrate. To specify the proper percentage of loading, the prepared samples were evaluated by CV analysis. **Figure 9** represents the capacitive/faradaic behavior of the assembled symmetric cells based on each composite in comparison with the ideal behavior of 3DG which has most EDLC profile among all the other samples. As it can be seen, all the samples show almost a rectangular CV graph with a low resistance. At applied scan rate of 2 mVs^{-1} redox reactions are well observed in the form of a wide hump from 0 to 0.6 V. It enhances with the percentage of FeS_2 from 5% to 20%. This ill-defined peak is the result of redox activities in the composites. The surface area under the voltammograms for electrodes based on 3DG and with a higher content of FeS_2 until 15 wt% gradually increases. However, 3DG-20 wt% FeS_2 shows no further charge expansion in comparison with 3DG-15 wt% FeS_2. This observation may suggest that 3DG-20 wt% FeS_2 has an inferior porous structure compared to the other samples. Surely, the sample with the higher content of FeS_2 lost a part of microporosity at the sacrifice of having a higher content of redox active materials.

Faradaic reactions have been confirmed by running a three-electrode cell investigation of capacitor based on 3DG-15 wt% FeS_2 in various voltage windows (**Figure 10**a–d). It seems that hydrogen storage could be considered for the negative electrode in the range of potential from –0.33 to –0.7 V versus SHE (Figure 10c). Redox activity of Fe species is also well observed from 0.2 to 0.4 V versus SHE.

The quality of interconnected porous structure of composite can be studied through analyzing the capacitive behavior at the scan rates from 2 to 200 mV s^{-1} and at the current densities from 0.2 to 2 A g^{-1}. Interconnected porous structure allows a fast charge response for the 3DG/15 wt% FeS_2 composite (Figure S7a,b, Supporting Information). However, at very high rates a significant aggravation of characteristics is observed for both dependences. EIS, in the form of Nyquist plot, for 3DG material and all composites with FeS_2 clearly shows the difference between materials with various loading (Figure S8, Supporting Information). To study the charge propagation, capacitance

 © 2021 The Authors. Small published by Wiley-VCH GmbH

ADVANCED SCIENCE NEWS
www.advancedsciencenews.com

NANO · MICRO small
www.small-journal.com

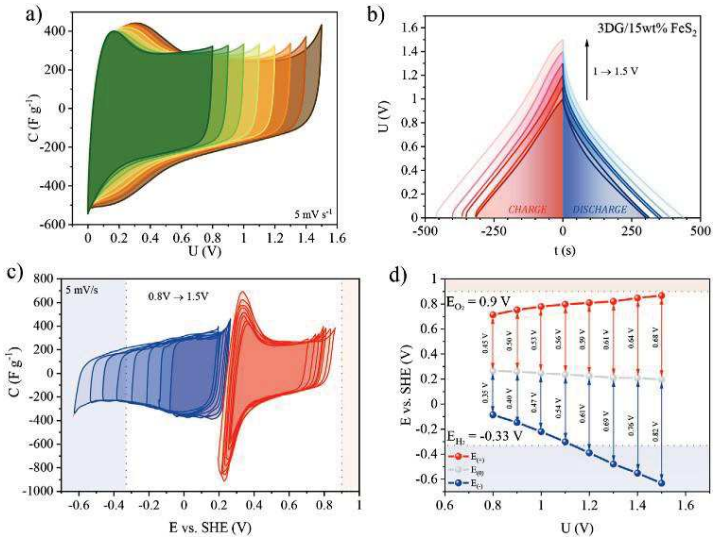

Figure 10. a) Voltage extension of 3DG/15 wt% FeS_2 electrode material in two-electrode cell, b) galvanostatic charge/discharge at 0.5 A g^{-1}, c) with separation of performance for (+) and (–) electrodes and d) indication of hydrogen and oxygen evolution.

versus frequency has been reported in Figure S9, Supporting Information for 3DG and composite with 15 wt% FeS_2. 3DG material supplies 50% capacitance at 1 Hz but for the composite with redox activity capacitance drops rapidly already at 50 mHz.

The cyclability of the 3DG/15 wt% FeS_2 composite were also investigated. Figure S10, Supporting Information presents 8000 galvanostatic cycles with current rate of 10 A g^{-1}.

For the comparison of both capacitor materials based on Re and Fe sulfides, the detailed charts of capacitance versus current loading are represented in Figure S11, Supporting Information. Energetic and Coulombic efficiencies for all materials are also indicated. As a rule of thumb, the higher redox activity, that is, higher capacitance, the lower charge propagation as well as energetic efficiency.

3. Conclusion

Two different composites based on carbon materials (NTs or 3DG) and TMDs were successfully prepared by hydrothermal synthesis and used as EC electrode materials. After detailed physicochemical characterization, their electrochemical performance was tested in ECs two- and three-electrodes cells. Mechanism of the energy storage has been elucidated. It was proven that type of transition metal such as rhenium restricts the voltage range of the capacitor (0.8 V). The composites show a specific capacitance of ≈110 F g^{-1} for ReS_2/7 wt% NTs at 0.2 A g^{-1} and 240 F g^{-1} for 3DG/15 wt% FeS_2. The composition of the prepared composite differed completely. 3DG/FeS_2 consisted of mainly highly porous carbon matrix, with a small loading of TMDs while in ReS_2/7 wt% NTs, the majority of the composite was ReS_2 and NTs served as a conductive additive. The two different approaches of using TMD as an additive or as a fundamental component have brought different results based on the initial properties of the matrix. Selection of the carbon support and method of composite preparation affect the final electrochemical performance. Energetic efficiency of charge/discharge process was exploited for true capacitance evaluation. It has been proven that voltage extension in aqueous medium is affected by materials structure, that is, edge sites strongly restrict operational window, type of metal. The species of the most noble metals catalyze water decomposition.

4. Experimental Section

Preparation of ReS_2 and CNTs/ReS_2 Composite: First, 0.6 g of ammonium perrhenate (Sigma Aldrich), 0.25 g of hydroxylamine hydrochloride (Sigma Aldrich), and 1.6 g of L-Cysteine (Sigma Aldrich) were dissolved in 40 mL of distilled water. The substrate solution was mixed for 2 h before the autoclave reaction. Then, 0.039 g of (which constituted a 7 wt% of ReS_2 material) MWCNTs (OD: 20–40 nm; L: 5–15 µm; 95+%, Iolitec) were dispersed in 40 mL of distilled water by the ultrasonic device (Hielscher—UP50H) for 30 min. The as-prepared mixtures were transferred into a stainless steel autoclave (Parr Instruments—High-Pressure Compact Reactor 5521) and kept at 180 °C for 48 h with stirring (125 rpm). After the reaction, a black precipitate was collected by filtration and then dried at 70 °C for 12 h. The same procedure was adopted for the synthesis of ReS_2, but without using NTs.

Preparation of 3DG and 3DG/FeS_2: Tailoring 3D porous structure based on graphene was carried out using one-step hydrothermal self-assembly treatment. GO was prepared according to the modified

 © 2021 The Authors. Small published by Wiley-VCH GmbH

ADVANCED SCIENCE NEWS
www.advancedsciencenews.com

NANO · MICRO small
www.small-journal.com

Hummers' method.[41] GO aqueous dispersion (4 mg mL^{-1}) was prepared by sonication of graphite oxide solution using ultrasonic bath for 1 h. Next, the GO solution was transferred into a Teflon-lined stainless steel autoclave (100 mL), and was kept without any stirring at 180 °C for 24 hr. Then, the autoclave was cooled down to 25 °C, and the formed cylindrical hydrogel was extracted and was stored in DI water to replace the undesired by-products inside the pores with water molecules. The purified hydrogel was freeze-dried prior the structural and elemental characterizations. The synthesis of 3DG/FeS_2 was carried out using a one-step hydrothermal reaction. For this purpose, different amounts of $FeCl_3$ 4 H_2O were dissolved in 20 mL ethylene glycol. Then, 60 mg of GO was dissolved into 30 mL of DI water. Later, the $FeCl_3$ and GO solutions were homogeneously dispersed in each other using ultrasonic bath. The samples contained 5, 10, 15, and 20 wt% of $FeCl_3$ in GO solution. Then, 15 mg of elemental sulfur was added to all the mixtures. The pH of the mixture was tuned to 9 before it was transferred into a 100 mL Teflon-lined stainless steel autoclave, and maintained at 200 °C for 24 h. After, the autoclave was cooled down to the room temperature and the 3DG/FeS_2 hydrogels were rinsed with water and ethanol before electrochemical analysis. Prior to physicochemical characterizations, the samples were freeze-dried.

Physical Characterization: Morphology of the samples was determined with the use of SEM Tescan Vega 5135 coupled with the PGT Avalon X-ray microanalyzer adapter for the evaluation of the EDS.

Diffractograms were obtained from aparatus, BRUKER D8 Advanced, equipped with Johansson monochromator using Cu Kα radiation (Cu Kα, λ = 1.5406 Å) and silicon strip detector LynxEye. The minimum measurement angle was 0.6 2Θ deg.

The specific surface area of samples were determined during N_2 adsorption/desorption at 77 K by using porosity analyzer ASAP 2460 (Micromeritics, USA). The samples were degassed for 24 h at 100 °C (He atmosphere and then for 5 h under the high vacuum) prior the measurements. Pore size distribution was evaluated using 2D-NLDFT model. The range of 0.01–0.05 relative pressure (p/p_0) was used for calculation of the specific surface area.

Electrode Preparation and Electrochemical Characterization: All the electrodes based on ReS_2/7 wt% NTs composite contained 90 wt% of active material, 5 wt% of binder, that is, polytetrafluoroethylene (60 wt% dispersion in water, Sigma Aldrich) and 5 wt% of conducting agent (C-NERGY Super C65, Imerys). Components were mixed in a mortar until dough-like material was obtained. Then it was rolled on a calendaring machine in order to obtain 200 µm thickness sheet of electrode material. Electrodes in a shape of discs with the diameter of 10 mm were cut from the foil, followed by drying in 70 °C for 24 h. The electrodes of similar mass separated by a glass microfiber membrane (GF/A, Whatman, diameter of 12 mm) were soaked with 1 mol L^{-1} Li_2SO_4 aqueous electrolyte.

For 3DG self-standing samples 1 mol L^{-1} Na_2SO_4 was used. Active materials loading per electrode was 8–10 mg for NT_S/ReS_2 and 2.5–3 mg for 3DG/FeS_2 composites.

All the electrochemical cells were investigated by using VMP3 multichannel potentiostat/galvanostat (Biologic, France) with the EC-lab software.

Supporting Information

Supporting Information is available from the Wiley Online Library or from the author.

Acknowledgements

M.F.K. and M.T. contributed equally to this work. E.F. supervised this project. The authors would like to acknowledge OPUS project financed by National Science Centre, Poland (project no. 2018/31/B/ST4/01852) for the financial support of the research.

Conflict of Interest

The authors declare no conflict of interest.

Data Availability Statement

The data that support the findings of this study are available from the corresponding author upon reasonable request.

Keywords

3D graphene, carbon nanotubes, electrochemical capacitors, transition metal-dichalcogenides

Received: October 31, 2020
Revised: January 22, 2021
Published online: March 19, 2021

[1] E. Frackowiak, F. Beguin, *Carbon* **2001**, *39*, 937.
[2] K. Fic, A. Platek, J. Piwek, E. Frackowiak, *Mater. Today* **2018**, *21*, 437.
[3] P. Simon, Y. Gogotsi, *Nat. Mater.* **2010**, *7*, 845.
[4] M. Yang, B. Cheng, H. Song, X. Chen, *Electrochim. Acta* **2010**, *23*, 7021.
[5] D. Guan, Z. Gao, W. Yang, J. Wang, Y. Yuan, B. Wang, M. Zhang, L. Liu, *Mater. Sci. Eng. B* **2013**, *178*, 736.
[6] D. Liang, Z. Tian, J. Liu, Y. Ye, S. Wu, Y. Cai, C. Liang, *Electrochim. Acta* **2015**, *182*, 376.
[7] H. Wang, D. Tran, J. Qian, F. Ding, D. Losic, *Adv. Mater. Interfaces* **2019**, *6*, 1900915.
[8] W. Choi, N. Choudhary, G. H. Han, J. Park, D. Akinwande, Y. H. Lee, *Mater. Today* **2017**, *20*, 116.
[9] N. Choudhary, M. A. Islam, J. H. Kim, T.-J. Ko, A. Schropp, L. Hurtado, D. Weitzman, L. Zhai, Y. Jung, *Nano Today* **2018**, *19*, 16.
[10] L. Lin, W. Lei, S. Zhang, Y. Liu, G. G. Wallace, J. Chen, *Energy Storage Mater.* **2019**, *19*, 408.
[11] S. Ding, D. Zhang, J. S. Chen, X. W. D. Lou, *Nanoscale* **2012**, *4*, 95.
[12] S. Wang, J. Zhu, Y. Shao, W. Li, Y. Wu, L. Zhang, X. Hao, *Chem. Eur. J.* **2017**, *23*, 3438.
[13] K. Gopalakrishnan, S. Sultan, A. Govindaraj, C. Rao, *Nano Energy* **2015**, *12*, 52.
[14] Q. Ji, C. Li, J. Wang, J. Niu, Y. Gong, Z. Zhang, Q. Fang, Y. Zhang, J. Shi, L. Liao, *Nano Lett.* **2017**, *17*, 4908.
[15] N. Choudhary, C. Li, H.-S. Chung, J. Moore, J. Thomas, Y. Jung, *ACS Nano* **2016**, *10*, 10726.
[16] T. Quan, N. Goubard-Bretesché, E. Härk, Z. Kochovski, S. Mei, N. Pinna, M. Ballauff, Y. Lu, *Chem. Eur. J.* **2019**, *25*, 4757.
[17] X. Chen, J. Ding, J. Jiang, G. Zhuang, Z. Zhang, P. Yang, *RSC Adv.* **2018**, *8*, 29488.
[18] S. Ratha, C. S. Rout, *ACS Appl. Mater. Interfaces* **2013**, *5*, 11427.
[19] S. Liu, D. Gao, J. Li, K. San Hui, Y. Yin, K. N. Hui, S. C. Jun, *J. Mater. Chem. A* **2019**, *7*, 26618.
[20] P. Asen, M. Haghighi, S. Shahrokhian, N. Taghavinia, *J. Alloys Compd.* **2019**, *782*, 38.
[21] X. Xie, M. Mao, S. Qi, J. Ma, *CrystEngComm* **2019**, *21*, 3755.
[22] Q. Zhang, S. Tan, R. G. Mendes, Z. Sun, Y. Chen, X. Kong, Y. Xue, M. H. Rümmeli, X. Wu, S. Chen, *Adv. Mater.* **2016**, *28*, 2616.
[23] M. Mao, C. Cui, M. Wu, M. Zhang, T. Gao, X. Fan, J. Chen, T. Wang, J. Ma, C. Wang, *Nano Energy* **2018**, *45*, 346.
[24] S. Liu, W. Lei, Y. Liu, Q. Qiao, W.-H. Zhang, *ACS Appl. Mater. Interfaces* **2018**, *10*, 37445.

 © 2021 The Authors. Small published by Wiley-VCH GmbH

[25] G. Lota, K. Fic, E. Frackowiak, *Energy Environ. Sci.* **2011**, *4*, 1592.
[26] H. Pan, J. Li, Y. Feng, *Nanoscale Res. Lett.* **2010**, *5*, 654.
[27] J. Gao, L. Li, J. Tan, H. Sun, B. Li, J. C. Idrobo, C. V. Singh, T.-M. Lu, N. Koratkar, *Nano Lett.* **2016**, *16*, 3780.
[28] A. Laheäär, P. Przygocki, Q. Abbas, F. Béguin, *Electrochem. Commun.* **2015**, *60*, 21.
[29] H. Li, C. Tsai, A. L. Koh, L. Cai, A. W. Contryman, A. H. Fragapane, J. Zhao, H. S. Han, H. C. Manoharan, F. Abild-Pedersen, *Nat. Mater.* **2016**, *15*, 48.
[30] Q. Zhang, W. Wang, J. Zhang, X. Zhu, Q. Zhang, Y. Zhang, Z. Ren, S. Song, J. Wang, Z. Ying, *Adv. Mater.* **2018**, *30*, 1707123.
[31] W. Shi, G. Li, Z. Wang, *J. Phys. Chem. C* **2019**, *123*, 12261.
[32] Q. Sun, B. Zhang, L. Diao, B. Chen, K. Song, L. Ma, F. He, *J. Mater. Chem. A* **2020**, *8*, 11607.
[33] J. Pan, R. Wang, X. Xu, J. Hu, L. Ma, *Nanoscale* **2019**, *11*, 10402.
[34] Y. Xu, Z. Lin, X. Zhong, X. Huang, N. O. Weiss, Y. Huang, X. Duan, *Nat. Commun.* **2014**, *5*, 4554.
[35] K. Yao, Z. Xu, M. Ma, J. Li, F. Lu, J. Huang, *Adv. Funct. Mater.* **2020**, *30*, 2001484.
[36] X. Zhang, J. Zhang, Y. Chen, K. Cheng, J. Yan, K. Zhu, K. Ye, G. Wang, L. Zhou, D. Cao, *J. Colloid Interface Sci.* **2019**, *536*, 291.
[37] Y. Zou, R. Liu, W. Zhong, W. Yang, *J. Mater. Chem. A* **2018**, *6*, 8568.
[38] D. Wu, W. Zhong, *J. Mater. Chem. A* **2019**, *7*, 5819.
[39] Y. Wang, M. Zhang, T. Ma, D. Pan, Y. Li, J. Xie, S. Shao, *Mater. Lett.* **2018**, *218*, 10.
[40] B. Konkena, S. Vasudevan, *J. Phys. Chem. Lett.* **2012**, *3*, 867.
[41] M. Foroutan, L. Naji, *Electrochim. Acta* **2019**, *301*, 421.
[42] J. Li, G. Zhang, C. Fu, L. Deng, R. Sun, C.-P. Wong, *J. Power Sources* **2017**, *345*, 146.

 © 2021 The Authors. Small published by Wiley-VCH GmbH

4. Article 2

Title: ***Fast response supercapacitor based on carbon-VS_2 electrodes with a wide operating voltage range***

Authors: Masoud Foroutan Koudahi, Elżbieta Frąckowiak*

Journal: Energy Storage Materials

DOI: https://doi.org/10.1016/j.ensm.2022.04.021

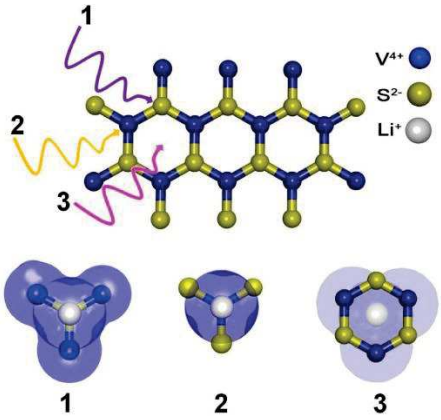

Motivation

Designing electrodes with an optimized electrochemical performance is one of the main challenges in developing aqueous-based ECs. In general, researchers are trying to integrate pseudocapacitive and EDL capacitive materials to improve the energy output of the cell. However, one should consider that most of the trendy pseudocapacitve materials such as 2D layered TMDs and MXenes show a high catalytic activity for water decomposition in aqueous media which results in narrowing the working voltage of the cell.

Previous studies revealed the instability of aqueous electrolytes in ReS_2-based ECs, where the working potential of electrodes was limited even below the theoretical values. In contrast, metal oxide/sulfides based on transition metals such as Mn or V have delivered charge storage in a wider working potential. Therefore, VS_2 was selected for this study as the pseudocapacitive material. Our approach, to improve the energy and power response of ECs in neutral aqueous electrolytes, was based on electrodes that are well-stable against parasitic reactions (catalytic activity for water decomposition and oxidation/corrosion).

The amount of TMD loading governs the charge response of a hybrid electrode. To highlight this influence further, two composites with different VS_2-to-3DG carbon proportions were prepared using a one-step hydrothermal treatment. SEM studies revealed a well-interconnected porous structure for the optimal composite electrode. Importantly, the materials seem to be significantly less dense, as the walls of pores are made of only a few layers of graphene. TEM analysis showed the possibility of having some VS_2 nanoparticles that are deposited not on the surface but even in between parallel layers. In fact, the deposited VS_2 nanoparticles can play the role of spacer to prevent the restacking of graphene layers, thereby increasing the surface accessibility of the electrode.

Temperature-programmed desorption (TPD) analysis showed a very low proportion of edge-to-basal sites for this sample, which was assigned further to the influence of ammonia and the other precursors in reducing the 3DG oxygen content and improving the dispersibility of graphene layers during the self-assembly treatment.

Electrochemical characterization was conducted to analyze the electrode's charge storage. It has been proven that the catalytic activity of electrodes can restrict the cell voltage, even in the case of materials like VS_2 with high loading. Notably, the optimal composite exhibited a stable charge response, not only below the theoretical H_2 but also *versus* the O_2 evolution line. This finding is significant as it means a wide working voltage (1.8V) was available for the assembled symmetric cell, enhancing its practical applicability. The high stability of the 3DG/VS_2 electrodes against corrosion reactions was demonstrated. Three-electrode cell studies also revealed that VS_2 exhibits faradaic activity at initial potentials during the positive polarization, while a pure capacitive response was observed during the negative sweeping.

A very high power response was observed even at 1 Hz or high scan rates and current densities. The wide working voltage and high-frequency response improved energy and power density of EC.

Energy Storage Materials 49 (2022) 255–267

Contents lists available at ScienceDirect

Energy Storage Materials

journal homepage: www.elsevier.com/locate/ensm

Fast response supercapacitor based on carbon-VS_2 electrodes with a wide operating voltage range

Masoud Foroutan Koudahi, Elżbieta Frąckowiak*

Institute of Chemistry and Technical Electrochemistry, Poznan University of Technology, Poznan, 60965, Poland

ARTICLE INFO

Keywords:
Three-dimensional graphene
Vanadium disulfide
Transition metal-dichalcogenide
Composite electrode
Wide operating voltage
Aqueous supercapacitor

ABSTRACT

The presented work has undertaken a rational design of composite electrodes based on three-dimensional graphene-like (3DG) and transition metal-dichalcogenide (TMD), i.e., VS_2. The aim was to expand the working voltage of TMD-based electrochemical capacitor (EC) in an aqueous medium above the thermodynamic limits. It has been found that designing the electrode material with a low proportion of edge to basal sites decreases the roughness of the electrode surface, and therefore, the possibility of water decomposition. The assembled cell based on the optimized composite electrode operating with lithium nitrate (1M) delivered a stable performance in a wide voltage range up to 1.8 V. Promising cyclic stability with capacitance retention of 80% after 7500 cycles at 1 A g^{-1} was recorded. The engineered structure of the electrode allowed the cell offering a superfast response with capacitive behavior even at a high scan rate of 3000 mV s^{-1}. In addition, the cell delivered a high energy density of 18 Wh kg^{-1} at the power density of 430 W kg^{-1} at a current density of 1 A g^{-1}. At high current density of 100 A g^{-1} the supercapacitor presented an energy density of 12 Wh kg^{-1} at the power density of 31000 W kg^{-1}.

1. Introduction

Efficient energy storage devices play a vital role in designing hybrid vehicles and advanced portable electronic products [1]. Nowadays, the industry is facing a growing demand for reliable, fast response power sources [2]. Electrochemical Capacitors (ECs), by nature, can provide a high power density, since they follow a non-faradaic mechanism for storing energy [3]. In recent years, carbonaceous materials such as activated carbon [4], graphene [5], and carbon nanotubes [6,7] were used as the electrode materials in ECs. Owing to a developed surface area, they offer a high capacitance but also long cycle life [8,9]. Conversely, ECs fail to meet the demand for having a high energy density, which is several orders of magnitude lower than for the traditional batteries [10]. The energy density (E) of electrochemical capacitors can be calculated by the following equation:

$$E = \frac{1}{2} CV^2 \quad (1)$$

It can be improved by enhancing either the capacitance or the working voltage window of a cell [11]. One promising approach to improve the EC performance is integrating pseudocapacitive materials such as metal oxides/sulfides which can enhance the energy density of ECs through fast, superficial redox reactions [12,13]. 2D materials such as Transition Metal Dichalcogenides (TMDs) [14,15] and Mxenes [16] have gained a lot of attention owing to their layered structure which provides a promising pathway for electron and ion transport. TMDs such as MoS_2 [17] and WS_2 [18] have been widely investigated during recent years and they were able to deliver high energy densities through the fast redox response. However, hybridization of pseudocapacitive materials with carbon material is challenging, since it may result in limitation of the cell voltage. For example, the integration of metal oxides/sulfides with carbon-based substrate usually increases the roughness of the electrode surface. By doing so, the electrode materials and the aqueous electrolytes become vulnerable to corrosion and water decomposition, respectively. At the same time, it has been proven that electrolyte medium, especially the type of anion, plays an important role in reducing water decomposition near the thermodynamic limit. For example, anions such as NO_3^- and ClO_4^- decrease the tendency of hydrogen bonding between water molecule (chaotropic species), while anions such as CH_3COO^- are considered as kosmotropic one, since it increases the possibility of H-bonding between H_2O molecules [19].

In addition, having a substrate with a high proportion of edge sites to basal planes promotes the occurrence of the aforementioned reactions, as well [20].

Here, graphene-like material with a honeycomb structure (3DG) was used as the substrate. This framework is made of edge-connected

* Corresponding author.
E-mail address: elzbieta.frackowiak@put.poznan.pl (E. Frąckowiak).

https://doi.org/10.1016/j.ensm.2022.04.021
Received 30 November 2021; Received in revised form 4 April 2022; Accepted 12 April 2022
Available online 14 April 2022
2405-8297/© 2022 The Authors. Published by Elsevier B.V. This is an open access article under the CC BY license (http://creativecommons.org/licenses/by/4.0/)

graphene walls which minimize the existence of sharp edge sites. In addition, 3DG provides a conductive porous skeleton for not only fast transportation of electrons and ions but also the suitable embedding of redox-active species on carbon materials [21]. Vanadium disulfide (VS_2) was chosen as the pseudocapacitive component owing to a high electrical and ionic conductivity as well as interlayer spacing of 5.746 Å [22–24]. From the physical point of view, VS_2 has a low energetic band of 0.187 eV, which substantially is lower than previously studied TMDs such as MoS_2 (1.9 eV) [25]. Moreover, electrode materials based on VS_2 show a fast Li^+ diffusion rate [26]. This layered material previously was investigated in different capacitor studies [27–32]. From these studies, the assembled cells based on VS_2 showed a relatively narrow voltage not higher than 1.4V even in an asymmetric cell. However, some of the presented works did not consider the high ohmic drop, which imply the fact that the realistic voltage window is narrower than the reported one. From the charge-discharge profiles at low current densities, it can be seen that the cells do not deliver capacitance after being fully charged [28,32]. From the cyclic voltammetry profiles, especially at scan rates higher than 200 mV s^{-1}, the electrodes failed to show the correct electrochemical performance which indicates that the assembled cells suffer from a slow power response. In most cases, the cells revealed a battery-like performance by showing a substantial deviation from rectangular and triangular shapes of cyclic voltammetry (CV) or galvanostatic charge-discharge (GCD) profiles, respectively, which from the electrochemical point of view are characteristic of ECs [16].

In this work, 3DG-VS_2 hybrid electrodes with different sulfide contents (from 20% to 50% of VS_2) were prepared. The assembled cell based on 3DG-20 wt% VS_2 showed good voltage stability up to 1.8V in 1M $LiNO_3$, which is superior to that of 3DG-50 wt% VS_2, previously reported VS_2 electrodes [27–32], and conventional ACs (1.5V) [33] in aqueous media. Owing to the synergetic effect (structural and chemical), 3DG-20 wt% VS_2 offered a rapid response especially in high regimes. These advanced ECs based on 3DG/VS_2 composite demonstrated a high energy, power and long-term cycleability. Present findings draw a clear insight for formulating new approaches for rational integration of carbon and pseudocapacitive materials to reach exceptional EC metrics.

2. Experimental section

2.1. Synthesis of 3DG-VS_2

Graphene oxide (GO) was synthesized according to the modified Hummers' method reported elsewhere [34]. 3DG-20 wt% VS_2 and 3DG-50 wt% VS_2 were synthesized using one-step in situ hydrothermal method. Briefly, a proper concentration of GO solution (2.5 mg ml^{-1}) was dispersed using and ultrasonic bath for 30 min. Meanwhile, 0.42 mmol and 1.7 mmol ammonium metavanadate were dissolved in 30 ml mixture of DI water and ammonia (25ml:5ml), separately, and the two solutions were stirred vigorously. Later, 2.1 mmol and 8.5 mmol of thioacetamide (TAA) were added to the former and the latter solutions, respectively. After 30 min of stirring at room temperature, the two solutions were added to their assigned GO solution in a drop wise fashion. The whole mixtures continued to be stirred for another 20 min before becoming transferred to the stainless steel autoclave. In the next step, the samples were kept at the temperature of 180 °C for the duration of 24 hr. Subsequently, the autoclaves were allowed to cool down naturally to the room temperature. Eventually, the prepared cylindrical hybrid hydrogels were extracted and washed with DI water for one week to the complete exchange of unreacted species with water molecules. For the sake of comparison, the bare substrate in presence of 2.1 mmol of TAA was synthesized following the same aforementioned protocol.

2.2. Physical characterization

The chemical structure of the prepared samples was evaluated by XRD and Raman analyses. The XRD investigation using BRUKER D8 Advanced, equipped with Johansson monochromator using Cu Kα radiation (Cu Kα, λ = 1.5406 Å). Raman analysis was carried out using ThermoFisher® DXR Raman microscope equipped with a 532 nm laser. To observe the internal porous structure, the prepared samples were subjected to 72 hr of freezing drying until the complete transformation of the hydrogel to the aerogel. SEM analysis was performed using Scanning Electron Microscope SEM Jeol 7001TTLS. To specify the surface area of the samples, the Brunauer–Emmett–Teller equation in the relative pressure range 0.01–0.05 was carried out. An ASAP 2460 analyzer (Micromeritics, US) was used for this purpose. Temperature programmed desorption (TPD) analysis was carried out using TG equipment (TG209 F1 Iris, NETZSCH) coupled with a mass spectrometer (QMS 403C Aëolos, NETZSCH). For this purpose, 8 mg of the prepared samples were heated from 25 °C to 900 °C (heating rate 20 °C min^{-1}) under the helium gas with a flow rate of 50 ml min^{-1}.

2.3. Electrode preparation and characterization

The electrochemical performance of the as-prepared samples was examined using two-electrode and three-electrode swagelok® cells with stainless steel current collectors and inner diameter of 12 mm. The materials were cut in a disk shape (diameter 8 mm, thickness 1 mm) and served as both negative and positive electrodes without using any binder or conductive additive. A round piece of Whatman Cellulose filter paper (ashless, No. 42) was cut in a diameter of 10 mm and used as the separator. Before running the electrochemical experiments, the electrode material and the separator were immersed in aqueous electrolyte for 72 h to complete exchange of water molecules in the pores with electrolyte ions. All the experiments were carried out in 1 M $LiNO_3$. CV, GCD, and EIS experiments were carried out on a VMP-3 and SP-200 BioLogic® potentiostat/galvanostat instrument.

3. Results and discussion

3.1. Physicochemical results

Figure S1 indicates the XRD data of 3DG and VS_2. The sharp peak at 2Θ=24.8° is assigned to the characteristic plane of 3DG with the interlayer spacing of 3.587 Å. Considering the spectra of VS_2, the characteristic peaks at 32, 36, 42, 55, 56, 58, and 67.5° are corresponding to the 100, 011, 102, 110, 103, 003, and 201 planes with a hexagonal lattice indexed by JCPDS card NO.: JCPDS 36-1139 [28]. Fig. 1a-d reveals the Raman spectra of 3DG, VS_2, 3DG-20 wt% VS_2, and 3DG-50 wt% VS_2. 3DG showed a distinguished peak at 1350 cm^{-1} as the result of graphitic disorder and defects in graphene walls. Another characteristic peak is located at 1550 cm^{-1} which explains the E_{2g} mode of the hexagonal lattice of л-л carbon bonds (Fig. 1a) [35].

Fig. 1b shows the Raman spectra of pure VS_2. The characteristic peaks are sharp which indicates the well-defined crystal lattice of the prepared TMD. There are two characteristic peaks, which appeared at 280 and 404 cm^{-1}, which are corresponding to the $E^1{}_{2g}$ and A_{1g} vibration mode of planes [28] $E^1{}_{2g}$ mode occurs because of the opposite vibration of the two sulfur atoms in the structure of VS_2. On the other hand, out-of-plane vibration of S atoms in opposite directions results in forming the A_{1g} vibration mode. The appeared peaks at 482 cm^{-1} can be assigned to the bending vibration of doubly coordinated sulfur atoms (S_2 atoms in Fig. 2). The located peak at 529 cm^{-1} could be the stretching mode of triply coordinated sulfur atoms (S_3 atoms in Fig. 2). However, the presence of vanadium oxygen species should not be excluded.

Fig. 1c-d confirms the successful hybridization of 3DG and VS_2. As the percentage of VS_2 in 3DG-VS_2 increases from 20 to 50%, the intensity of the characteristic peaks increases which proves various quantities of sulfide deposition on 3DG. The proportion of the D and G bands in 3DG and 3DG-20 wt% VS_2 are 1.3 and 1.4, respectively. A high proportion of intensity for D band to G band indicates the higher percent-

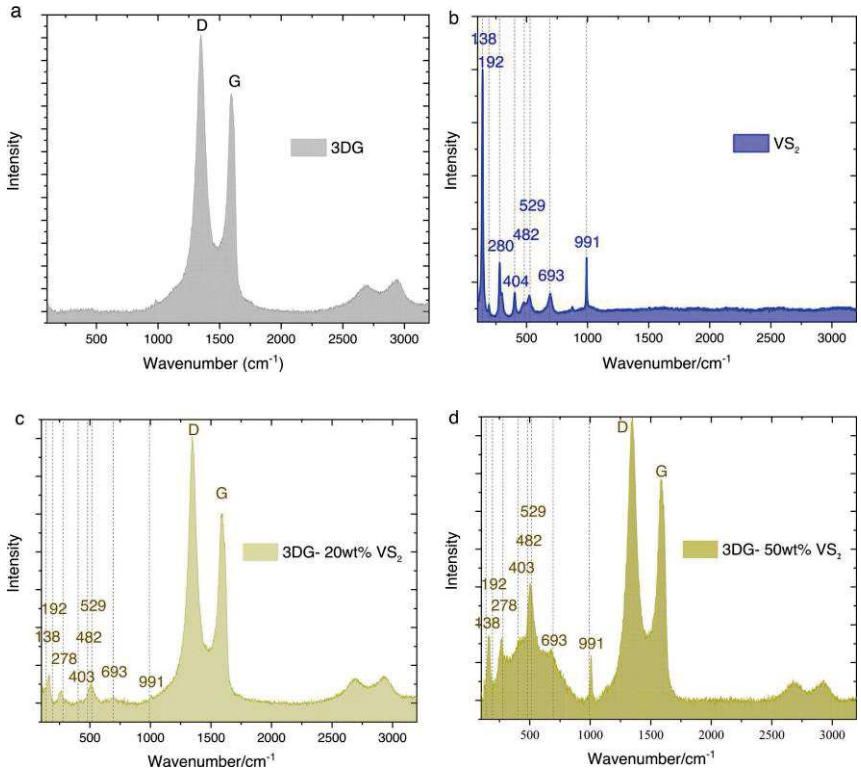

Fig. 1. Raman spectra of (a) 3DG, (b) VS_2 powder, (c) 3DG-20 wt% VS_2, and (c) 3DG-50 wt% VS_2.

age of sp^2 to sp^3 carbon hybridization. Due to the addition of reductive thioacetamide (TAA) in the self-assembly reaction, the 3DG-substrate in hybrid electrodes lost a high content of oxygen groups which will result in regaining a higher degree of sp^2 network [36].

In fact, the Raman mapping of two connected graphene layers shows a high intensity of the D band in grain boundaries between graphene layers [37]. In addition, the edged graphene layers are usually connected with various oxygen functional groups. Considering this fact, measuring the oxygen content of each sample allows us to gain a clear insight into the amount of edge-free graphene layers. To do so, a set of thermogravimetric (TG) analyses together with monitoring the content of CO, CO_2, and H_2O evolution was carried out. Figure S2 indicates the resulted TG plots of 3DG, 3DG-20 wt% TAA, 3DG-20 wt% VS_2, and 3DG-50 wt% VS_2. Table S1 represents the obtained values of this analysis. For 3DG sample an overall mass loss of 27.2% was detected whereas 19% loss can be assigned to the release of oxygen content (Figure S2a). On the other hand, 3DG-20 wt% VS_2 mass loss was 18.1%, including only 7.7% of oxygen evolution (Figure S2c). To understand the role of TAA in assisting the chemical reduction of 3DG for hybrid samples during the hydrothermal treatment, 3DG was prepared in presence of TAA (with the same amount that was used during the preparation of 3DG-20 wt% of VS_2), and the sample labeled as 3DG-20 wt% TAA. The TG analysis of 3DG-20 wt% TAA indicates a total mass loss of 9.2%, including 6% of oxygen release (Figure S2b). This data reveals the binary role of TAA (sulfur source and reducing agent) during the formation of 3DG-VS_2 samples. With increasing the content of TAA from 20% to 50%, 3DG-50 wt% VS_2 showed an oxygen loss equivalent to 4.8% (Figure S2d). To specify the content of each functional group in the resulted total oxygen loss, the evolved fragments were further transported with the carrier gas (He) to a mass spectrometer. Fig. 3 compares the content of CO and CO_2 evolution from 3DG and 3DG-20 wt% VS_2, including their deconvolution results. Phenolic groups and quinones are related to CO evolution. On the other hand, carboxyl groups as well as lactones are connected with CO_2 evolution. The deconvolution of CO profile related to 3DG shows a considerable amount of phenol evolution (1640 μmol g^{-1}) from 400 °C to 900 °C. This value, in the case of 3DG-20 wt% VS_2, was decreased to 59 μmol g^{-1}. However, we must take into account that phenolic groups can be located either at the basal or the edge of GO layers, and therefore, considering the obtained value of these functional groups may lead to a misleading conclusion about the content of oxygen at the edges of GO layers. As the result, comparing the number of surface functionalities such as carboxyl groups as well as lactones and quinones, which are exclusively positioned at the edge of GO layers, gives us a more correct interpretation. The deconvolution of CO in 3DG shows a mass loss equivalent to 620 μmol g^{-1} at the range of 600-900 °C, which is related to the release of quinone fragments. On the other hand, this value in 3DG-20 wt% of VS_2 is calculated as 69 μmolg^{-1}. From the CO_2 deconvolution, the value of 2100 μmol.g^{-1} and 1101 μmol g^{-1} mass loss at the range of 400 to 900 °C were detected that can be assigned to the evolution of carboxylic functionalities from 3DG and 3DG-20 wt%

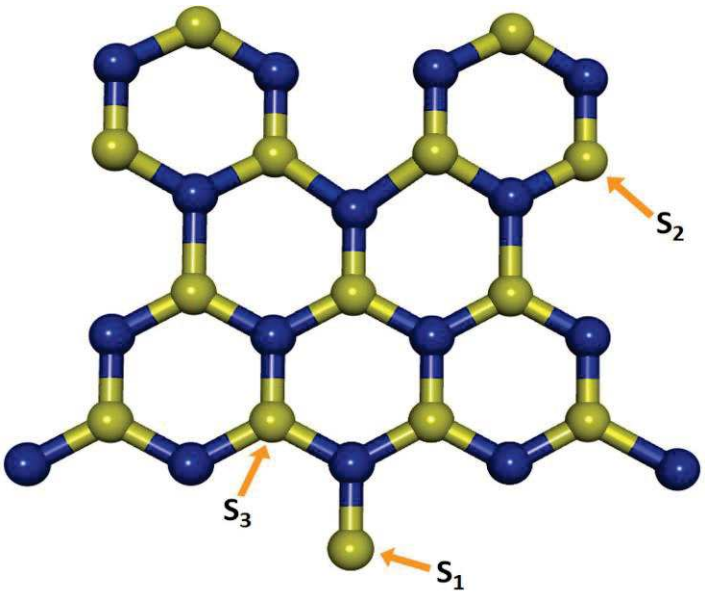

Fig. 2. Schematic representation of a VS_2 layer, including the location of sulfur atoms based on their different coordination number (Vanadium atoms: blue sphere, Sulfur atoms: yellow sphere).

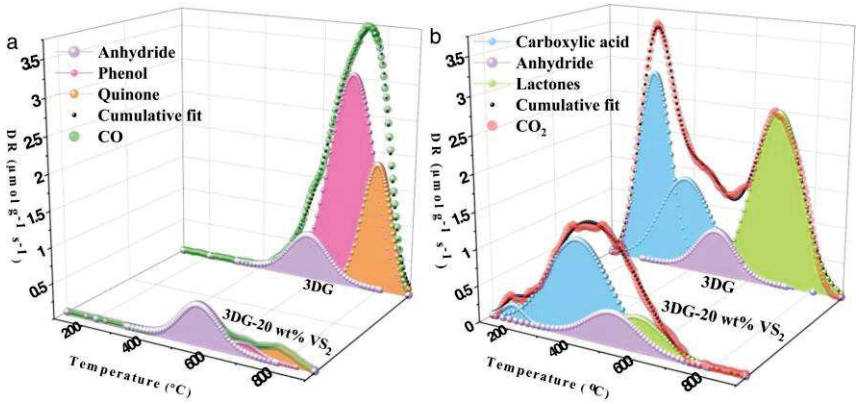

Fig. 3. Comparison between the TPD analysis of 3DG and 3DG-20 wt% VS_2, including CO (a) and CO_2 (b) desorption profiles with their deconvolution in independently fitted peaks (colorful dotted lines) and the obtained cumulative thermogram (black dotted lines).

VS_2, respectively. Furthermore, the evolution of lactones at 300-700 °C in 3DG and 3DG-20 wt% VS_2 was decreased from 1483 μmol g^{-1} to 249 μmol g^{-1}. These results prove the negligible amount of edged graphene layers in 3DG-20 wt% VS_2 in comparison with that of 3DG. The higher intensity of D/G bands in 3DG-20 wt% VS_2 is the result of a higher number of grain boundaries.

Figure S3 represents the content of CO_2 evolution from 3DG-20 wt% TAA and 3DG-50 wt% VS_2, including their deconvolution results. As it was expected, 3DG-20 wt% TAA showed a comparable amount of carboxylic groups evolution in comparison with that of 3DG-20 wt% VS_2 (1101 to 1013 μmol g^{-1}), while this content in the case of 3DG-50 wt% VS_2 was decreased to 799 μmol g^{-1}. Moreover, the amounts of lactone that were released in 3DG-20 wt% TAA and 3DG-20 wt% VS_2 are quite similar (249 μmol g^{-1}). It is worth mentioning that the content of CO evolution in 3DG-20 wt% TAA and 3DG-50 wt% VS_2 was negligible. Figure S4 indicates the SEM images obtained from the freeze-dried hydrogels of 3DG. The hierarchical structure of the substrate is made of macropores mainly with a diameter from 1-5 μm. The image with the higher magnification represents the existence of smaller pores that are embedded on the junction of walls. Fig. 4 illustrates the SEM images obtained from 3DG-20 wt% VS_2. Comparing the obtained images from 3DG and 3DG-20 wt% VS_2 reveals a higher level of porosity in the

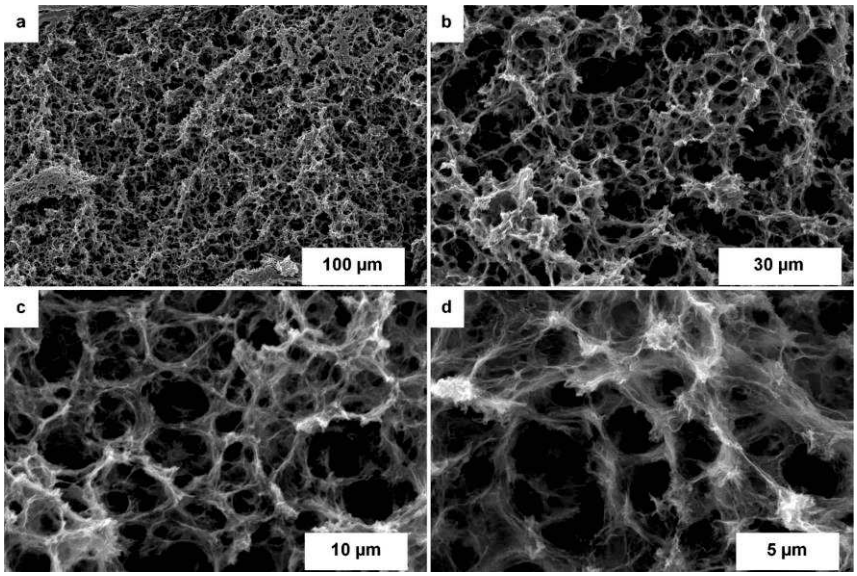

Fig. 4. SEM images of the freeze-dried 3DG-20 wt% VS_2.

composite compared to the substrate. Also, the internal framework of 3DG-20 wt% VS_2 represents an ordered structure with a higher level of interconnection and accessibility in comparison with that of 3DG. The mutual connection of graphene walls minimized the number of edge layers [20]. Moreover, no sign of agglomeration was observed which indicates a low ratio of bulk-to-surface within the internal structure.

Fig. 5 illustrates the SEM images from 3DG-50 wt% VS_2. At the first glance, the higher density of the porous structure compared to 3DG-20 wt% VS_2 is noticeable. Deposition of VS_2 higher than the optimum amount led to the significant blockage of the nanoporous framework, and therefore, the loss of the pores' accessibility and interconnectivity. Figure S5 demonstrates a SEM image for 3DG-20 wt% VS_2 and 3DG-50 wt% VS_2 at the highest magnification. Figure S5b shows an individual cube entity of VS_2 that is assembled by random stacking of VS_2 nanosheets, starting from the basal plane. Each sulfide layer has a diameter of 0.5 to 1 µm and a thickness of 50-100 nm [38,39]. These units consist of a few 2D layers which are grown on each other. Comparing the images with the lowest magnification which are taken from 3DG, 3DG-20 wt% VS_2, and 3DG-50 wt% VS_2, it can be said that 3DG-20 wt% VS_2 has a more homogeneous porosity. Furthermore, the structure of 3DG-20 wt% VS_2 seems to be less dense than the other samples.

Figure S6 and S7 demonstrate the obtained data from the elemental analysis. The homogenous distribution of various elements, including V and S at the surface of 3DG is visible from the map data recorded while monitoring a broad surface of the samples. Comparison of the maps proves further the complete coverage of 3DG with VS_2 in 3DG-50 wt% VS_2. The corresponding EDX spectrum reveals the atomic percentages of individual atoms. Fig. 6 presents the TEM images of the freeze-dried 3DG-20 wt% VS_2. Nanoparticles with a diameter of 20-35 nm are homogeneously distributed on the surface of a graphene layer (Fig. 6a, b). Almost no trace of agglomeration can be observed from the unique size of VS_2 nanoparticles. Fig. 6c indicates the (001) plane of VS_2 with the interlayer spacing of 2.6 Å. From the selected area electron diffraction (SAED) patterns, planes 001 and 002 (interlayer spacing of 6.6 Å) are highlighted (Fig. 6d).

Figure S8 and Table S2 represent the data from specific surface area measurements by N_2 sorption on 3DG, VS_2, 3DG-20 wt% VS_2, and 3DG-50 wt% VS_2. Considering the isotherm curves, 3DG and 3DG-50 wt% VS_2 showed a H_3-type hysteresis, while VS_2 and 3DG-20 wt% VS_2 showed a H_2-type hysteresis during the desorption. Comparison of the sorption values indicates that 3DG-20 wt% VS_2 has a higher surface area (256 $m^2\ g^{-1}$) than 3DG (190 $m^2\ g^{-1}$) and 3DG-50 wt% VS_2 (178 $m^2\ g^{-1}$).

Importantly, 3DG-20 wt% VS_2 has a higher mesoporosity (0.54 $cm^3\ g^{-1)}$ compared to that of 3DG (0.23 $cm^3\ g^{-1}$). On the other hand, 3DG-50 wt% VS_2 lost almost half of its mesoporosity (0.12 $cm^3\ g^{-1}$) in comparison with that of 3DG.

3.2. Electrochemical results

To determine the operational working voltage of the 3DG substrate, and GCD analyses in a wide range of voltage were carried out, and the recorded data is presented in Figure S9. During stepwise increase of the voltage, especially from 1.5V up to 1.7V, 3DG showed a current rise in the mid voltage range, probably as the result of unreduced oxygen functionalities or the semiconductive nature of some graphene walls [20]. The substrate showed almost pure capacitive performance with the upper limit voltage from 1V to 1.5V. For further expansion of voltage window to 1.7V, a deviation from the linear current response, following the start of the corrosion reactions or water decomposition, was observed. A steep current rise at the upper limit voltage of a CV plateau can be seen as an ohmic drop in the galvanostatic charge-discharge profile. Coulombic efficiency calculated only from discharge time (ignoring ohmic drop) gives higher capacitance values, whereas reliable values can be obtained only from the integration of the discharge plot. Comparison of the calculated energy efficiency shows that 3DG has an optimum working voltage up to 1.5V which is a promising value in aqueous medium. However, the combination of carbon substrates with pseudocapacitive materials usually narrows the operational voltage window of a cell. Specifically, most of the TMDs are catalytically active, and therefore, they enhance the

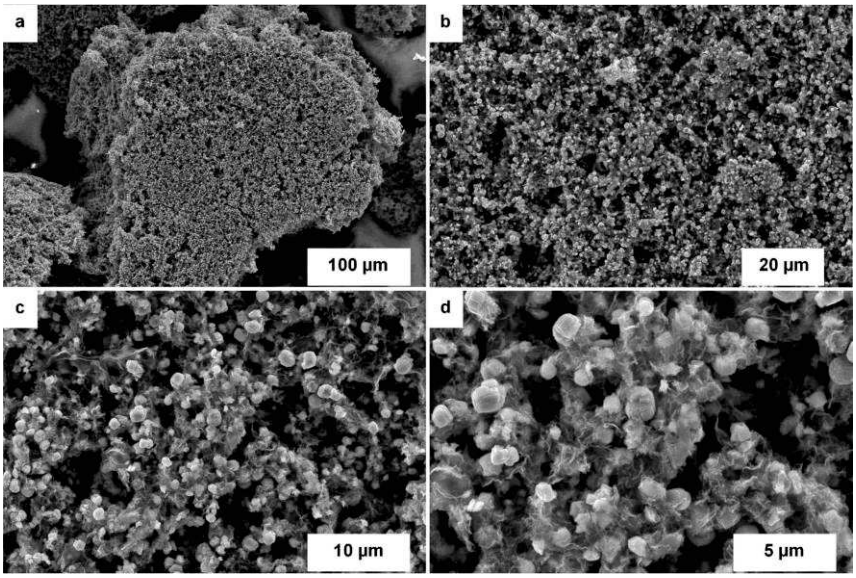

Fig. 5. SEM images of the freeze-dried 3DG-50 wt% VS_2.

possibility of hydrogen/oxygen evolution. Considering this fact, rational hybridization of carbonaceous substrates with TMDs is of paramount importance [40]. Fig. 7 indicates the stability window of 3DG-20 wt% VS_2 in a wide range of voltage. From the CV profile, the electrode is able to deliver a constant, capacitive response even up to 1.8V with no obvious sign of a sharp current rise at the upper limit voltage. The GCD profile reveals the same stable performance with moderate efficiency degradation. Up to 1.7V, the energy efficiency of 3DG and 3DG-20 wt% VS_2 was decreased to 58% and 81%, respectively.

It can be concluded that hybridization of 3DG and 20 wt% VS_2 does not affect the stability of the hybrid electrode with catalytic effects. Moreover, the optimum porous structure of 3DG-20 wt% VS_2, which is made of edge-free graphene walls, minimizes the possibility of the electrolyte decomposition, and allows the cell to provide stable performance in a wide range of voltages [20]. Following the obtained results, the safe operational voltage of 3DG-20 wt% VS_2 was selected to be 1.8V. To see the effect of VS_2 with a higher content on the electrochemical performance of the hybrid electrode, 3DG and VS_2 with an equal mass portion were prepared, as well. Figure S10 illustrates the electrochemical behavior of 3DG-50 wt% VS_2 upon gradual voltage expansion. Interestingly, 3DG-50 wt% VS_2 showed a relatively similar working voltage as 3DG. A significant current rise was observed immediately if expanding the upper limit voltage up to 1.3V. From the recorded GCD profiles, 3DG-50 wt% VS_2 showed an instant 16% drop in efficiency as the voltage window was expanded from 1.2 V to 1.3 V. Hybridization of VS_2 with 3DG higher than the optimum value narrowed the working voltage of 3DG-50 wt% VS_2 due to the following reasons: (i) A considerable increase in the catalytic activity of the electrode with sulfide, and subsequently, a shrinkage of voltage to less than 1.5V (operational working voltage of the bare 3DG); (ii) losing a considerable number of surficial redox-active sites, which decreases the involvement of electron transfer, and subsequently, the working voltage of the cell [40]. To evaluate the capacitive performance of the two composite electrodes, a series of electrochemical experiments in a broad range of sweep rates and current densities was carried out [41]. Fig. 8a shows the CV profile of 3DG-20 wt% VS_2. Comparing the capacitive behavior of 3DG and 3DG-20 wt% VS_2 at 5 mV s^{-1} reveals that the hybrid electrode has a substantially better performance as well as reversibility than that of the substrate.

To evaluate the power response of 3DG-20 wt% VS_2, CV plot in a wide range of scan rates was recorded. The sample revealed a supreme rate capability while maintaining its initial performance at 5 mV s^{-1} to a high sweep rate of 3000 mV s^{-1}. Fig. 8b presents the charge-discharge profiles recorded at low current regimes. Considering the triangular shape of plots, 3DG-20 wt% VS_2 showed a reversible and capacitive behavior without sign of ohmic drop. From integrating the discharge plot, the cell reached a high capacitance of 161 F g^{-1} at the current density of 1 A g^{-1}. Fig. 8c shows the GCD profiles of 3DG-20 wt% VS_2 recorded at an extremely high current density of 50 A g^{-1}, 70 A g^{-1}, and 100 A g^{-1}. Interestingly, the sample with the lower percentage of VS_2 almost preserved its capacitive performance at such high current regimes, where only a 0.25V IR-drop was observed (at 100 A g^{-1}). From the Electrochemical Impedance Spectroscopy (EIS) spectra, the vertical Warburg line shows almost no diffusion resistance against ions transportation. Reaching such a favorable capacitive performance requires high accessibility of ions to the internal porous structure of the electrode (Fig. 8d) [42]. In the case of hybrid electrodes, the key factor is the dominance of fast, surficial rather than sluggish, bulk redox activities. Also, VS_2 has a small band gap of 0.187 eV which reduces the impedance against electron transport [25]. Fig. 8e reveals the difference of the obtained capacitance as a function of frequency. 3DG-20 wt% VS_2 showed a semi-linear capacitance variation and a 71% capacitance retention up to 1 Hz. These results are in agreement with the data from pore size distribution (Table S2). In fact, the high dynamic of charge propagation can be assigned to the presence of mesopores in 3DG-20 wt% VS_2 [43].

A three-electrode cell investigation was further carried out to monitor the electrochemical behavior of individual 3DG-20 wt% VS_2 positive and negative electrodes with respect to the SHE reference electrode.

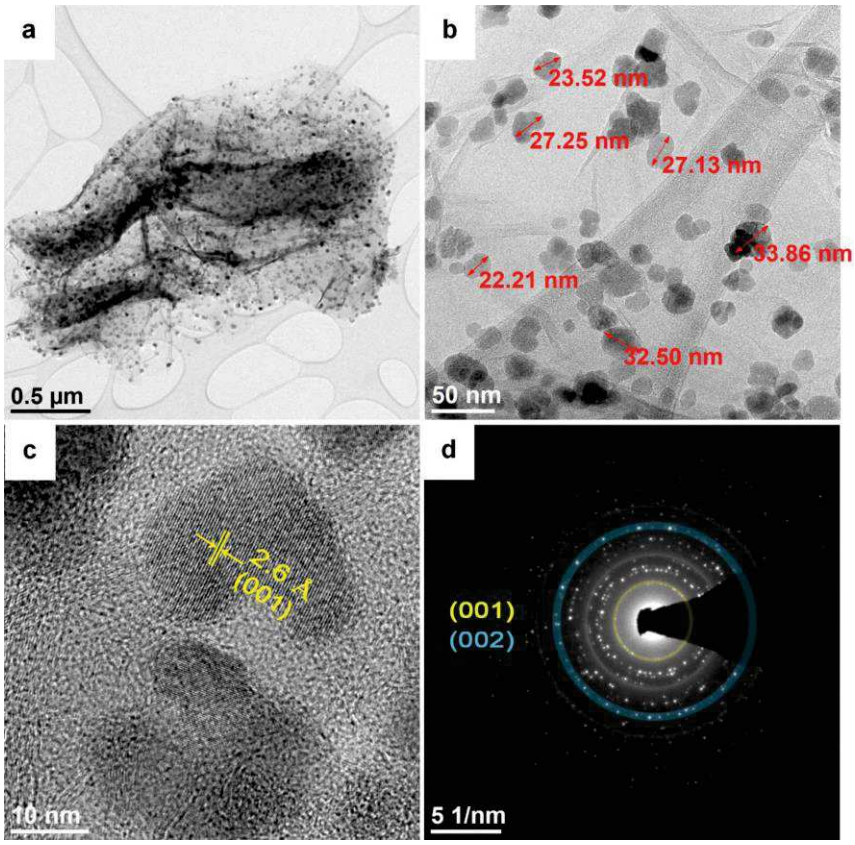

Fig. 6. TEM images (a, b, c) and SAED pattern of the freeze-dried 3DG-20 wt% VS_2

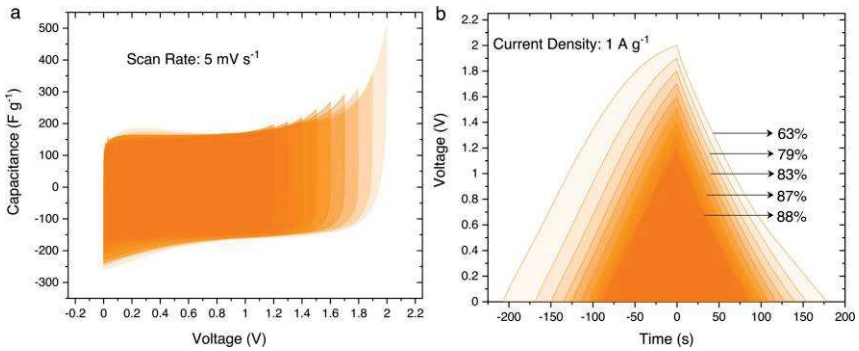

Fig. 7. Determination of the maximum operational voltage window of 3DG-20 wt% VS_2 in 1M $LiNO_3$: CV analysis at the scan rate of 5 mV s^{-1} (a) and GCD profile at the current density of 1 A g^{-1} (b).

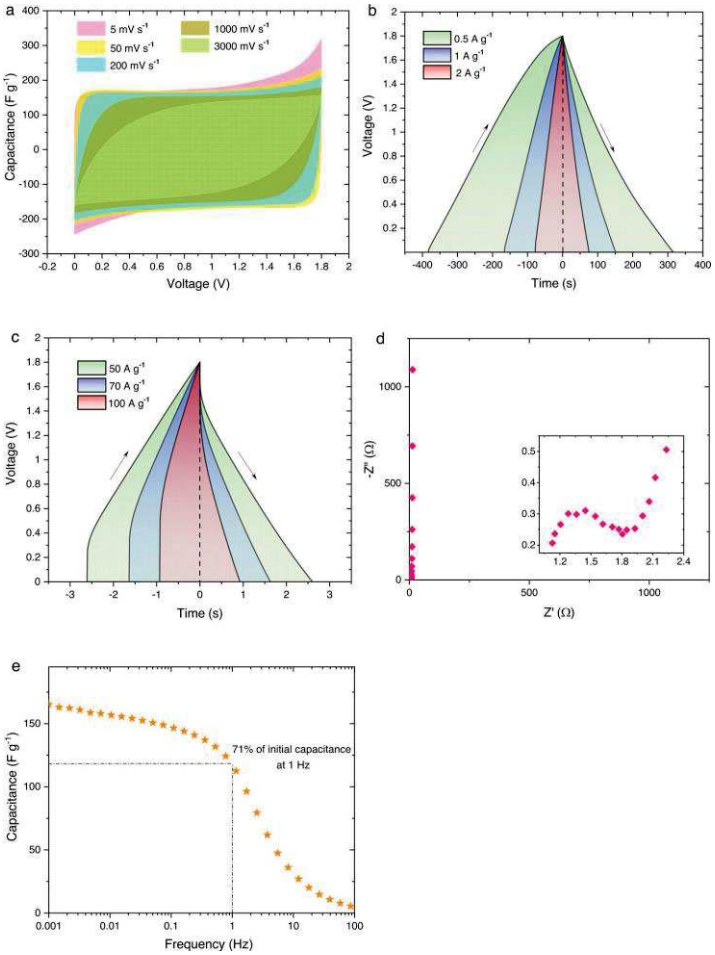

Fig. 8. Electrochemical performance of 3DG-20 wt% VS_2 in 1M $LiNO_3$: CV profile (a), GCD profile at low (b) and high (c) current density, EIS spectra (d), and variation of capacitance versus frequency (e).

Fig. 9a illustrates the CV plots recorded at 5 mV s^{-1} while the potential window is gradually extended.

As it can be seen, the negative electrode has a pure capacitive behavior with no apparent current rise following the extension of potential. The positive electrode showed a wide redox peak (hump) in the potential range of -0.1V to 0.4V that can be assigned to the bulk redox activities. However, the high broadness of this peak may indicate a combination of surface pseudocapacitive and bulk faradaic currents that are responsible for such a current rise. To determine the ratio of mentioned currents of the appeared hump (without contribution of electrical double layer (EDL), i.e., rectangular part), the power equation was employed [44]:

$$i_p = a\upsilon^b \tag{2}$$

where, i_p is the peak current in a specific potential *vs* Ag/AgCl, a and b are constant parameters, and υ is the scan rate. CV analysis in a broad range of scan rates was carried out for the positive electrode (Fig. 10a). The peak current in each scan rate was determined, and subsequently, a plot based on the log of i_p *vs* log of scan rate (υ) was drawn (Fig. 10b). The slope of the fitted line (b) can be in the range of 0.5 (bulk faradaic response) to 1 (surface pseudocapacitive). The slope of the fitted line (0.62) shows more bulk redox currents responsible for this peak.

To measure the contribution of capacitive and diffusion-controlled mechanisms in the total capacitance of the positive electrode, a plot based on the variation of capacitance *vs* $\upsilon^{-1/2}$ was drawn (Fig. 10c). The capacitance (C_{sp}) can be written as follow:

$$C_{sp} = \frac{1}{m\upsilon\Delta V}\int (I_{dc} + I_{dl})dV \tag{3}$$

Where m is the mass of the electrode, υ is scan rate, ΔV is the potential window. The diffusion-controlled current (I_{dc}) and the double-layer driven current (I_{dl}) are according to Eqs. (4) and (5), respectively [45]:

$$I_{dc} = k_1\upsilon^{1/2} \tag{4}$$

$$I_{dl} = k_2\upsilon \tag{5}$$

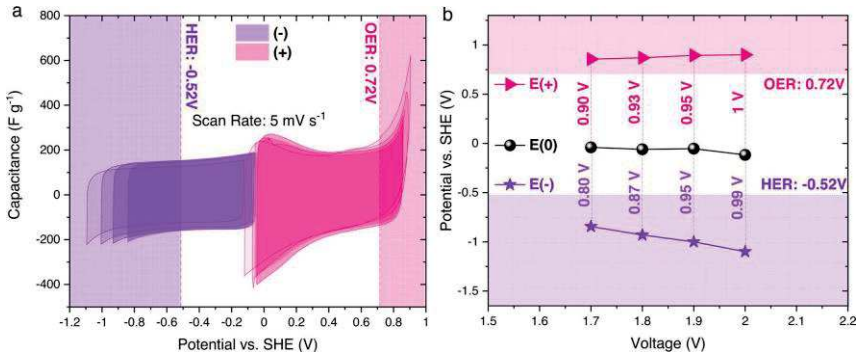

Fig. 9. Electrochemical performance of the EC cell based on 3DG-20 wt% VS_2 in 1M $LiNO_3$: CV of the positive and negative electrodes at 5 mV s^{-1} (a). Variation of the electrode potential vs. voltage along with the thermodynamic limit of O_2 and H_2 evolutions (b).

Therefore, Eq. (3) can be as follow:

$$C_{sp} = \frac{1}{m\upsilon\Delta V}\int k_1\upsilon^{1/2}dV + \frac{1}{m\upsilon\Delta V}\int k_2\upsilon\ dV \quad (6)$$

In Eq. (6), k_1, k_2, and υ are independent of the potential variation. Thus, this equation can be as follow:

$$C_{sp} = \frac{K_1}{m}\upsilon^{-\frac{1}{2}} + \frac{K_2}{m} \quad (7)$$

In this equation, $\frac{K_1}{m}\upsilon^{-\frac{1}{2}}$ and $\frac{K_2}{m}$ represent the capacitance as the result of the diffusion-controlled current and double-layer driven current, respectively.

Hence, a plot based on capacitance *vs* $\upsilon^{-1/2}$ was drawn. The intersection point of the fitted line with the vertical axis shows that 28% of the total capacitance from the positive electrode can be due to diffusion-controlled current.

This result further proves the low proportion of bulk to surface active sites in 3DG-20 wt% VS_2. Interestingly, both negative and positive electrodes showed no sign of oxygen and hydrogen evolution while crossing the thermodynamic limit of HER and OER. Especially, the 3DG-20 wt% VS_2 showed a stable capacitive performance under the negative polarization beyond the HER line. One probable reason may lie in the effect of anions on the stability of water molecules. Here, NO_3^- acts as a chaotropic agent to decrease the tendency of H-bonding among H_2O molecules. [19] In contrast to the theoretical potential value of hydrogen evolution, therefore, the cell can proceed to a wider potential range beyond the HER line. In agreement with the two-electrode cell experiments, no catalytic H_2 evolution was observed. The diagram on the right side shows that both electrodes work relatively in the same width of potential range (Fig. 9b). Expansion of the potential window to 2V led to a shift of both negative and positive potential ranges toward the negative values versus SHE, probably due to the electrolyte decomposition or the redox activity of by-products.

The proposed mechanism for the surficial redox reaction in 3DG-20 wt% VS_2 can be described as follow:

$$VS_2 + xLi^+ + xe^- \leftrightarrow VS_2^-Li^+_x \quad (8)$$

Fig. 11 schematically presents the structure of the vanadium disulfide layer as well as the proposed sites for adsorption of Li ions at the surface. It has been proven that monovalent cations such as Li^+ effectively can be adsorbed at the surface of the VS_2 lattice. Efficient adsorption at surface of VS_2 occurs while Li ions are placed at the top of S^{2-} ions. In this position, Li ions will be coordinated by three V ions. Irrespective of the type of the active sites, the adsorption requires a very small adsorption energy between -1.25 to -2.5 eV [46].

Generally, the assembled cell based on 3DG-20 wt% VS_2 operated in a higher voltage range (1.8 V) in comparison with that of 3DG (1.5 V). One of the probable reasons behind such improvement might be the effect of TAA on the substrate during the self-assembly and hybridization reaction. To gain an insight into this theory, 3DG in presence of TAA, with the same amount that was used during the preparation of 3DG-20 wt% VS_2, was prepared, and the sample was named 3DG-20 wt% TAA. Figure S11 represents the electrochemical performance of the sample. Interestingly, the CV profile of the substrate after reduction appears to be considerably different from the pristine CV profile of 3DG and parallel to that of 3DG-20 wt% VS_2 (Figure S11a). The first point to mention is the absence of voltage-dependent current increase that was already seen in the CV of 3DG. From the GCD plot (Figure S11b), the calculated specific capacitance is 131 F g^{-1}, which is lower than that of 3DG, 148 F g^{-1}, due to the loss of oxygen content. From Figure S11c-d it can be seen that 3DG-20 wt% TAA illustrated similar conductivity as that of 3DG-20 wt% VS_2. Figure S12 illustrates the electrochemical performance of 3DG-50 wt% VS_2 in a two-electrode cell. With the increase of the percentage of VS_2 to 50%, the electrode showed a considerable resistive behavior in comparison with that of 3DG-20 wt% VS_2 (Figure S12a). By increasing the dominancy of slow faradaic currents in the bulk, surface-based redox activities are no longer the main reason of energy storage within the cell. Considering the CV plot, there are two pairs of redox peaks at 0.55V and 0.85V. Figure S12b demonstrates the charge-discharge profiles which was recorded at low current density. Deviating from an ideal capacitive response, the sample showed a resistive behavior. Additionally, the cell showed a poor reversibility be gaining almost no charge, especially at the upper half of discharge plot. From the EIS spectra (Figure S12c), the slope of the Warburg line reveals high diffusion resistance against the penetration of ions to the pores. Tracing the variation of capacitance versus frequency, extracted from EIS plot, indicates a poor rate of charge propagation within 3DG-50 wt% VS_2 (Figure S12d). Such a high degree of VS_2 loading led to blockage of mesopores and loss of the interconnectivity of the porous framework which play a vital role in accumulation of the charge. To further specify the origin of the appeared peaks in the CV plot, a three-electrode cell investigation was carried out on 3DG-50 wt% VS_2 (Figure S13). The appeared peaks at 0.4V are assigned to the faradaic activity of V^{+4}/V^{3+} ions.[28] In addition, the cell based on 3DG-50 wt% VS_2 showed a limit potential range which is closer to the thermodynamic limits. The pro-

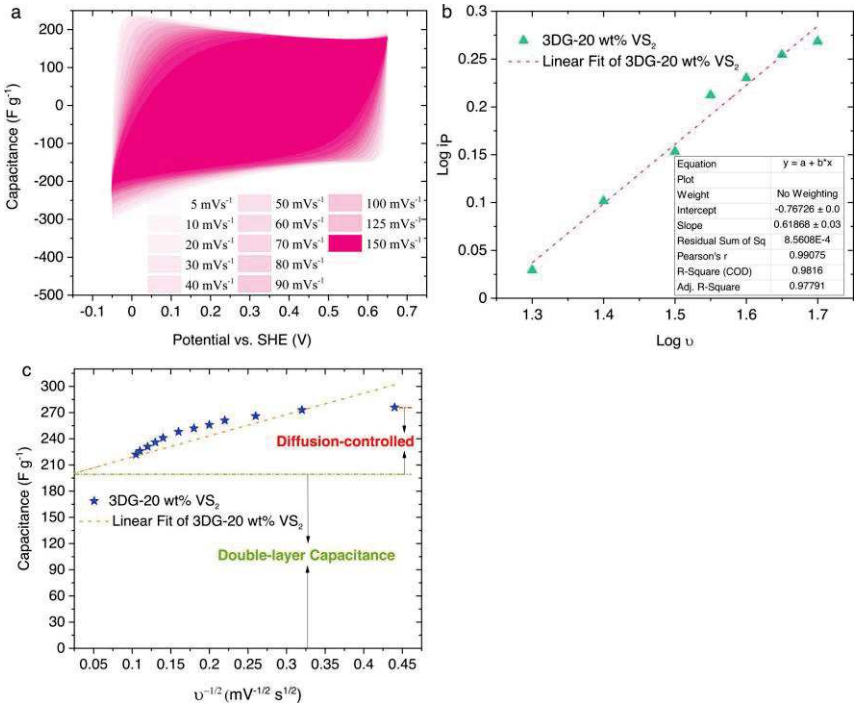

Fig. 10. Electrochemical performance of 3DG-20 wt% VS_2 as the positive electrode: CV profile in different scan rates (a). The variation of peak current *vs* scan rate, driven from the CV analysis (b). The variation of capactiance *vs* $\upsilon^{-1/2}$ was used to calculate double-layer capacitance and diffusion-controlled capacitance (c).

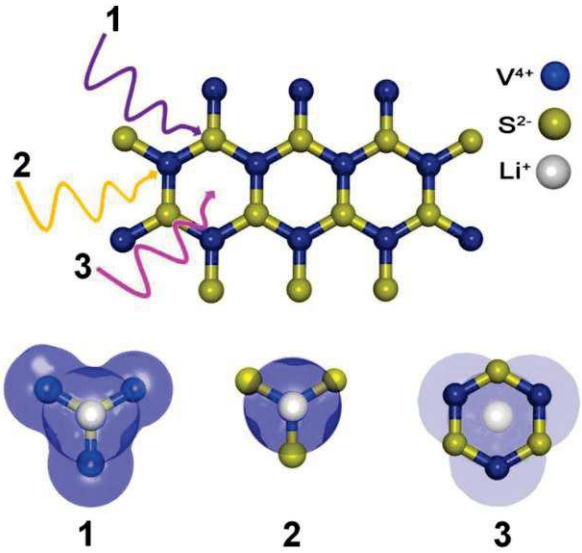

Fig. 11. Schematic representation of a VS_2 layer, including the proposed sites for adsorption of Li ions at the surface.

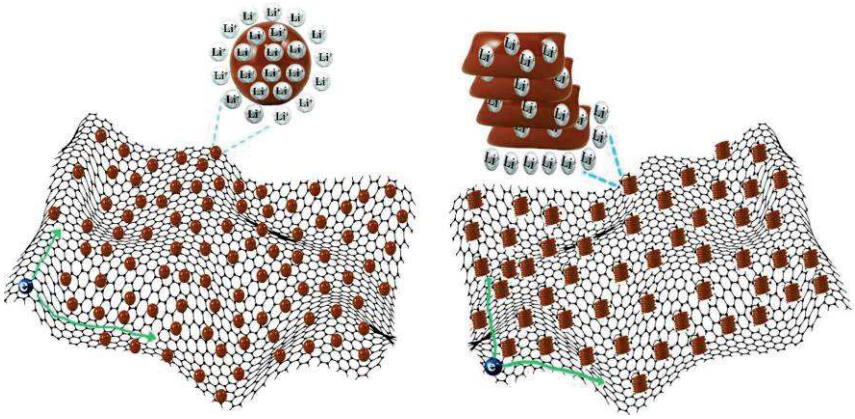

Fig. 12. Schematic representation of physical interaction in between ions and electrode materials in 3DG-20 wt% VS_2 (left) and 3DG-50 wt% VS_2 (right).

posed energy storage mechanism for insertion of ions in 3DG-50 wt% VS_2, can be described as follow:

$$xLi^+ + xe^- + VS_2 \leftrightarrow Li_xVS_2 \quad (9)$$

Fig. 12 compares the schematic representation of the proposed interactions that exist between ions and VS_2 in 3DG-20 wt% VS_2 and 3DG-50 wt% VS_2, respectively. In accordance with the obtained SEM results, VS_2 units (brown spheres) show a homogenous distribution and a proper distance from each other at the surface of graphene walls in 3DG-20 wt% VS_2. This arrangement allows the fast adsorption/desorption of electrolyte ions at the surface of the electrode. On the other hand, VS_2 units in 3DG-50 wt% VS_2 are grown over each other in a layered fashion. Such structure requires long-distance intercalation of ions to the internal space of VS_2 layers. It is worth mentioning that 3DG-VS_2 with 10%, 30%, and 40% of VS_2 were prepared, as well. However, the performance of the two first samples was similar to 3DG-20 wt% VS_2, while 3DG-40 wt% VS_2 showed a comparable performance to 3DG-50 wt% VS_2.

Figure S14 compares the performance of 3DG, 3DG-20 wt% TAA, 3DG-20 wt% VS_2, and 3DG-50 wt% VS_2. Considering the CV profiles, 3DG-20 wt% VS_2 showed a higher capacitance (164 F g^{-1}) than the other hybrid electrode and bare substrates. EIS analysis, recorded from 100 kHz to 1 mHz includes a semi-circle in higher frequency and a vertical line in low frequencies. The difference between the recorded equivalent series resistance is because of cell assembling. The pressure applied during cell construction was tuned to be maximum without destruction of the porous skeleton of the electrode materials. The power capability of the samples was further evaluated by drawing a plot based on the variation of capacitance values versus the frequency (Figure S14c). The specific capacitance values were calculated at 1 Hz to underline the rapid response of the electrodes. While 3DG-50 wt% VS_2 reached 21% of its initial capacitance, 3DG-20 wt% VS_2 was able to preserve 71% of

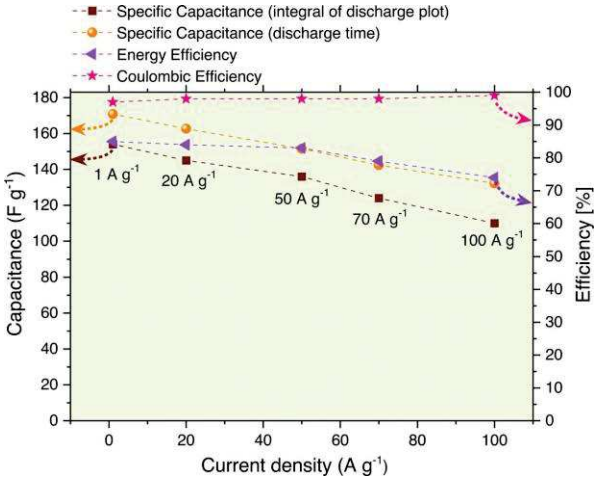

Fig. 13. Variation of specific capacitance, energy efficiency, and coulombic efficiency as the function of current density for 3DG-20 wt% VS_2.

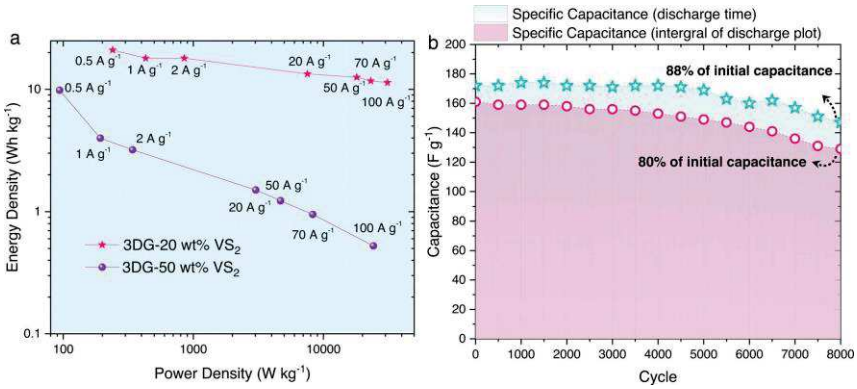

Fig. 14. Ragone plot of 3DG-20 wt% VS_2 and 3DG-50 wt% VS_2 (a). Capability of 3DG-20 wt% VS_2 at the current density of 1 A g^{-1} (b).

the initial capacitance recorded at 1 Hz. Fig. 13 indicates the variation of the specific capacitance, coulombic efficiency, and energy efficiency at different current densities for 3DG-20 wt% VS_2. The net variation of the specific capacitance and current density represents the high power capability of 3DG-20 wt% VS_2 from low to extremely high current densities. Another key point is to highlight the variation of coulombic efficiency and energy efficiency with the current density. In the case of 3DG-20 wt% VS_2, these values show a relatively similar and close variation with respect to the current density. Conversely, these values are not comparable in the case of 3DG-50 wt% VS_2 (Figure S15).

High power density materials show a typical, triangular shape of the GCD plots which leads to relatively similar coulombic and energy efficiency values. On the other hand, battery-like electrodes show slow charge propagation, and a smaller integral area of the discharge plot, especially in the upper half of the voltage window, which results in different coulombic and energy efficiencies. Fig. 14a illustrates the Ragone plot which is based on the calculated energy density and power density of the EC at the low current densities. 3DG-20 wt% VS_2 was delivering an energy density of 18 Wh kg^{-1} at the power density of 431 W kg^{-1}. On the other hand, 3DG-50 wt% VS_2 reached an energy density of 3.98 Wh kg^{-1} at the power density of 193 W kg^{-1}. To investigate the long-term stability of the optimum sample, 3DG-20 wt% VS_2 was subjected to repetitive charge-discharge cycles at 1 A g^{-1} while cycling continued till 20% of initial capacitance loss was observed.

Fig. 14b represens the obtained data from this analysis. 3DG-20 wt% VS_2 preserved 80% of its initial capacitance reaching 8000 cycles.

3. Conclusions

This work presents a rational pathway for integrating carbon-based electrodes and TMDs toward designing hybrid ECs with a high energy density without sacrificing their favorable power performance. Expanding the working voltage window of the cell was accomplished through adopting main strategies as follows: (i) designing a highly porous structure based on free-edge graphene walls which enhances the smoothness of the electrode surface, and reduces the possibility of aqueous medium decomposition. (ii) Adopting a capacitor-toward-battery approach rather than a battery-toward-capacitor one in designing the hybrid ECs by integrating VS_2 with an optimum amount which resulted in maintaining the initial, high power capability of the substrate, as well as reducing the rate of catalytic activities. (iii) Choosing the proper electrolyte, including an anion with a chaotropic nature, decreases the rate of H-bonding between the water molecules, and therefore, increases the stability of the aqueous medium beyond 1.23V. Employing the aforementioned strategies allowed the assembled cell based on the optimized composite electrode to deliver stable electrochemical performance in a wide range of working voltage up to 1.8V as well as 80% of capacitance retention after 8000 continuous charge-discharge cycles at 1 A g^{-1}. The hybrid electrode showed a supreme capacitive performance while demonstrating almost no resistance in a wide range of sweep rates from 5 mV s^{-1} to 3000 mV s^{-1}. Additionally, 3DG-20 wt% VS_2 showed a 71% of capacitance retention at the frequency of 1 Hz, which reveals the superfast response of the hybrid electrode. Finally, the cell reached a high energy density of 18 Wh kg^{-1} at the power density of 430 W kg^{-1} at a current density of 1 A g^{-1}, while at 100 A g^{-1} the hybrid electrode reached an energy density of 12 Wh kg^{-1} at the high power density of 31000 W kg^{-1}. Enhancing the energy density of the prepared ECs with preserving its favorable power rate gives a reasonable way towards energy storage applications.

Declaration of Competing Interest

The authors declare no conflict of interest.

CRediT authorship contribution statement

Masoud Foroutan Koudahi: Conceptualization, Methodology, Data curation, Investigation, Writing – original draft. **Elżbieta Frąckowiak:** Supervision, Conceptualization, Data curation, Writing – review & editing.

Acknowledgements

The authors would like to acknowledge OPUS project financed by National Science Centre, Poland (project no. 2018/31/B/ST4/01852) for the financial support of the research.

Supplementary materials

Supplementary material associated with this article can be found, in the online version, at doi:10.1016/j.ensm.2022.04.021.

References

[1] E. Frackowiak, F. Beguin, Supercapacitors: Materials, Systems and Applications, Wiley VCH Verlag GmbH & Co, 2013.
[2] F. Bu, W. Zhou, Y. Xu, Y. Du, C. Guan, W. Huan, Recent developments of advanced micro-supercapacitors: design, fabrication and applications, Npj Flexible Electronics 4 (2020) 1–16, doi:10.1038/s41528-020-00093-6.

[3] C. Choi, D.S. Ashby, D.M. Butts, R.H. DeBlock, Q Wei, J. Lau, B. Dunn, Achieving high energy density and high power density with pseudocapacitive materials, Nature Reviews Materials 5 (2020) 5–19, doi:10.1038/s41578-019-0142-z.
[4] A. Platek-Mielczarek, E. Frackowiak, K. Fic, Specific carbon/iodide interactions in electrochemical capacitors monitored by EQCM technique, Energy & Environmental Science 14 (2021) 2381–2393, doi:10.1039/D0EE03867A.
[5] S. Manoharan, K. Krishnamoorthy, A. Sathyaseelan, S. Kim, High-power graphene supercapacitors for the effective storage of regenerative energy during the braking and deceleration process in electric vehicles, Materials Chemistry Frontiers 5 (2021) 6200–6211, doi:10.1039/D1QM00465D.
[6] E. Frąckowiak, M. Foroutan Koudahi, M. Tobis, Electrochemical Capacitor Performance of Nanotextured Carbon/Transition Metal Dichalcogenides Composites, Small 17 (2021) 2006821-1-2006821-10, doi:10.1002/smll.202006821.
[7] C.R. Chen, H. Qin, H. Cong, S. Yu, A highly stretchable and real-time healable supercapacitor, Advanced Materials 31 (2019) 1900573, doi:10.1002/adma.201900573.
[8] P. Simon, Y. Gogotsi, Materials for electrochemical capacitors, Nature Materials (2010) 320–329, doi:10.1038/nmat2297.
[9] X. Aeby, A. Poulin, G. Siqueira, M.K. Hausmann, G. Nystrom, Fully 3D Printed and Disposable Paper Supercapacitors, Advanced Materials (2021) 2101328, doi:10.1002/adma.202101328.
[10] P. Simon, Y. Gogotsi, Perspectives for electrochemical capacitors and related devices, Nature Materials 19 (2020) 1151–1163, doi:10.1038/s41563-020-0747-z.
[11] X. Wu, B. Huang, Wang Q, Y. Wang, Wide potential and high energy density for an asymmetric aqueous supercapacitor, Journal of Materials Chemistry A 7 (2019) 19017–19025, doi:10.1039/C9TA06428A.
[12] L. Lyu, W. Hooch Antink, B. Lee, C. Kim, E. Jung, K. Seong, T. Hyeon, Y. Piao, Zeolitic Imidazole Framework Sacrificial Template-Assisted Synthesis of NiCoP Nanocages Doped with Multiple Metals for High-Performance Hybrid Supercapacitors, ACS Applied Energy Materials 4 (2021) 10553–10564, doi:10.1021/acsaem.1c01493.
[13] Z. Wu, D. Chen, L. Li, L. Wang, A universal electrochemical lithiation–delithiation method to prepare low-crystalline metal oxides for high-performance hybrid supercapacitors, RSC Advances 11 (2021) 30407–30414, doi:10.1039/D1RA05814B.
[14] L. Lin, W. Lei, S Zhang, Y. Liu, G. Wallace, J. Chen, Two-dimensional transition metal dichalcogenides in supercapacitors and secondary batteries, Energy Storage Materials 19 (2019) 408–423, doi:10.1016/j.ensm.2019.02.023.
[15] Q. Yun, L. Li, Z. Hu, Q. Lu, B. Chen, H. Zhang, Layered transition metal dichalcogenide-based nanomaterials for electrochemical energy storage, Advanced Materials 32 (2020) 1903826, doi:10.1002/adma.201903826.
[16] B. Anasori, M.R. Lukatskaya, Y. Gogotsi, 2D metal carbides and nitrides (MXenes) for energy storage, Nature Reviews Materials 2 (2017) 1–17, doi:10.1038/natrevmats.2016.98.
[17] M. Tobis, S. Sroka, E. Frackowiak, Supercapacitor with Carbon/MoS2 Composites, Frontiers in Energy Research 9 (2021) 647878-1-647878-11, doi:10.3389/fenrg.2021.647878.
[18] K.S. Kumar, N. Choudhary, D. Pandey, Y. Ding, L. Hurtado, H. Chung, L. Tetard, Y. Jung, J. Thomas, Investigating 2D WS2 supercapacitor electrode performance by Kelvin probe force microscopy, Journal of Materials Chemistry A 8 (2020) 12699–12704, doi:10.1039/D0TA03383A.
[19] S. Thareja, A. Kumar, Water-In-Salt" Electrolyte-Based High-Voltage (2.7 V) Sustainable Symmetric Supercapacitor with Superb Electrochemical Performance—An Analysis of the Role of Electrolytic Ions in Extending the Cell Voltage, ACS Sustainable Chemistry & Engineering 9 (2021) 2338–2347, doi:10.1021/acssuschemeng.0c08604.
[20] K. Nomura, H. Nishihara, N. Kobayashi, T. Asada, T. Kyotani, 4.4 V supercapacitors based on super-stable mesoporous carbon sheet made of edge-free graphene walls, Energy & Environmental Science 12 (2019) 1542–1549, doi:10.1039/C8EE03184C.
[21] A. Khazaeli, G. Godbille-Cardona, D.P. Barz, A Novel Flexible Hybrid Battery–Supercapacitor Based on a Self-Assembled Vanadium-Graphene Hydrogel, Advanced Functional Materials 30 (2020) 1910738, doi:10.1002/adfm.201910738.
[22] E. Meyer, A. Bede, D. Mutukwa, R. Taziwa, N. Zingwe, Optimization, and analysis of carbon supported VS2 nanocomposites as potential electrodes in supercapacitors, Journal of Energy Storage 27 (2020) 101074, doi:10.1016/j.est.2019.101074.
[23] A.V. Murugan, M. Quintin, M. Delville, G Campet, K. Vijayamohanan, Entrapment of poly (3, 4-ethylenedioxythiophene) between VS2 layers to form a new organic–inorganic intercalative nanocomposite, Journal of Materials Chemistry 15 (2005) 902–909, doi:10.1039/B414922J.
[24] Z. Huang, X. Han, X. Cui, C. He, J. Zhang, X. Wang, Z. Lin, Y. Yang, Vertically aligned VS 2 on graphene as a 3D heteroarchitectured anode material with capacitance-dominated lithium storage, Journal of Materials Chemistry A 8 (2020) 5882–5889, doi:10.1039/C9TA13835H.
[25] M. Kan, B. Wang, Y. Lee, Q. Sun, A density functional theory study of the tunable structure, magnetism and metal-insulator phase transition in VS2 monolayers induced by in-plane biaxial strain, Nano Res 8 (2014) 1348–1356, doi:10.1007/s12274-014-0626-5.
[26] L. Zhang, D. Sun, Q. Wei, H. Ju, J. Feng, J Zhu, L. Mai, E. Cairns, J. Guo, Understanding the electrochemical reaction mechanism of VS2 nanosheets in lithium-ion cells by multiple in situ and ex situ x-ray spectroscopy, Journal of Physics D: Applied Physics 51 (2018) 494001.
[27] W.A. Haider, M. Tahir, L. He, W. Yang, A. Minhas-khan, K. Owusu, Y. Chen, X. Hong, L. Mai, Integration of VS2 nanosheets into carbon for high energy density micro-supercapacitor, Journal of Alloys and Compounds 823 (2020) 151769, doi:10.1016/j.jallcom.2019.151769.
[28] T.M. Masikhwa, F. Barzegar, J.K. Dangbegnon, A. Bello, M.J. Madito, D. Momodu, N. Manyala, Asymmetric supercapacitor based on VS 2 nanosheets and activated carbon materials, RSC advances 6 (2016) 38990–39000, doi:10.1039/C5RA27155J.
[29] Q. Ji, C. Li, J. Wang, J. Niu, Y. Gong, Z. Zhang, Q. Fang, Y. Zhang, J. Shi, L. Liao, X. Wu, L. Gu, Z. Liu, Y. Zhang, Metallic vanadium disulfide nanosheets as a platform material for multifunctional electrode applications, Nano Letters 17 (2017) 4908–4916, doi:10.1021/acs.nanolett.7b01914.
[30] B. Pandit, L.K. Bommineedi, B.R. Sankapal, Electrochemical engineering approach of high performance solid-state flexible supercapacitor device based on chemically synthesized VS2 nanoregime structure, Journal of Energy Chemistry 31 (2019) 79–88.
[31] H. Wang, L. You, Y. Guan, H. Wang, Rational fabrication of flower-like VS2-decorated Ti3C2 MXene heterojunction nanocomposites for supercapacitance performances, Colloids and Surfaces A: Physicochemical and Engineering Aspects 629 (2021) 127381 doi:10.1016/j.colsurfa.2021.127381.
[32] B. Archana, N. Kottam, C.S. KB, Synthesis, characterization and supercapacitor electrode performances of VS2 nanosheets, Materials Today: Proceedings 46 (2021) 545–549, doi:10.1016/j.matpr.2020.10.746.
[33] P. Ratajczak, F. Béguin, A High-Voltage Electrochemical Cell Operating with Two Aqueous Electrolytes of Different pH Values, ChemElectroChem 5 (2018) 2518–2521, doi:10.1002/celc.201800778.
[34] M. Foroutan, L. Naji, Systematic evaluation of factors influencing electrochemical and morphological characteristics of free-standing 3D graphene hydrogels as electrode material for supercapacitors, Electrochimica Acta 301 (2019) 421–435, doi:10.1016/j.electacta.2019.01.161.
[35] G.J. Rani, K.J. Babu, M.J. Rajan, Watsonia meriana flower like Fe3O4/reduced graphene oxide nanocomposite for the highly sensitive and selective electrochemical sensing of dopamine, Journal of Alloys and Compounds 688 (2016) 500–512, doi:10.1016/j.jallcom.2016.07.101.
[36] X. Chen, N. Li, Y. Rong, Y. Hou, Y. Huang, W. Liang, β-Cyclodextrin functionalized 3D reduced graphene oxide composite-based electrochemical sensor for the sensitive detection of dopamine, RSC Advances 11 (2021) 28052–28060, doi:10.1039/D1RA02313F.
[37] Q. Yu, L.A. Jauregui, W. Wu, R. Colby, J. Tian, Z. Su, H. Cao, Z. Liu, D. Pandey, D. Wei, T.F. Chung, P. Peng, N.P. Guisinger, E.A. Stach, J. Bao, S-S. Pei, Y.P. Chen, Control and characterization of individual grains and grain boundaries in graphene grown by chemical vapour deposition, Nature Materials 10 (2011) 443–449, doi:10.1038/nmat3010.
[38] P. He, m. Yan, G. Zhang, R. Sun, L. Chen, Q. An, L. Mai, Layered VS2 nanosheet-based aqueous Zn ion battery cathode, Advanced Energy Materials 7 (2017) 1601920, doi:10.1002/aenm.201601920.
[39] X. Zhang, Q. He, X. Xu, T. Xiong, Z. Xiao, J. Meng, X. Wang, L. Wu, J. Chen, L. Mai, Advanced Energy Materials, Insights into the Storage Mechanism of Layered VS2 Cathode in Alkali Metal-Ion Batteries 10 (2020) 1904118, doi:10.1002/aenm.201904118.
[40] J.-C. Liu, Z.-H. Huang, T.-Y. Ma, Aqueous supercapacitor with ultrahigh voltage window beyond 2.0 volt, Small Structures 1 (2020) 2000020, doi:10.1002/sstr.202000020.
[41] B. Pandit, S.S. Karade, B.R. Sankapal, Sankapal, Hexagonal VS2 anchored MWCNTs: first approach to design flexible solid-state symmetric supercapacitor device, ACS applied materials & interfaces 9 (2017) 44880–44891, doi:10.1021/acsami.7b13908.
[42] Y. Xu, Z. Lin, X. Zhong, X. Huang, N.O. Weiss, Y. Huang, X. Duan, Holey graphene frameworks for highly efficient capacitive energy storage, Nature Communications 5 (2014) 1–8, doi:10.1038/ncomms5554.
[43] E. Frackowiak, Carbon materials for supercapacitor application, Physical Chemistry Chemical Physics 9 (2007) 1774–1785, doi:10.1039/B618139M.
[44] V. Augustyn, J. Come, M.A. Lowe, J.W. Kim, P-L. Taberna, S.H. Tolbert, H.D. Abruna, P. Simon, B. Dunn, High-rate electrochemical energy storage through Li+ intercalation pseudocapacitance, Nature Materials 12 (2013) 518–522, doi:10.1038/nmat3601.
[45] W. Yan, T. Ayvazian, J. Kim, Y. Liu, K.C. Donavan, W. Xing, Y. Yang, J.C. Hemminger, R.M. Penner, Mesoporous Manganese Oxide Nanowires for High-Capacity, High-Rate, Hybrid Electrical Energy Storage, ACS Nano 5 (2011) 10 8275-8287, doi:10.1021/nn2029583.
[46] D. Wang, Y. Liu, X. Meng, Y. Wei, Y. Zhao, Q. Pang, G. Chen, Two-dimensional VS_2 monolayers as potential anode materials for lithium-ion batteries and beyond: first-principles calculations, Journal of Materials Chemistry A 5 (2017) 21370–21377, doi:10.1039/C7TA06944H.

5. Article 3

Title: ***$Ti_3C_2T_x$ MXene as Intriguing Material for ElectrochemicalCapacitor***

Authors: Masoud Foroutan Koudahi, Elżbieta Frąckowiak

Journal: Small

DOI: https://doi.org/10.1002/smll.202307165

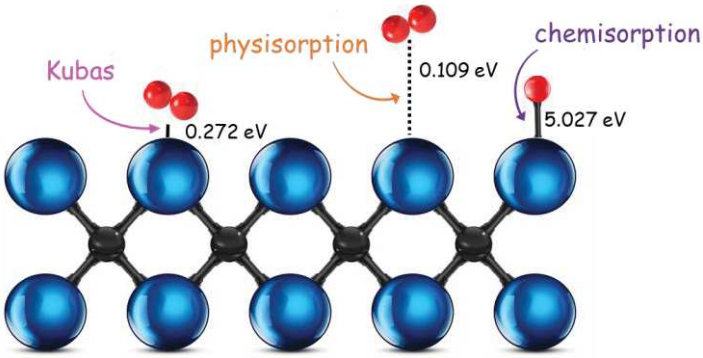

Motivation

MXenes are an interesting class of 2D layered materials that have been investigated frequently as the EC electrode. However, the main focus was on their charge storage response in a narrow range of negative potentials and there was no information regarding the performance of MXenes in a full cell. The mechanism behind the hydrogen storage of titanium carbides was remained unclear, and therefore, this study aimed to elucidate it. For this purpose, it was needed to evaluate the electrochemical response of MXenes in aqueous media with different pH to understand its effect on the hydrogen adsorption/desorption. In addition, it was necessary to understand the type of interactions by which hydrogen atoms or molecules are adsorbed at the surface of MXenes. Furthermore, the working voltage of MXene-based ECs was severely limited. Hence, it was important to find alternatives for realizing cells with efficient, wide voltage operating.

Careful evaluation of electrochemical interactions at the electrode/electrolyte interface, provided us with key information regarding the severe charge and potential imbalance between the negative and positive electrode. It was found that titanium

carbide MXenes are exclusively active at the negative potentials, where a combination of capacitive and faradaic currents (hydrogen electrosorption) contribute to the energy storage. Different mechanism was suggested for the nature of interactions that are involved in the hydrogen storage of MXenes.

The cell voltage significantly was improved by realizing asymmetric ECs based on MXenes as a negative electrode and positive electrode in the form of activated carbon. In this case, a very wide working voltage (2V) in neutral electrolyte was obtained. Long-term cyclability of the cell was reached with 80% of its initial capacitance value after 22000 cycles.

RESEARCH ARTICLE

NANO · MICRO small
www.small-journal.com

$Ti_3C_2T_x$ MXene as Intriguing Material for Electrochemical Capacitor

*Masoud Foroutan Koudahi and Elżbieta Frąckowiak**

This study provides meaningful insight into the charge storage in $Ti_3C_2T_x$ MXene (M-transition metal, X-carbon, T-Cl, F, O) for electrochemical capacitor (EC) application. The experiments show that this 2D material is especially adapted for the hydrogen electrosorption under negative polarization. It is found that hydrogen bonding to the $Ti_3C_2T_x$ surface occurs through interactions of various strength. Different mechanisms are suggested to explain the nature of H stored at the electrode/electrolyte interface depending on pH and potential range. For the negative potentials, both capacitive and faradaic currents are involved, and the electrode can operate in a relatively wide range. On the other hand, the narrow range of positive potentials limits whole voltage of EC. Such charge disproportion has a major impact on the performance failure of symmetric MXene-based ECs. New design of MXene cells with a wide operating voltage is introduced. To equalize the charge storage of both electrodes, the positive $Ti_3C_2T_x$ electrode is replaced by the porous carbon (BP2000) with a wide working potential and a good capacitive response. Thus, EC operating voltage is considerably expanded to 1.3, 1.4, 2 V in acidic, basic, neutral medium, respectively. During cycling tests at 1 A g^{-1}, the asymmetric cell MXene/BP2000 maintains 80% of initial capacitance after 22 000 cycles.

1. Introduction

Today's world is facing an urgent need for replacing fossil fuels with clean and renewable energies. Considerable market demand is based on portable electronic applications, and therefore, having safe and reliable energy storage devices is essential. Electrochemical capacitors (ECs) store energy by reversible adsorption/desorption of ions at the electrode surface. Following such non-faradaic mechanism, ECs deliver a high power response but moderate energy in a wide voltage range.[1] In recent years, many studies have been dedicated to improving the energy output of ECs. The contribution of faradaic currents through integrating pseudocapacitive and carbon materials,[2,3] doping heteroatoms,[4] and grafting redox active functionalities at the surface[5] enhance the capacitance of the cell. Electrochemical hydrogen storage play an important role for batteries, e.g., Ni/MHs, fuel cells, supercapacitors.[6] Materials with the high ability to store hydrogen can improve the energy storage of a system. MXenes (M-transition metal, X-C or N) are a new 2D family as promising hydrogen storage host.[7,8] Different interactions are responsible for hydrogen storage in MXenes. Generally, in 2D materials the hydrogen storage can proceed by physisorption, chemisorption, or Kubas interactions.[9,10] In physisorption, molecular hydrogen is adsorbed at the surface by the weak van der Waals interactions. 2D carbons such as multi-layered graphene (3–6 stacked flakes) store hydrogen by the van der Waals forces with a gravimetric storage capacity of 0.85 wt%.[11] However, the binding enthalpy of H_2 molecules with the graphene surface (2-10 kJ mol^{-1}) is insufficient and below the calculated ideal enthalpy (20–30 kJ mol^{-1}).[12] Chemisorption consists of three stages, including evolution and subsequent dissociation of molecular hydrogen, followed by a strong chemical sorption of hydrogen atoms. Carbon electrodes store hydrogen by adsorption of hydrogen originated from the reduction of hydronium ions (in acidic media) or the water molecules (in basic/neutral media).[13] Strong binding is possible through Kubas bondings, where the elongated hydrogen molecules (σ orbitals) and the metallic adsorbent (π orbitals) form a complex.[14] In terms of the bonding strength, this interaction can be placed between physisorption and chemisorption. As already mentioned, MXenes are the recent member of 2D layered materials that show a promising hydrogen storage performance even beyond the designated U.S. DOE target (5.5 wt%). A theoretical survey indicates the total storage capacity of 8.5 wt% for Ti_2C, including 3.4 wt%, 1.7 wt%, and 3.4 wt% of the share for physisorption, chemisorption, and Kubas interactions.[15] MXenes are made of transition metals (Ti, Nb, Mo, etc.) that are intervened by carbon or nitrogen layers. Such combination allows MXenes to offer a high conductivity and storing performance for energy applications.[16–18] The removal of aluminum from the MAX (M-transition metal, A-Al, X-C or N) phase provides a tunable interlayer spacing[19] for ionic or molecular insertion. Using etchants during the top-down preparation leads to the formation of various functional groups at the surface, which can be further optimized.[20] Some theoretical

M. F. Koudahi, E. Frąckowiak
Institute of Chemistry and Technical Electrochemistry
Poznan University of Technology
Poznan 60-965, Poland
E-mail: elzbieta.frackowiak@put.poznan.pl

The ORCID identification number(s) for the author(s) of this article can be found under https://doi.org/10.1002/smll.202307165

DOI: 10.1002/smll.202307165

 © 2023 Wiley-VCH GmbH

ADVANCED SCIENCE NEWS
www.advancedsciencenews.com

NANO · MICRO small
www.small-journal.com

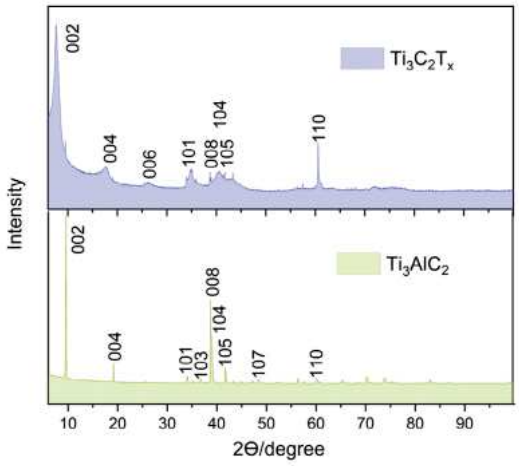

Figure 1. XRD characterization of Ti_3AlC_2 and $Ti_3C_2T_x$.

modeling was carried out to explain the storage performance of MXenes.[15,21] However, there are only few experimental studies related to the storage mechanism or the nature of interaction that occurs between hydrogen and MXene surface.

In this paper, MXene ($Ti_3C_2T_x$) material (T-Cl, F, O), originating from MAX (Ti_3AlC_2), was investigated physicochemically and electrochemically in detail. The hydrogen storage in titanium carbide has been studied by cyclic voltammetry, impedance spectroscopy, and galvanostatic charge–discharge in different aqueous electrolytes with various pH values. Characteristics reveal that hydrogen is stored in MXenes through different interactions. Depending on the bonding strength, each interaction occurs in a specific potential that can be detected in the voltammogram. Furthermore, the acquired information provided a comprehensive explanation regarding the reaction overpotential of titanium carbide.[22,23] A big difference between the capacity of the negative and positive electrodes has the main impact on cell performance being at the origin of the low EC voltage. To address this problem, we demonstrated that the working voltage of MXene-based ECs can be substantially expanded by selecting electrode materials with proper charge response and working potential. The assembled asymmetric cells were operating in a wider voltage range, compared to their symmetric counterparts. In the case of the asymmetric EC in 1 M Li_2SO_4, the cell showed a stable and long lifespan at the high voltage.

2. Results

2.1. Physicochemical Characterization

To evaluate the expansion degree of the prepared $Ti_3C_2T_x$, XRD analysis was carried out (**Figure 1**). Shifting the location of the 002 peak can be assigned to the successful delamination of the MAX phase to its respective MXene.[24] Using Bragg's law, a corresponding c lattice value was increased from 4.626 Å in Ti_3AlC_2 to 5.814 Å in the case of the $Ti_3C_2T_x$. The intensity of 104 peak in $Ti_3C_2T_x$ shows a considerable decrease in comparison with that in the MAX phase, which is due to the successful removal of aluminum.[25]

The quantitative analysis of the $Ti_3C_2T_x$ surface was performed by XPS analysis (**Figure 2**). MAX compound Ti_3AlC_2 spectra are shown in Figure S1 (Supporting Information). Surface concentrations of chemical bonds obtained from fitting XPS data for all analyzed samples are listed in Table S1 (Supporting Information). The Ti 2p spectra of $Ti_3C_2T_x$ (**2a**) and Ti_3AlC_2 (**S1a**) can be fitted with three 2p doublet structures ($p_{3/2}$–$p_{1/2}$ doublet separation equals 5.2 eV for Ti^{3+} state, 5.7 eV for the Ti^{4+} state and 5.6 eV for TiC) originating from the three different states of Ti. Titanium is found mainly in TiC which appears as a $2p_{3/2}$ centered at 455.0 eV, secondly there is visible Ti^{3+} oxidation state from Ti_2O_3 or TiF or TiCl expressed with $2p_{3/2}$ line at 456.6 eV (**2a**) and the line at 458.8 eV indicates the presence of Ti^{4+} state in TiO_2.[26–28] The Al 2p spectrum of Ti_3AlC_2 (**S1b**) was fitted with two doublet structures (doublet separation $p_{3/2}$–$p_{1/2}$ equals 0.4 eV) with first main $2p_{3/2}$ line centered at 72.1 eV which indicates metallic aluminum and second $2p_{3/2}$ line at 74.5 eV which specifies Al^{3+} oxidation state most likely in Al_2O_3 or $Al(OH)_3$.[29] The C 1s spectra of $Ti_3C_2T_x$ (**2b**) and Ti_3AlC_2 (**S1c**) can be fitted with three components: first line positioned at 281.7 eV which indicates Ti-C carbide, second line at 285.0 eV shows presence of aliphatic carbon C-C and/or C = C type bonds and last line at 289.1 eV which originates from O-C = O type bonds.[30] The O 1s spectra of $Ti_3C_2T_x$ (**2c**) and Ti_3AlC_2 (**S1d**) were fitted with two components: first line centered at 530.1 eV which indicates mainly metal oxides like O-Ti and O-Al or organic species containing O = C type bonds and second line at 531.8 eV from either metal hydroxides and/or some part of O = C organic bonds and O-Si bonds.[26] The Cl 2p spectrum of $Ti_3C_2T_x$ (**2d**) was fitted with one doublet structure (doublet separation $p_{3/2}$–$p_{1/2}$ equals 1.6 eV) with main $2p_{3/2}$ line centered at 199.1 eV which proves presence of Cl^- ions in TiCl.[26]

Fluorine 1s spectrum (**2e**) was fitted with a single line positioned at 684.9 eV which points out the presence of F^- ions in TiF_x.[26] **Figure 3** presents the cross-sectional SEM images taken from Ti_3AlC_2 (**3a**) and $Ti_3C_2T_x$ (**3b**). The MAX phase has a dense structure made of strongly stacked layers with no available interlayer space. In addition, MAX particles have a broad range of size. Etching of the aluminum resulted in delaminated $Ti_3C_2T_x$ flakes with better accessibility to the interior surface and interlayer space, however, a part of the bulk grains was left partially untreated by the etchant.

In general, the flakes are relatively thin and they are made of a few stacked $Ti_3C_2T_x$ layers. However, the random nature of the etching process leads to the presence of thicker $Ti_3C_2T_x$ made of more layers.

The elemental mapping of the MAX and MXene phases are presented in Figures S2 and S3 (Supporting Information), including the EDS results together with the elemental analysis. The homogenous dispersion of Ti, C, F, and Cl can be noticed in the prepared MXene. The decrease of the aluminum amount from 21% to 2% correlates with the observed delaminated structure of the MXene. In addition, the amount of chlorine from 2% in Ti_3AlC_2 was increased to 7% in titanium carbide which can be taken as the dominancy of the Cl terminals at the surface of Ti layers. Figure 3c,d shows a cross-section of the electrodes prepared from $Ti_3C_2T_x$. Obviously, a binder (PTFE) and conductive additive

 © 2023 Wiley-VCH GmbH

ADVANCED SCIENCE NEWS
www.advancedsciencenews.com

NANO · MICRO small
www.small-journal.com

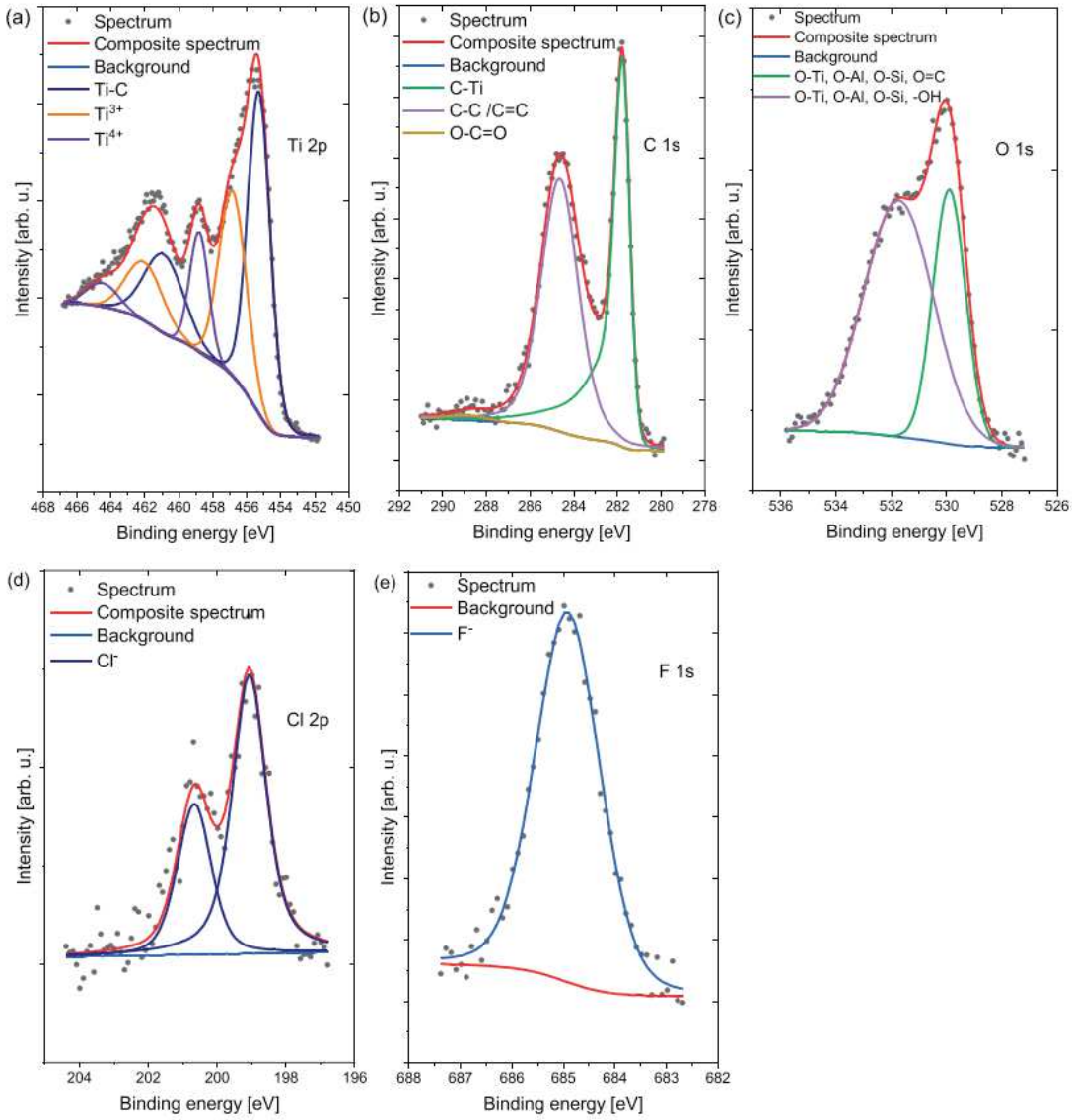

Figure 2. XPS spectra of $Ti_3C_2T_x$ including, Ti 2p (a), C 1s (b), O 1s (c), Cl 2p (d), and F 1s (e).

modify the electrode morphology. Nitrogen sorption isotherms in **Figure 4** present the surface area and pore size distribution of the samples. Delamination of MAX phase leads to an increase of the accessible surface area of the MXene. From the SEM images, the presence of untreated MAX grains was noticed. This means that the resulting particles have a broad range of distribution. Therefore, the delaminated particles were separated from the untreated ones for further analysis. For this purpose, the MXene aqueous dispersion was subjected to centrifugation at 3500 rpm for 1 h, and the supernatant, containing fine MXene layers, was separated after the precipitation. BET analysis on the dried supernatant shows the surface area of 24 $m^2\ g^{-1}$ that is considerably higher than the average surface area (4 $m^2\ g^{-1}$). Previously reported N_2 isotherm of $Ti_3C_2T_x$ demonstrates also that adsorption and desorption proceeds with different energy.[31] We have also performed a nitrogen sorption on the prepared electrodes. Specific surface area of the electrodes was comparable to SSA of pure $Ti_3C_2T_x$ and it was equal to 10 $m^2\ g^{-1}$.

 © 2023 Wiley-VCH GmbH

ADVANCED SCIENCE NEWS
www.advancedsciencenews.com

NANO · MICRO small
www.small-journal.com

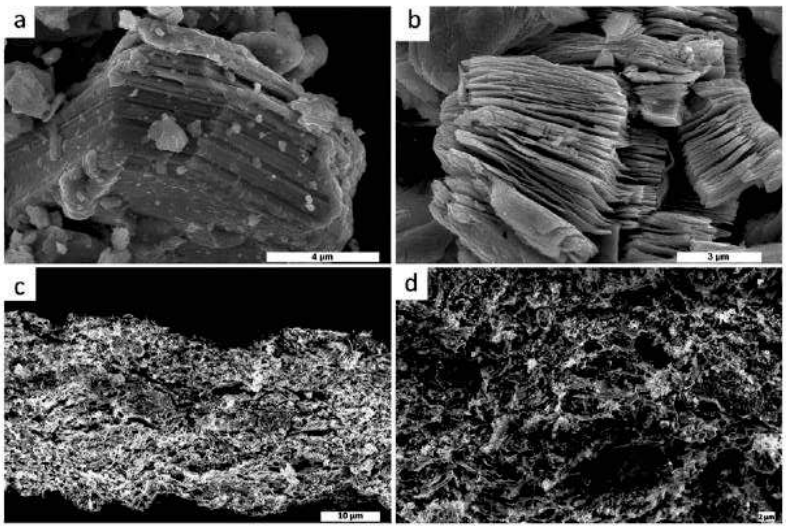

Figure 3. SEM images of Ti_3AlC_2 (a) and $Ti_3C_2T_x$ (b). Cross-section of $Ti_3C_2T_x$ electrode (c), (d).

2.2. Electrochemical Characterization

In the first step, the voltage stability of two-electrode symmetric cells based on titanium carbide in different aqueous media was evaluated. In 1 M H_2SO_4, the cell showed a pure capacitive behavior up to 0.5 V (**Figure 5a**). However, the expansion of the voltage from 0.5 to 0.9 V resulted in a stepwise change of mechanism into the strong faradaic response. Further extension beyond 0.9 V led to a severe decline in the cell's performance, i.e., the gradual electrolyte decomposition. In neutral pH (1 M Li_2SO_4), the cell based on $Ti_3C_2T_x$ showed a relatively stable capacitive behavior in a wide range of voltage from 0.5 to 1.3 V (Figure 5b).

A moderate increase in the current's response was noticed during the voltage extension. In the alkaline medium, the voltammograms show a typical EDL response up to 1 V (Figure 5c). Above 1 V, a rapid current rise related to the electrolyte decomposition was recorded. To find the reason behind the various working voltage, especially in acidic pH, the electrochemical performance of titanium carbide was evaluated separately for positive and negative electrodes, using a three-electrode symmetric system (Swagelok cell equipped with reference electrode). **Figure 6** presents the obtained results from the gradual expansion of the potential at scan rate of 5 mV s^{-1} in (a) acidic, (b) neutral, and (c) alkaline electrolytes. The positive $Ti_3C_2T_x$ electrode showed a considerably narrow working potential range (0.3–0.6 V

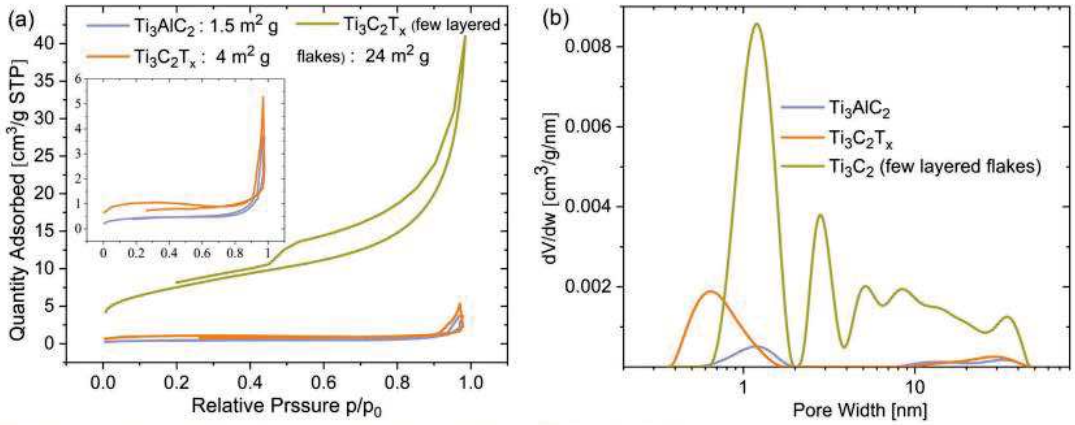

Figure 4. N_2 sorption isotherms at 77 K (a) and pore size distribution (b) of $Ti_3C_2T_x$ and Ti_3AlC_2.

© 2023 Wiley-VCH GmbH

ADVANCED SCIENCE NEWS
www.advancedsciencenews.com

NANO · MICRO small
www.small-journal.com

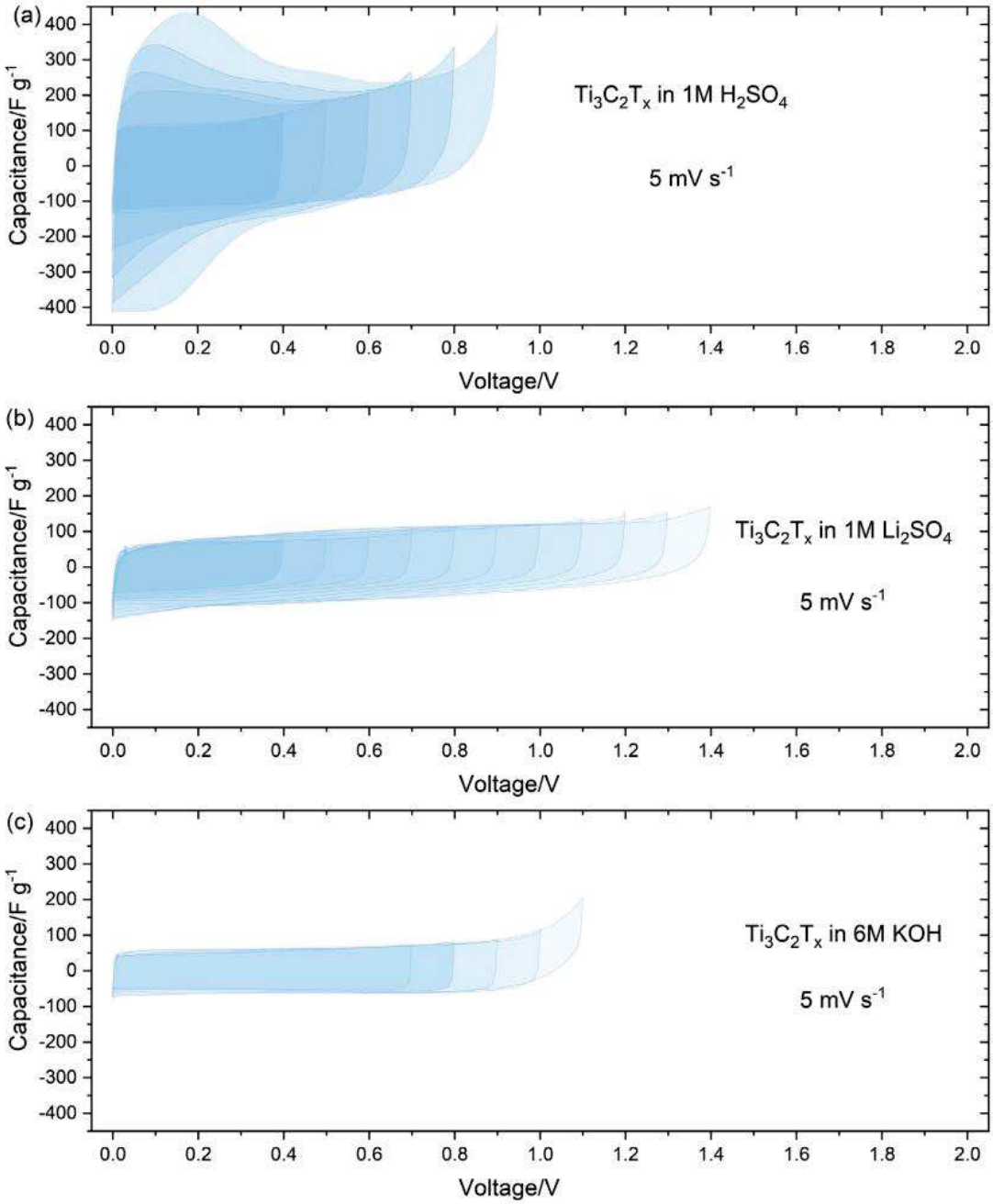

Figure 5. CV response of the assembled two-electrode Swagelok cell based on $Ti_3C_2T_x$ in 1 M H_2SO_4 (a), 1 M Li_2SO_4 (b), and 1 M KOH (c) at the scan rate of 5 mV s^{-1}. Au collectors.

© 2023 Wiley-VCH GmbH

ADVANCED SCIENCE NEWS
www.advancedsciencenews.com

NANO · MICRO small
www.small-journal.com

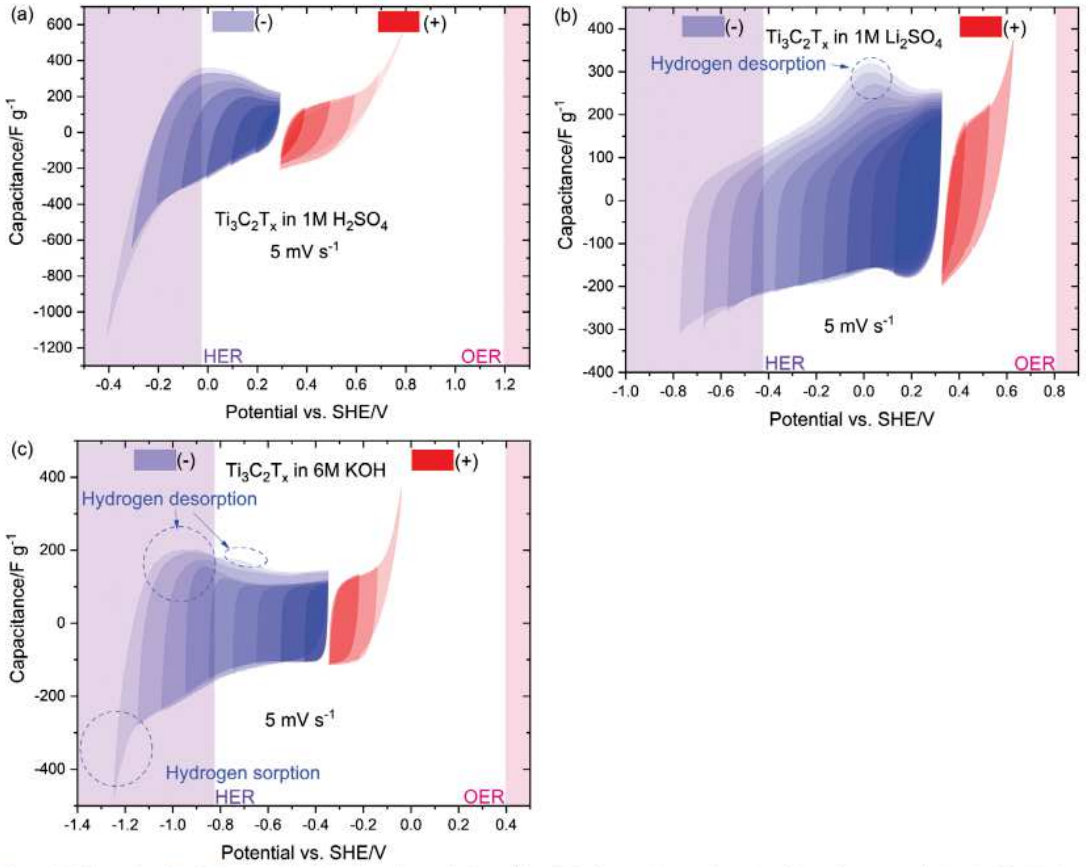

Figure 6. CV graphs of $Ti_3C_2T_x$, assembled in a three-electrode Swagelok cell, for the positive and negative electrode, separately. 1 M H_2SO_4 (a), 1 M Li_2SO_4 (b), and 6 M KOH (c) at the scan rate of 5 mV s^{-1}. Au collectors.

versus SHE) in the acidic medium (Figure 6a) which is far below the theoretical value of O_2 evolution (1.2 V). Oxidation process of the MXene electrode is clearly observed above 0.6 V versus SHE. Following the negative electrode, titanium carbide presented a capacitive behavior in the narrow range of potential related to sorption and desorption of solvated hydronium ions. However, when the potential range was gradually extended towards the negative values, the EDL response was accompanied by faradaic currents. Interestingly, a well reversible current response gradually increased even beyond the theoretical value of H_2 evolution (−0.03 V) that allowed the electrode to operate in a wider potential window.

To gain a better insight into the origin of the aforementioned hump, the capacitive and faradaic currents in the system were investigated in detail. For this purpose, the $Ti_3C_2T_x$ electrode was assembled in a three-electrode homemade cell with electrolyte excess that allows better diffusion. Figure S4 (Supporting Information) indicates the CV response of titanium carbide in 1 M H_2SO_4 during the negative polarization. The EDL behavior of $Ti_3C_2T_x$ was accompanied by the well visible faradaic currents during the gradual potential extension. It can be seen that response at 0.15 V versus SHE is located above the theoretical limit of H_2 evolution (−0.03 V vs SHE), hence, it should be related to the desorption of strongly adsorbed hydrogen. Below −0.2 V versus SHE, the rate of H_2 evolution has become intensified. Following such a current's rise, another oxidation hump close to the theoretical border appeared that is a clear sign that hydrogen is differently bonded to the electrode. It is well known that the hydrogen evolution can occur at underpotential and/or overpotential conditions,[32] and therefore, hydrogen desorption may occur at different potential values. Taking into' account the acidic medium (Figure S4, Supporting Information), the nascent hydrogen begins to appear even below the theoretical line, hence, hydrogen evolution reaction can be defined as follows:

$$H^+ + e^- \rightarrow H_{ads} \text{ (Volmerstep)} \quad (1)$$

$$2H_{ads} \rightarrow H_2 \text{ (Tafelstep)} \quad (2)$$

 © 2023 Wiley-VCH GmbH

ADVANCED SCIENCE NEWS
www.advancedsciencenews.com

NANO · MICRO small
www.small-journal.com

$$H^+ + H_{ads} + e^- \rightarrow H_2 \text{ (Heyrovskystep)} \quad (3)$$

Once the adsorption energy for hydrogen is lower than the energy needed for H release, and Tafel or Heyrovsky steps have a low activation barrier, a number of adsorbed hydrogen can combine into H_2. Otherwise, the adsorbed hydrogen can diffuse to the inner space between the titanium carbide layers and becoming trapped in sites with higher adsorption energy (chemisorption). Our previous studies on hydrogen storage into activated microporous carbon indicate the correlation of sorption/desorption potentials with the different strength of interactions.[32] While H physisorption may occur more easily, i.e., at less negative potentials, Kubas interactions or chemisorption happen at more negative potentials (more energy needed). Therefore, it can be said that the peak at −0.03 V versus SHE belongs to desorption of H_2 molecules, and the peak at 0.17 V versus SHE is assigned to desorption of H_{ads}. Our experimental results link the nature of interactions between the hydrogen and $Ti_3C_2T_x$ surface obtained from molecular calculations, i.e., physisorption and Kubas interactions which contribute equally (3.4 wt%).[15] Considering the fact that both ill-defined peaks are well separated it proves that two types of H sorption sites exist. Hence, anodic humps at −0.03 V and 0.17 V may be designated to release H_2 molecules that were adsorbed by physisorption and Kubas bonding, respectively.

In 1 M Li_2SO_4 (Figure 6b), $Ti_3C_2T_x$ showed an EDL performance in a wide voltage range (to 1.3 V), mainly due to the stable performance of the electrode in negative potential. Nevertheless, the positive polarization of the $Ti_3C_2T_x$ resulted in the same charge response as that of titanium carbide in the acidic electrolyte. Comparing the charge of the negative and positive electrodes, there is a significant imbalance between both electrodes. Below −0.8 V versus SHE, the capacitive response of the electrode was accompanied by parasitic currents (H_2 bubbling), and therefore, reaching a stable current by further expansion was not possible. The oxidation peak at 0.1 V versus SHE originates from desorption of the hydrogen that was more strongly adsorbed, probably chemisorbed. Considering the CV response of $Ti_3C_2T_x$ in the alkaline medium (Figure 6c), a more rectangular CV profile was obtained in comparison with that in acidic and neutral media. Especially, above the theoretical water reduction limit (from −0.3 to −0.8 V versus SHE range), titanium carbide showed almost a pure EDL response. Lower than this value (−0.83 V), the faradaic currents caused by hydrogen adsorption/desorption were observed. The mild hump at −0.7 V versus SHE is assigned to the moderately stored hydrogen. Figure S5 (Supporting Information) presents the EIS spectra recorded after each 200 mV of potential expansion during the negative CV polarization. After the first step of potential expansion, in acidic and neutral media, the cell shows a charge transfer resistance (semicircle) and Warburg diffusion response (vertical line). Further polarization towards negative potential results in the disappearance of the semicircles and a lower diffusion resistance. In alkaline electrolyte, the EIS spectra consisted of a vertical Warburg line, and almost no charge transfer was detected during the step-wise expansion of potential. Generally, in the acidic medium titanium carbide showed a considerable capacity in a narrow range of voltage which was mainly due to the reversible redox reactions of hydrogen. In the neutral medium, on the other hand, the cell operated in a wider voltage window with a mediocre capacitance.

To exploit both advantages, the influence of electrolyte pH on the CV response of $Ti_3C_2T_x$ in 1 M Li_2SO_4 (pH adjusted to 2 and 3) and 1 M $BeSO_4$ (pH 2) was investigated. **Figure 7** indicates the obtained voltammograms from the three-electrode symmetric cell experiments. Separate polarization of the electrodes indicates the presence of a redox peak in pH 2 (Figure 7a) and in pH 3 (Figure 7b) that are comparable to the observed hump in 1 M Li_2SO_4 (Figure 6b). The acidic pH of the electrolyte drives the negative electrode to perform in a relatively narrow potential range (0.9 V in 1 M Li_2SO_4 with pH 2 and 3 versus 1.1 V in 1 M Li_2SO_4). In 1 M $BeSO_4$, the CV profile of $Ti_3C_2T_x$ negatively polarized showed a redox peak below the theoretical line (Figure 7c). Further decrease of the cut-off potential from −0.35 to −0.45 V versus SHE led to a sudden increase of the hydrogen evolution. The first and the second peaks during the anodic scan can be assigned to desorption of weakly and tightly bonded hydrogen. As it was expected, there is an imbalance between the capacity of the negative and positive electrodes that can affect the working voltage of the cell. Such inequality is due to the different storage mechanism of both electrodes, especially oxidative degradation of positive one.

Figure 7d compares the voltammogram of $Ti_3C_2T_x$ (–) in acidic and neutral electrolytes. Decreasing the pH of the medium improves the rate of hydrogen adsorption/desorption, i.e., the capacity of the electrode but in the narrow potential range. In the case of $BeSO_4$ electrolyte, the higher EDL capacity is observed than for Li_2SO_4 with the same pH, it can be explained by the smaller size of Be^{2+} ionic radii (0.031 nm) than strongly solvated Li^+ (0.060 nm).

In addition, we tried to study the hydrogen storage into the titanium carbide by the galvanostatic charge–discharge test (Figure S6, Supporting Information). For this purpose, the homemade cell was assembled with 1 M H_2SO_4, 1 M Li_2SO_4, and 6 M KOH using $Ti_3C_2T_x$ as the working electrode. At first, the electrodes were conditioned within the respective stable potential, using the cyclic voltammetry technique. After relaxation for 1 h under OCV, the electrodes were negatively polarized to the lowest potential for the hydrogen sorption and were kept at that point for 12 h to adsorb hydrogen at the surface (current density of -0.5 A g^{-1}). After that, a current density of $+0.025$ A g^{-1} was applied and electrodes were charged up to the highest potential. It is interesting to observe the OCV values just after the negative polarization. In the case of neutral and alkaline medium, the potential of electrode has negative values −0.6 V versus SHE and −0.9 V versus SHE, respectively. Such low potential value shows that in the electrode there is electrosorbed hydrogen. However, in the case of acidic medium, the potential of electrode rapidly reached the positive values. From our experience gained with the hydrogen sorption in activated carbon,[13,32] it clearly shows that H-MXene interactions are more weak in acidic medium than in alkaline and neutral electrolytes. The anodic charge responses (Figure S6, Supporting Information) reflect hydrogen desorption and they are in agreement with the cyclic voltammograms (Figure 6). From the previously reported studies by Compton and co-workers[33] carried out on TiC particles, there is no faradaic response due to the oxidation of titanium carbide in acidic and neutral media within this potential range, hence, such a response can be assigned to the electrodesorption of hydrogen from Ti_3C_2.

© 2023 Wiley-VCH GmbH

ADVANCED SCIENCE NEWS
www.advancedsciencenews.com

NANO · MICRO small
www.small-journal.com

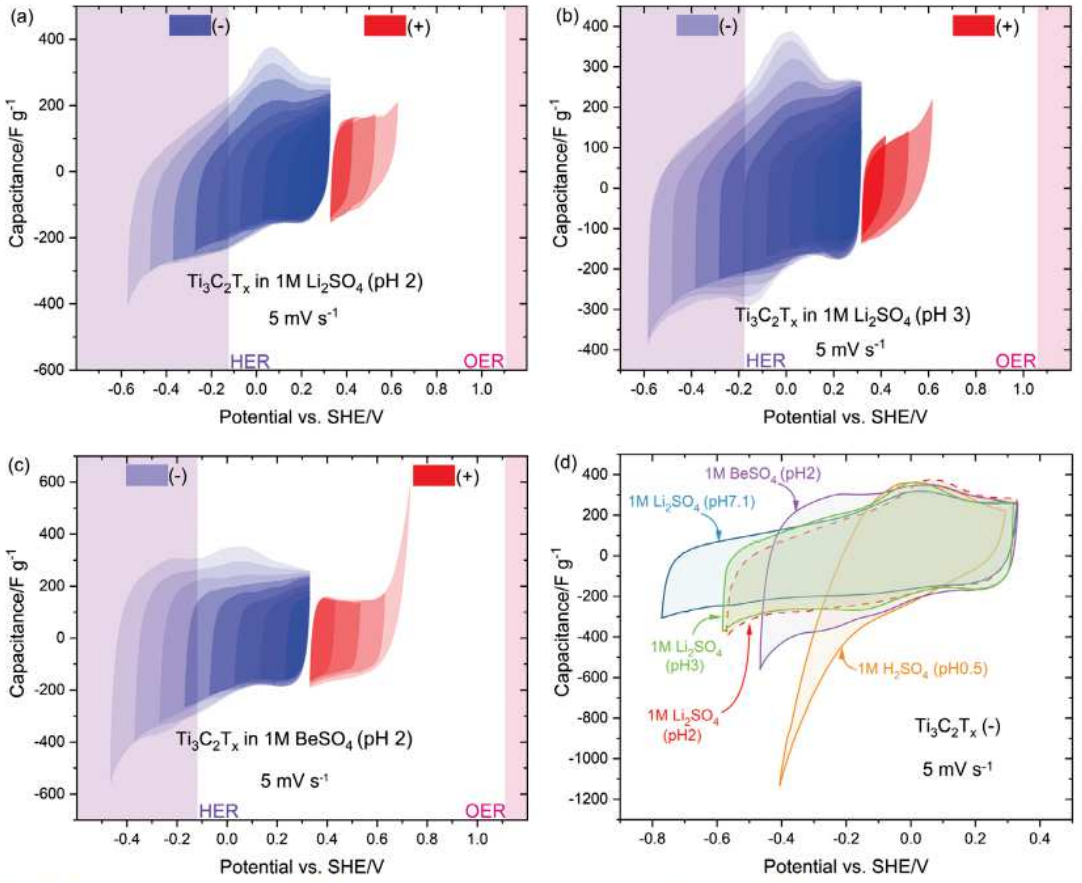

Figure 7. Electrochemical performance of $Ti_3C_2T_x$ in a three-electrode Swagelok cell, including CV graphs of $Ti_3C_2T_x$ as the negative and positive electrode in 1 M Li_2SO_4 with: a) pH of 2; b) pH of 3; and c) 1 M $BeSO_4$. d) Comparison between the electrochemical performance of the negative $Ti_3C_2T_x$ in acidic and neutral media. Au collectors.

Surely, the amount of hydrogen stored could be improved with the more porous MXene samples and the higher interlayer distance.

We have also performed some EC accelerated aging, so called floating tests. The symmetric EC system was kept at the maximum voltage, i.e., 0.7 V in 1 M H_2SO_4 and 1.4 V in 1 M Li_2SO_4. At that time, all parasitic reactions could occur during these harsh conditions and some oxidation of both electrodes was observed. Oxygen content (wt%) of electrode (+) increased from 5.3% to 9.3% in 1 M Li_2SO_4 and to 12.6% in 1 M H_2SO_4. For electrode (–), the oxygen content increased to 10.4% in 1 M Li_2SO_4 and to 9.3% in 1 M H_2SO_4. Hence, some moderate passivation of electrodes cannot be excluded.

The effect of current collectors has also been investigated. Gold current collectors were used for the comparative electrode characterization. It was proven that the titanium-based materials may show a great ability to store hydrogen.[34–36] Figure S7 (Supporting Information) compares the CV response of the titanium carbide in the negative potential range, assembled in a three-electrode cell using titanium or gold current collectors. In 1 M H_2SO_4, the capacity of $Ti_3C_2T_x$ shows a considerable improvement (almost two times higher) once gold current collectors were replaced by Ti ones. Such capacity increase even resulted in the appearance of the two specific humps instead of one peak, similar to the observed in Figure S4 (Supporting Information). In our investigation, we found that the current density shows a considerable increase as the potential range of study was expanded toward the negative values. In 1 M Li_2SO_4, the assembled cell based on Ti current collectors shows a relatively same capacity behavior but in a wider potential window. In basic medium, the obtained CV profiles are completely the same, and no meaningful difference was observed. In general, it is better to avoid using Ti current collectors while evaluating the reliable performance of MXenes in acidic medium.

© 2023 Wiley-VCH GmbH

ADVANCED SCIENCE NEWS
www.advancedsciencenews.com

NANO · MICRO small
www.small-journal.com

Comparing the performance of $Ti_3C_2T_x$ in a wide potential range indicates that symmetric cells based on titanium carbide fail to meet the demand for wide voltage range ECs. Such drawback is mainly due to the following reasons: i) the restricted working potential of $Ti_3C_2T_x$ in negative potential ranges; ii) different storage mechanisms of titanium carbide in the negative (capacitive and faradaic contribution) and positive (oxidative degradation) ranges that lead to a severe charge imbalance. Another strategy such as cell modification might be a better approach to improving the performance of $Ti_3C_2T_x$-based ECs. It is well known that the porous carbons show a stable electrochemical performance in a wide range of potentials. Figure S8 (Supporting Information) presents the electrochemical behavior of BP2000 in a symmetric cell and as the negative and positive electrodes. During the negative polarization, molecular hydrogen will be evolved (Tafel step). However, no H desorption was detected during the oxidation. Compared to the positive $Ti_3C_2T_x$, BP2000 can offer a suitable capacitive response in a wide potential range. Thus, a series of asymmetric cells was assembled based on $Ti_3C_2T_x$ and BP as the negative and positive electrodes, respectively. **Figure** 8a–c displays the recorded CV profiles from two-electrode cell experiments. In acidic and basic media, asymmetric cells were able to perform up to 1.3 and 1.4 V, respectively. These values are higher than the working voltage of symmetric $Ti_3C_2T_x$ cells in 1 M H_2SO_4 (0.9 V) and 6 M KOH (1 V). A more significant improvement was detected in case of the asymmetric cell in the neutral medium, where a stable capacitive behavior up to 2 V was recorded. Figure 8d–f shows the CV response of titanium carbide and BP in various media. As it can be seen, the major improvement is related to the performance of the positive electrode (BP2000) that operates in a considerably wider potential window in comparison with the positively polarized $Ti_3C_2T_x$ (see Figure 6). In a neutral medium, BP2000 operates even beyond the theoretical OER border, and it is 4 times wider than the recorded working potential of the positive $Ti_3C_2T_x$ electrode (0.8 V vs 0.2 V). In addition to the expansion of working potential, there is a significant increase in the charge storage of positive electrode. As it was mentioned, positively polarized titanium carbide stores charge mainly through non-faradaic mechanism. While low surface area MXenes (4 $m^2\ g^{-1}$) fail to store a substantial part of charge, BP2000 with a well-developed micro/mesoporous surface area (≈2000 $m^2\ g^{-1}$) can supply a high capacitance. When there is an imbalance between charges of electrodes, the capacitance of a cell will be restricted mainly by the performance of the electrode with the lower capacity. Therefore, charge balance between the negative and positive electrodes can be taken as the other reason behind voltage expansion of asymmetric ECs.

From the galvanostatic charge/discharge profile, the asymmetric cell based on $Ti_3C_2T_x$ reached a coulombic and energy efficiency of 100% and 83%, respectively (**Figure** 9). The typical concave shape of the discharge curve shows that energetic efficiency of EC is lower (83%) during whole galvanostatic tests.

To verify the stability of the cell's performance during long cycling, the assembled asymmetric cell was subjected to continuous charge-discharge cycles at 2 V till the capacitance of the cell was decreased to 80% of its initial value (international standard limit). The cell was able to operate up to 22 000 galvanostatic charge-discharge cycles at 1 A g^{-1} which is quite promising in comparison with the previously reported data. In addition, an energy density of 11.4 Wh kg^{-1} at a power density of 501 W kg^{-1} and a current density of 1 A g^{-1} was calculated.

3. Conclusions

MXenes are a new family of 2D materials applied for various energy storage systems. Yet, some drawbacks have to be overcome to fully exploit them. Generally, they are not adapted as a positive electrode because they are easily oxidized and decomposed at high potentials. On the other hand, they are attractive candidates for a negative side. $Ti_3C_2T_x$ MXene was selected as a promising hydrogen storage material that can be interesting for energy applications. However, in the literature there are no experimental investigations regarding the mechanism or the nature of interactions that are involved. This study aims to provide a better understanding of the energy storage of MXene in EC. For this purpose, the performance of titanium carbide, as the main studied member of MXene family, was evaluated using full cells in different aqueous media and pH values. It has been noticed that hydrogen adsorbs at the surface/bulk of MXene layers with different bonding strength. As tight bonding may occur depending on pH, type of electrolyte and overpotentials, it is possible to differentiate between the contributions of the weak and strong interactions in the total hydrogen storage of MXenes. The two designated humps can be assigned to desorption of H_2 by physisorption and Kubas interactions. Following the obtained information, we addressed the problem with the narrow working voltage of symmetric $Ti_3C_2T_x$-based ECs due to a lack of the stability for positive electrode. It was found that a combination of capacitive and faradaic currents is responsible for the energy storage of the titanium carbide during the negative polarization. However, in the positive range, a high disproportion with the negligible capacitive charge is observed. These factors are the two main reasons behind the narrow working voltage of MXene-based ECs. Employing carbon materials as the positive electrode, the asymmetric cell based on MXene and BP2000 was able to operate to 1.3, 2, and 1.4 V in acid, neutral and basic medium, respectively. These values are substantially higher than the obtained values from the symmetric $Ti_3C_2T_x$-based ECs. The asymmetric cell in 1 M Li_2SO_4 was able to reach the performance for continuous 22 000 charge–discharge cycles that is quite promising in comparison with the previously reported values.

4. Experimental Section

Material Preparation: $Ti_3C_2T_x$ was synthesized through the exfoliation of the MAX phase (Ti_3AlC_2), using a combination of hydrochloric acid (HCl) and lithium fluoride (LiF).[37,38] Briefly, 2 g of LiF was added into a polypropylene beaker containing 40 ml of 9 M HCl, and the mixture was vigorously stirred (450 rpm) for 15 min till the complete dissolution of the Li salt. Later, the beaker was transferred into an ice-water bath, and it was cooled down to 10 °C. Afterward, 2 g of Ti_3AlC_2 (≤40 µm particle size, Sigma-Aldrich Co.) gradually was added (in 20 min) to the beaker. Subsequently, the reaction was heated up to 50 °C, and it was maintained at this temperature for 24 h before becoming cooled down to room temperature. The resulting sample was poured into propylene tubes, and it was subjected to one step of centrifuge at 3500 rpm for 5 min before decanting the HCl residue away. The remaining $Ti_3C_2T_x$ precipitate was dispersed in

 © 2023 Wiley-VCH GmbH

ADVANCED SCIENCE NEWS
www.advancedsciencenews.com

NANO · MICRO small
www.small-journal.com

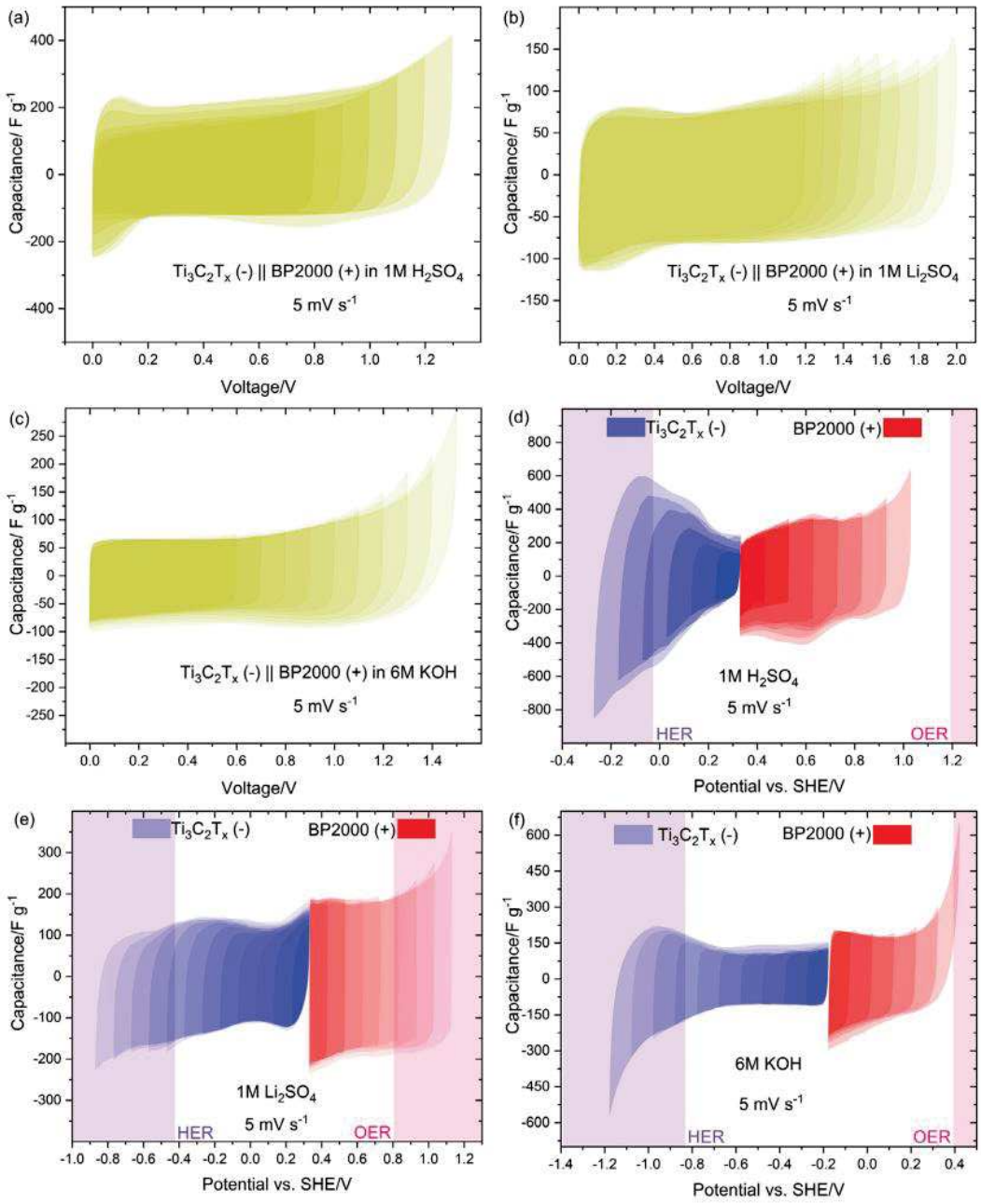

Figure 8. CV curves of the asymmetric three-electrode Swagelok cell based on (−)$Ti_3C_2T_x$ and (+)BP2000 electrodes: a) 1 M H_2SO_4; b) 1 M Li_2SO_4; c) 6 M KOH. CV profiles of the negative $Ti_3C_2T_x$ and positive BP2000 electrodes: d) 1 M H_2SO_4, e) 1 M Li_2SO_4, f) 6 M KOH. Ti current collectors.

© 2023 Wiley-VCH GmbH

ADVANCED SCIENCE NEWS
www.advancedsciencenews.com

NANO · MICRO small
www.small-journal.com

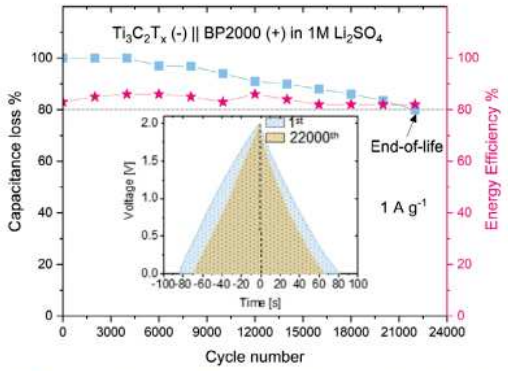

Figure 9. Cyclic performance of the asymmetric Swagelok cell based on $Ti_3C_2T_x$ and BP2000 as the negative and positive electrodes in 1 M Li_2SO_4 at the current density of 1 A g^{-1}.

DIW, and it was centrifuged for another 5 min at 3500 rpm, and the acidic waste was separated at the end of the process. This stage was repeated six times till the pH of the supernatant reached 5.8. Eventually, the sample was redispersed in 1 l of DIW and was vacuum filtered before becoming dried at 50 °C for 24 h.

Physiochemical Characterization: XRD analysis was used to examine the chemical structure and interlayer spacing of the MAX phase and $Ti_3C_2T_x$ sample. BRUKER D8 Advanced, equipped with a Johansson monochromator using Cu $K\alpha$ radiation (Cu $K\alpha$, $\lambda = 1.5406$ Å) was employed for the XRD study. The quantitative analysis of surfaces was carried out using X-ray photoelectron spectroscopy (XPS). The analyses were carried out in a PHI VersaProbeII Scanning XPS system using monochromatic Al $K\alpha$ (1486.6 eV) X-rays focused to a 100 µm spot and scanned over the area of 400 µm × 400 µm. The photoelectron take-off angle was 45° and the pass energy in the analyzer was set to 117.50 eV (0.5 eV step) for survey scans and 46.95 eV (0.1 eV step) to obtain high energy resolution spectra for the C 1s, O 1s, Ti 2p, Cl 2p, Al 2p, F 1s, and Si 2p regions. A dual beam charge compensation with 7 eV Ar^+ ions and 1 eV electrons were used to maintain a constant sample surface potential regardless of the sample conductivity. All XPS spectra were charge referenced to the unfunctionalized, saturated carbon (C–C) C 1s peak at 285.0 eV. The operating pressure in the analytical chamber was less than 5×10^{-9} mbar. Deconvolution of the spectra was carried out using PHI MultiPak software (v.9.9.3). Spectrum background was subtracted using the Shirley method. The morphology of the samples was studied using Scanning Electron Microscope SEM Jeol 7001TTLS. Brunauer–Emmett–Teller (BET) analysis was carried out to examine the surface area and pore size distribution of the materials. ASAP 2460 analyzer (Micromeritics, US) was used in this case. The surface area was determined using the Brunauer–Emmett–Teller equation in the relative pressure range of 0.01–0.05.

Electrode Preparation and Characterization: Electrodes were prepared using 90% of active material, 5% of polytetrafluoroethylene (60 wt% aqueous dispersion), and 5% of conductive additive (C-NERGY Super C65, Imerys). The components were transferred into a mortar and mixed together using isopropanol as the solvent. After the formation of a homogenized dough-like paste, samples were rolled by a calendaring machine into a sheet with ≈150 µm thickness. Subsequently, disc-like electrodes with a diameter of 8 mm were cut before drying at 60 °C overnight in a dryer. The mass of the electrodes in the case of assembled symmetric and asymmetric cells was around 6–7 mg and 3 mg, respectively. Whatman glass microfiber membrane with a diameter of 12 mm was cut to use as the separator. Two-electrode Swagelok cells were used for determining the electrochemical performance of symmetric and asymmetric $Ti_3C_2T_x$-based ECs. The two-electrode Swagelok cells, equipped with a reference electrode, were employed to study the capacitive behavior of titanium carbide as the negative and positive electrodes. For this purpose, Hg/Hg_2SO_4 (in 1 M H_2SO_4) and Hg/HgO (in 6 M KOH) reference electrodes were used for investigations in acidic/neutral and basic media, respectively. 1 M H_2SO_4, 1 M $BeSO_4$, 1 M Li_2SO_4 with different pH, and 6 M KOH were served as the electrolyte. A three-electrode homemade cell with electrolyte excess was used to investigate the hydrogen adsorption/desorption mechanism of $Ti_3C_2T_x$. In this case, a platinum mesh served as the counter electrode. Gold current collectors were employed in all experiments, except for the cyclability analysis of the asymmetric cell in 1 M Li_2SO_4. To see the influence of current collectors on the charge storage of titanium carbide, a two-electrode cell with a reference electrode was assembled, and titanium current collectors were used in this study. A computer-controlled multichannel potentiostat/galvanostat (VMP3, Biologic, France) was used to conduct and control all measurements.

Supporting Information

Supporting Information is available from the Wiley Online Library or from the author.

Acknowledgements

The authors would like to acknowledge the National Science Centre, Poland, for the financial support in the framework of the project 2022/45/N/ST5/02275 and partially from 0911/SBAD/2301 project.

Conflict of Interest

The authors declare no conflict of interest.

Data Availability Statement

The data that support the findings of this study are available from the corresponding author upon reasonable request.

Keywords

aqueous electrolyte, electrochemical capacitor, hydrogen storage, overpotential, $Ti_3C_2T_x$ MXene, wide operating voltage

Received: August 22, 2023
Revised: November 13, 2023
Published online:

[1] L. Demarconnay, E. Raymundo-Piñero, F. Béguin, *Electrochem. Commun.* **2010**, *12*, 1275.
[2] M. F. Koudahi, E. Frackowiak, *Energy Storage Mater.* **2022**, *49*, 255.
[3] E. Frackowiak, M. Foroutan Koudahi, M. Tobis, *Small* **2021**, *17*, 2006821.
[4] Y. Zheng, K. Chen, K. Jiang, F. Zhang, G. Zhu, H. Xu, *J. Energy Storage* **2022**, *56*, 105995.
[5] S. Isikli, M. Lecea, M. Ribagorda, M. C. Carreño, R. Díaz, *Carbon* **2010**, *66*, 654.
[6] A. Eftekhari, B. Fang, *Int. J. Hydrogen Energy* **2017**, *42*, 25143.
[7] S. Liu, J. Liu, X. Liu, J. Shang, L. Xu, R. Yu, J. Shui, *Nat. Nanotechnol.* **2021**, *16*, 31.
[8] M. R. Lukatskaya, S. Kota, Z. Lin, M.-Q. Zhao, N. Shpigel, M. D. Levi, J. Halim, P.-L. Taberna, M. W. Barsoum, P. Simon, Y. Gogotsi, *Nat. Energy* **2017**, *2*, 17105.

 © 2023 Wiley-VCH GmbH

[9] S. Wook Han, G. Cha, Y. Park, S. C. Hong, *Sci. Rep.* **2017**, *7*, 7152.
[10] T. K. A. Hoang, D. M. Antonelli, *Adv. Mater.* **2009**, *21*, 1787.
[11] N. Kostoglou, V. Tzitzios, A. G. Kontos, K. Giannakopoulos, C. Tampaxis, A. Papavasiliou, G. Charalambopoulou, T. Steriotis, Y. Li, K. Liao, K. Polychronopoulou, C. Mitterer, C. Rebholz, *Int. J. Hydrogen Energy* **2015**, *40*, 6844.
[12] L. Morris, M. L. Trudeau, D. Reed, D. Book, D. M. Antonelli, *Phys. Chem. Chem. Phys.* **2015**, *17*, 9480.
[13] F. Béguin, M. Friebe, K. Jurewicz, C. Vix-Guterl, J. Dentzer, E. Frackowiak, *Carbon* **2006**, *44*, 2392.
[14] K. Raju, S. Rajendran, T. K. A. Hoang, D. Durgalakshmi, J. Qin, D. E. Diaz-Droguett, F. Gracia, M. A. Gracia-Pinilla, *J. Power Sources* **2020**, *466*, 228305.
[15] Q. Hu, D. Sun, Q. Wu, H. Wang, L. Wang, B. Liu, A. Zhou, J. He, *J. Phys. Chem. A* **2013**, *117*, 14253.
[16] X. Li, Z. Huang, C. E. Shuck, G. Liang, Y. Gogotsi, *Nat. Rev. Chem.* **2022**, *6*, 389.
[17] J. Halim, S. Kota, M. R. Lukatskaya, M. Naguib, M.-Q. Zhao, E. J. Moon, J. Pitock, J. Nanda, S. J. May, Y. Gogotsi, M. W. Barsoum, *Adv. Funct. Mater.* **2016**, *26*, 3118.
[18] Y. Wang, X. Wang, X. Li, Y. Bai, H. Xiao, Y. Liu, R. Liu, G. Yuan, *Adv. Funct. Mater.* **2019**, *29*, 1900326.
[19] P. Simon, *ACS Nano* **2017**, *11*, 2393.
[20] R. Ibragimova, P. Erhart, P. Rinke, H.-P. Komsa, *J. Phys. Chem. Lett.* **2021**, *12*, 2377.
[21] P. Kumar, S. Singh, S. A. R. Hashmi, K.-H. Kim, *Nano Energy* **2021**, *85*, 105989.
[22] Y. Zhou, K. Maleski, B. Anasori, J. O. Thostenson, Y. Pang, Y. Feng, K. Zeng, C. B. Parker, S. Zauscher, Y. Gogotsi, J. T. Glass, C. Cao, *ACS Nano* **2020**, *14*, 3576.
[23] Z. Hu, Y. Xie, D. Yu, Q. Liu, L. Zhou, K. Zhang, P. Li, F. Hu, L. Li, S. Chou, S. Peng, *ACS Nano* **2021**, *15*, 8407.
[24] M. Naguib, M. Kurtoglu, V. Presser, J. Lu, J. Niu, M. Heon, L. Hultman, Y. Gogotsi, M. W. Barsoum, *Adv. Mater.* **2011**, *23*, 4248.
[25] J. Luo, X. Tao, J. Zhang, Y. Xia, H. Huang, L. Zhang, Y. Gan, C. Liang, W. Zhang, *ACS Nano* **2016**, *10*, 2491.
[26] A. D. Wagner, A. V. Naumkin, A. Kraut-Vass, J. W. Allison, C. J. Powell, J. R. J. Rumble, *NIST Standard Reference Database (SRD 20)*, **2003**, http://doi.org/10.18434/T4T88K
[27] M. C. Biesinger, L. W. M. Lau, A. R. Gerson, R. S. C. Smart, *Appl. Surface Sci.* **2010**, *257*, 887.
[28] N. C. Saha, H. G. Tompkins, *J. Appl. Phys.* **1992**, *72*, 3072.
[29] C. D. Wagner, D. E. Passoja, H. F. Hillery, T. G. Kinisky, H. A. Six, W. T. Jansen, J. A. Taylor, *J. Vac. Sci. Technol.* **1982**, *21*, 933.
[30] G. Beamson, D., Briggs, *J. Chem. Educ.* **1993**, *70*, 25.
[31] X. Wang, W. Chen, Y. Liao, Q. Xiang, Y. Li, T. Wen, Z. Zhong, *J. Mater. Sci.* **2021**, *56*, 2486.
[32] K. Jurewicz, E. Frackowiak, F. Béguin, *Appl. Phys. A* **2004**, *78*, 981.
[33] P. Nayak, R.-C. Xie, R. G. Palgrave, R. G. Compton, *Chem. Electro. Chem.* **2021**, *8*, 911.
[34] V. Stavila, R. Bhakta, T. M. Alam, E. H. Majzoub, M. Allendorf, *ACS Nano* **2012**, *6*, 9807.
[35] U. Ulmer, M. Dieterich, A. Pohl, R. Dittmeyer, M. Linder, M. Fichtner, *Int. J. Hydrogen Energy* **2017**, *42*, 20103.
[36] P. Millenbach, M. Givon, *J. Less-Common Metals* **1982**, *87*, 179.
[37] C. M. Subramaniyam, M.-A. Kang, J. Li, A. Vahidmohammadi, M. M. Hamedi, *Energy Adv.* **2022**, *1*, 999.
[38] Y. Su, B. Liu, Q. Zhang, J. Peng, C. Wei, S. Li, W. Li, Z. Xue, X. Yang, J. Sun, *Adv. Funct. Mater.* **2022**, *32*, 2204306.

 © 2023 Wiley-VCH GmbH

6. Article 4

Title: ***Charge storage and operando electrochemical dilatometry of MXene electrodes in ionic liquids***

Authors: Masoud Foroutan Koudahi, Andres Camilo Parejo Tovar, François Béguin, Elżbieta Frąckowiak*

Journal: submitted

DOI: -

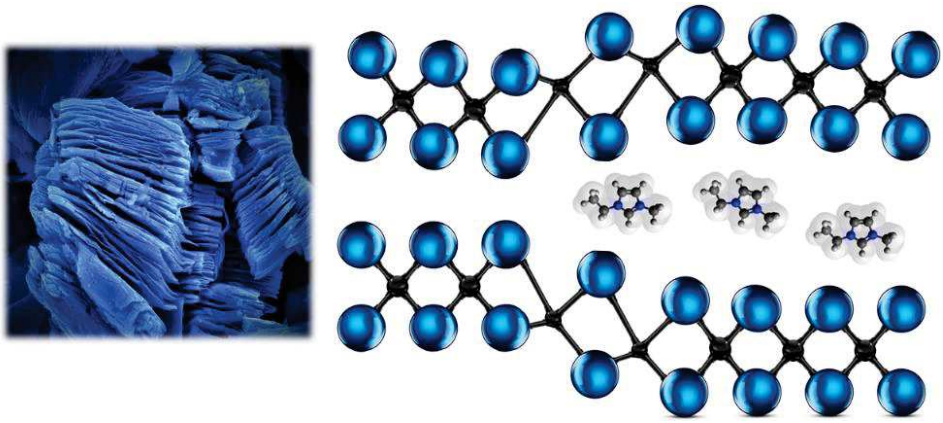

Motivation

ILs are one of promising class of electrolytes due to their high electrochemical stability for energy storage applications. MXenes show a rich charge storage behavior in aqueous-ECs, although their working potential is severely limited. Design of IL-based ECs is an important step in extending the applications of MXenes in energy storage. For this purpose, it is vital to understand the fundamentals of interactions at the electrode/electrolyte interface in these systems. A comprehensive study was carried out, where titanium carbides and molybdenum titanium carbides with different structural and chemical properties were prepared.

Physicochemical characterizations such as XRD and SEM revealed the difference between the interlayer spacing of the samples. XPS analysis exhibited the possibility of controlling the surface functional groups, which play a significant role in the energy storage of MXenes. Ti carbides presented a well delaminated structure, while in the case of Mo/Ti carbide a relatively dense structure after etching was observed.

Typical electrochemical characterization but also *operando* electrochemical dilatometry measurements, were carried out to explain the importance of preparation method on key properties such as interlayer spacing and surface functionalities, and subsequently, their influence on the energy storage of MXenes-based ECs. Ionic liquids with different size of cation and anion served as electrolytes. CV response presented a combination of faradaic and capacitive current that are involved in the charge storage of titanium carbides during the negative polarization. Dilatometry investigations provided important information in linking the growing capacitive response of negatively polarized titanium carbides with its volumetric expansion. In contrast, Mo/Ti carbides exhibit volumetric expansion only during the positive polarization. Faradaic current could be interpreted by the hydrogen bonding, hydroxide surface groups at MXene can share their hydrogen with ionic liquids that can play the role of hydrogen acceptor.

For the first time, charge/discharge phenomena of Mo/Ti carbides have been studied in ionic liquids using *operando* electrochemical dilatometry.

7. Article that are not included in this thesis

Title: ***Reline deep eutectic solvent as a green electrolyte for electrochemical energy storage applications†***

Authors: Sara Azmi, Masoud Foroutan Koudahi, Elzbieta Frackowiak*

Journal: Energy & Environmental Science

DOI: https://doi.org/10.1039/D1EE02920G

Motivation

Deep eutectic solvents (DES) have been attracted much attention in the recent years due to their green and environmental friendly nature. In addition, they have an excellent anti-corrosion properties, resulting in the elongation of the working life of the current collectors in an electrochemical cell. Similar to organic electrolytes, solvent-free media can provide a stable working voltage for ECs, although the cell assembly requires inert atmosphere, which is expensive. Realizing DES-based ECs in ambient conditions results in a considerable decrease at the cost and the time of cell production. The flexibility of cell handling at the air allows us to have a better control over important characteristics of DES such as its high viscosity. In addition, the nature of interactions between DES molecules and the surface of porous electrodes is complex. Therefore, reline DES electrolyte with different viscosity and electrode materials with various porous texture were selected to gain a comprehensive knowledge about the mechanism of charge storage in these systems. It was found that a stable EDL response in a wide voltage range (up to 2.2V), with a high energy efficiency, and a long life span can be reached. Improving the rate of ionic diffusion was crucial, in particular from the bulk electrolyte to the inner structure of the electrode. Addition of small amount of water up to the certain value improved the charge storage of the cell without degrading key metrics such as cycle life or the self-discharge.

List of figures

Figures

Scientific accomplishments

8. Publications

1) *Electrochemical Capacitor Performance of Nanotextured Carbon/Transition Metal Dichalcogenides Composites*
   E. Frąckowiak*, **M. Foroutan Koudahi**, M. Tobis
   Small, 17, 2021, 2006821 **(IF: 13.3)**
2) *Reline deep eutectic solvent as a green electrolyte for electrochemical energy storage*
   Applications (article not included in the dissertation)
   S. Azmi, **M. Foroutan Koudahi**, E. Frackowiak*
   Energy and Environmental Science, 15, 2022, 1156-1171 **(IF: 39.714)**
3) *Fast response supercapacitor based on carbon-VS2 electrodes with a wide operating*

voltage range

M. Foroutan Koudahi, E. Frąckowiak*

Energy Storage Materials, 49, 2022, 255-267 **(IF: 20.4)**

4) *$Ti_3C_2T_x$ MXene as Intriguing Material for Electrochemical Capacitor*

M. Foroutan Koudahi, E. Frąckowiak*

Small, 2023, 2307165 **(IF: 13.3)**

5) *Charge storage and operando electrochemical dilatometry of MXene electrodes in ionic liquids*

M. Foroutan Koudahi, Andres Camilo Parejo Tovar, François Béguin, Elżbieta Frąckowiak*

Submitted

Total Impact Factor: 86,714

9. Reports

1) *Preparation and characterization of novel 2D MXenes material / Masoud Foroutan Koudahi (WTCH) // r4109_2023*

M. Foroutan Koudahi, E. Frąckowiak

10. Scientific conferences

1) *Composites Based on Three-dimensional Graphene and Transition Metal Dichalcogenides as the Electrode Materials in Supercapacitors*

M. Foroutan Koudahi, E. Frąckowiak

Poster, August 31-September 04, 2020, 71st Annual Meeting of the International Society of Electrochemistry (ISE)

Belgrade, Serbia (on-line)

2) *Carbon/Dichalcogenide Composites as Electrodes for Electrochemical Capacitors*
   M. Tobis, M. Foroutan Koudahi, **E. Frąckowiak**
   Oral, October 4-9, 2020, Pacific Rim Meeting on Electrochemical and Solid State Science
   Hawaii, USA (on-line)
3) *Carbon/ReS_2 Composites as an Attractive Electrode Materials in Electrochemical Capacitors*
   M. Tobis, M. Foroutan Koudahi, E. Frąckowiak
   Poster, August 18-20, 2021, American Association for Advances in Functional Materials
   Los Angeles, USA (on-line)
4) *Nanotextured Carbon/VS_2 Composites as the Hybrid Electrodes in Electrochemical Capacitors*
   M. Foroutan Koudahi, E. Frąckowiak
   Poster, August 19-September 03, 2021, 72nd Annual Meeting of the International Society of Electrochemistry (ISE)
   Jeju Island, Korea (on-line)
5) *Carbon materials as a support for TMD based supercapacitor electrodes*
   M. Tobis, M. Foroutan Koudahi, E. Frąckowiak
   Oral, July 03-08, 2022, Carbon 2022
   London, UK
6) *Hybrid electrochemical capacitors based on Transition Metal Dichalcogenides and carbon-based materials*
   M. Foroutan Koudahi, E. Frąckowiak
   Poster, August 15-19, 2022, Regional Meeting of the International Society of Electrochemistry (ISE)
   Prague, Czech Republic
7) *The Effect of Carbon Texture on the Performance of TMD Based Supercapacitor Electrodes*

E. Frąckowiak, M. Foroutan Koudahi, M. Tobis,

Oral, July 16-21, 2023, Carbon 2023

Cancun, Mexico

8) *MXenes as intriguing material for energy storage*

M. Foroutan Koudahi, E. Frąckowiak

Oral, September 26-29, 2023, ICAC 2023

Kamakura, Japan

9) *The Electrode/Electrolyte Interface in MXene-Based Electrochemical Capacitors*

M. Foroutan Koudahi, E. Frąckowiak

Oral, October 8-12, 2023, 244th meeting of The Electrochemical Society (ECS)

Gothenburg, Sweden

11. Reseach Project

1) OPUS, National Science Centre of Poland

Study of the electrode/electrolyte interface of high stability and quick charge response

Project No.: 2018/31/B/ST4/01852

Project coordinator: Prof. dr hab. Elżbieta Frąckowiak

mgr inż. Masoud Foroutan Koudahi involved as the contractor

2) Preludium 21, National Science Centre of Poland

Preparation and characterization of novel 2D MXenes material

Project No.: 2022/45/N/ST5/02275

Project coordinator: mgr inż. Masoud Foroutan Koudahi

Literature

1. Khan k., Tareen A., Aslam M., Mahmood A., Khan Q., Zhang Y., Ouyang Z., Guo Z., Zhang H., Going green with batteries and supercapacitor: Two dimensional materials and their nanocomposites based energy storage applications, Progress in Solid State Chemistry, 2020, *58*, 100254. https://doi.org/10.1016/j.progsolidstchem.2019.100254.

2. Dyatkin B., Presser V., Heon M., Lukatskaya M., Beidaghi M., Gogotsi Y., Development of a Green Supercapacitor Composed Entirely of Environmentally Friendly Materials, ChemSusChem, 2013, *6*, 2269-2280. https://doi.org/10.1002/cssc.201300852.

3. Gosh S., Yadav S., Devi A., Thomas T., Techno-economic understanding of Indian energy-storage market: A perspective on green materials-based supercapacitor technologies, Renew Sustain Energy Rev, 2016, *161*, 112412. https://doi.org/10.1016/j.rser.2022.112412.

4. Chang Z., Yang Y., Li M., Wang X., Wu Y., Green energy storage chemistries based on neutral aqueous electrolytes, J. Mater. Chem. A, 2014, 2, 10739-10755. https://doi.org/10.1039/C4TA00565A.

5. Saikia B., Benoy S., Bora M., Tamuly J., Pandey M., Bhattacharya D., A brief review on supercapacitor energy storage devices and utilization of natural carbon resources as their electrode materials, Fuel, 2020, 282, 118796. https://doi.org/10.1016/j.fuel.2020.118796.

6. Libich. J, Maca. J, Vondrak. J, Cech. O, Sedlarikova. M, Supercapacitors: Properties and applications, J. Energy Storgae, 2018, 17, 224-227. https://doi.org/10.1016/j.est.2018.03.012.

6. Kalair A., Abas N., Saleem M., Kalair A., Khan N., Role of energy storage systems in energy transition from fossil fuels to renewables, Energy Storgae, 2020, 3, 135. https://doi.org/10.1002/est2.135.

7. Yin Y., Liu Q., Zhao Y., Chen T., Wang J., Gui L., Lu C., Recent Progress and Future Directions of Biomass-Derived Hierarchical Porous Carbon: Designing, Preparation, and Supercapacitor Applications, energyfuels, 2023, 5, 3523-3554. https://doi.org/10.1021/acs.energyfuels.2c04093.

8. Zaboor A., Mehr F., Mao G., Yu Y., Sapi A., The carbon neutrality feasibility of worldwide and in China's transportation sector by E-car and renewable energy sources

before 2060, J. Energy Storgae, 2023, 61, 106696. https://doi.org/10.1016/j.est.2023.106696.

9. Fu R., Li S., Yu J., Wang Z., Guo W., Xie Y., Yang L., Liu K., Ren W., Qiu J., A closed-loop and scalable process for the production of biomass-derived superhydrophilic carbon for supercapacitors, Green Chem, 2021, 23, 3400-3409. https://doi.org/10.1039/D1GC00670C.

10. Weisser F., Muller-Mahn D., No Place for the Political: Micro-Geographies of the Paris Climate Conference 2015, Antipode, 2016, 49, 802-820. https://doi.org/10.1111/anti.12290.

11. Vicente-Serrano S., Quiring S., Pena-Gallardo M., Yuan S., Dominguez-Castro F., A review of environmental droughts: Increased risk under global warming?, Earth-Science Rew, 2020, 201, 102953. https://doi.org/10.1016/j.earscirev.2019.102953.

12. Ledger M., Brown L., Edwards F., Milner A., Woodward G., Drought alters the structure and functioning of complex food webs, Nature Clim Change, 2013, 3, 223-227. https://doi.org/10.1038/nclimate1684.

13. Berrill P., Wilson E., Reyna J., Fontanini A., Hertwich E., Decarbonization pathways for the residential sector in the United States, Nature Clim Change, 2022, 12, 712-718. https://doi.org/10.1038/s41558-022-01429-y.

14. bildirici M., Gokmenoglu S., Environmental pollution, hydropower energy consumption and economic growth: Evidence from G7 countries, Renew Sustain Energy Rev, 2017, 75, 68-85. https://doi.org/10.1016/j.rser.2016.10.052.

15. Rosillo-Calle F., A review of biomass energy – shortcomings and concerns, J. Chem. Technol. Biotechnol., 2016, 91, 1933-1945. https://doi.org/10.1002/jctb.4918.

16. Shetty C., Priyam A., A review on tidal energy technologies, Mater. Today Proc., 2022, 56, 2774-2779. https://doi.org/10.1016/j.matpr.2021.10.020.

17. Villanueva D., Feijoo A., Wind power distributions: A review of their applications, Renew Sustain Energy Rev, 2010, 14, 1490-1495. https://doi.org/10.1016/j.rser.2010.01.005.

18. Kannan N., Vakeesan D., Solar energy for future world: - A review, Renew Sustain Energy Rev, 2016, 62, 1092-1105. https://doi.org/10.1016/j.rser.2016.05.022.

19. Batlle C., Rodilla P., A critical assessment of the different approaches aimed to secure electricity generation supply, Energy Policy, 2010, 38, 7169-7179. https://doi.org/10.1016/j.enpol.2010.07.039.

20. Paz F., Fernandez P., Addressing 2030 EU policy framework for energy and climate: Cost, risk and energy security issues, Energy, 2016, 115, 1347-1360. https://doi.org/10.1016/j.energy.2016.01.068.

21. Powells G., Bulkeley H., Bell S., Judson E., Peak electricity demand and the flexibility of everyday life, Geoforum, 2014, 55, 43-52. https://doi.org/10.1016/j.geoforum.2014.04.014.

22. Powells G., Bulkeley H., Bell S., Judson E., Household energy resilience in extreme weather events: An investigation of energy service importance, HVAC usage behaviors, and willingness to pay, Applied Energy, 2024, 363, 123051. https://doi.org/10.1016/j.apenergy.2024.123051.

23. Sanni S., Oricha J., Oyewole T., Bawonda F., Analysis of backup power supply for unreliable grid using hybrid solar PV/diesel/biogas system, Applied Energy, 2021, 227, 120506. https://doi.org/10.1016/j.energy.2021.120506.

24. Yang Y., Wang M., Liu Y., Zhang L., Peak-off-peak load shifting: Are public willing to accept the peak and off-peak time of use electricity price?, J. Clean. Prod. , 2018, 199, 1066-1071. https://doi.org/10.1016/j.jclepro.2018.06.181.

25. Bruno F., Tay N., Belusko M., Minimising energy usage for domestic cooling with off-peak PCM storage, Energy Build., 2014, 76, 347-353. https://doi.org/10.1016/j.enbuild.2014.02.069.

26. Thomaben G., Kavvadias K., Navarro J., The decarbonisation of the EU heating sector through electrification: A parametric analysis, Energy Policy, 2021, 148, 111929. https://doi.org/10.1016/j.enpol.2020.111929.

27. Nieto J., Moyano P., Moyano D., Miguel L., Is energy intensity a driver of structural change? Empirical evidence from the global economy, J. Ind. Ecol., 2022, 27, 283-296. https://doi.org/10.1111/jiec.13352.

28. Spear B., James Watt: The steam engine and the commercialization of patents, World Pat. Inf., 2008, 30, 53-58. https://doi.org/10.1016/j.wpi.2007.05.009.

29. Parsons C., Stoney G., The Steam-Turbine, ICE Virtual Library, 1906, 163, 167-198. https://doi.org/10.1680/imotp.1906.16610.

30. Yang J., Yu Y., Ma T., Cuiguang Z., Wang Q., Evolution of energy and metal demand driven by industrial revolutions and its trend analysis, China Popul. Resour. Environ., 2021, 19, 256-264. https://doi.org/10.1016/j.cjpre.2021.12.028.

31. Gur T., Review of electrical energy storage technologies, materials and systems: challenges and prospects for large-scale grid storage, Energy Environ. Sci., 2018, 11, 2696-2767. https://doi.org/10.1039/C8EE01419A.

32. Popovic A., Gvozdenovic M., Jankovic A., Jugovic B., Grugur B., Polypyrrole on graphite: An exemplary model system for comprehensive electrochemical analysis of energy storage materials, Synth. Met., 2023, 297, 117386. https://doi.org/10.1016/j.synthmet.2023.117386.

33. Schutter C., Pohlmann S., Balducci A., Industrial Requirements of Materials for Electrical Double Layer Capacitors: Impact on Current and Future Applications, Adv. energy Mater, 2019, 9, 1900334. https://doi.org/10.1002/aenm.201900334.

34. Wang Y., Song Y., Xia Y., Electrochemical capacitors: mechanism, materials, systems, characterization and applications, Chem. Soc. Rev, 2016, 45, 5925-5950. https://doi.org/10.1039/C5CS00580A.

35. Kim T., Song W., Son D., Ono L., Qi Y., Lithium-ion batteries: outlook on present, future, and hybridized technologies, J. Mater. Chem. A, 2019, 7, 2942-2964. https://doi.org/10.1039/C8TA10513H.

36. Lucia U., Overview on fuel cells, Renew. Sustain. Energy Rev., 2014, 30, 164-169. https://doi.org/10.1016/j.rser.2013.09.025.

37. Sun J., Luo B., Li H., A Review on the Conventional Capacitors, Supercapacitors, and Emerging Hybrid Ion Capacitors: Past, Present, and Future, Adv. Energy Sustainability Res., 2022, 3, 2100191. https://doi.org/10.1002/aesr.202100191.

38. Chung D., Development, design and applications of structural capacitors, Renew. Sustain. Appl. Energy, 2018, 231, 89-101. https://doi.org/10.1016/j.apenergy.2018.09.132.

39. Yao S., Yuan J., Mehedi H., Gheeraert E., Carbon nanotube forest based electrostatic capacitor with excellent dielectric performances, Carbon, 2017, 116, 648-654. https://doi.org/10.1016/j.carbon.2017.02.043.

40. Shiraishi S., Kurihara H., Okabe K., Hulicova D., Oya A., Electric double layer capacitance of highly pure single-walled carbon nanotubes (HiPco™Buckytubes™) in propylene carbonate electrolytes, Electrochem. Comm., 2002, 4, 593-598. https://doi.org/10.1016/S1388-2481(02)00382-X.

41. Jang H., Jo M., Ahn H., Tailored functional group vitalization on mesoporous carbon nanofibers for ultrafast electrochemical capacitors, Appl. Surf. Sci., 2023, 623, 157081. https://doi.org/10.1016/j.apsusc.2023.157081.

42. Pan Q., Tong Z., Su Y., Qin S., Tang Y., Energy Storage Mechanism, Challenge and Design Strategies of Metal Sulfides for Rechargeable Sodium/Potassium-Ion Batteries, Adv. Funct. Mater., 2021, 31, 2103912. https://doi.org/10.1002/adfm.202103912.

43. Winter M., Brodd R., What Are Batteries, Fuel Cells, and Supercapacitors?, Chem. Rev., 2004, 104, 4245-4270. https://doi.org/10.1016/j.apsusc.2023.157081.

44. Zhang R., Xu H., Luo D., Chi J., Fan Z., Dou H., Zhang X., Noncovalent interactions engineering construct the fast-kinetics organic cathode for room/low-temperature aqueous zinc-ion battery, J. Chem. Eng., 2023, 458, 141336. https://doi.org/10.1016/j.cej.2023.141336.

45. Gao X., Yang H., Multi-electron reaction materials for high energy density batteries, Energy Environ. Sci., 2010, 3, 174-189. https://doi.org/10.1039/B916098A.

46. Coromina H., Adeniran B., Mokaya R., Walsh D., Bridging the performance gap between electric double-layer capacitors and batteries with high-energy/high-power carbon nanotube-based electrodes†, J. Mater. Chem. A, 2016, 4, 14586-14594. https://doi.org/10.1039/C6TA05686E.

47. Forse A., Merlet C., Griffin J., Grey C., New Perspectives on the Charging Mechanisms of Supercapacitors, JACS, 2016, 138, 5731-5744. https://doi.org/10.1021/jacs.6b02115.

48. Zuo W., Ruizhi L., Zhou C., Li Y., Xia J., Liu J., Battery-Supercapacitor Hybrid Devices: Recent Progress and Future Prospects, Adv. Sci., 2017, 4, 1600539. https://doi.org/10.1002/advs.201600539.

49. Mukhopadhyay A., Sheldon B., Deformation and stress in electrode materials for Li-ion batteries, Prog. Mater. Sci., 2014, 63, 58-116. https://doi.org/10.1002/advs.201600539.

50. Frackowiak E., Beguin F., Carbon materials for the electrochemical storage of energy in capacitors, Carbon, 2001, 39, 937-950. https://doi.org/10.1016/S0008-6223(00)00183-4.

51. Platek A., Piwek J., Fic K., Frackowiak E., Ageing mechanisms in electrochemical capacitors with aqueous redox-active electrolytes, Electrochim. Acta, 2019, 311, 211-220. https://doi.org/10.1016/j.electacta.2019.04.117.

52. Beguin F., Presser V., Balducci A., Frackowiak E., Carbons and Electrolytes for Advanced Supercapacitors, Adv. Mater., 2014, 26, 2219-2251. https://doi.org/10.1002/adma.201304137.

53. Simon P., Gogotsi Y., Materials for electrochemical capacitors, Nat. Mater, 2008, 7, 845-854. https://doi.org/10.1038/nmat2297.

54. Lewandowski A., Galinski M., Practical and theoretical limits for electrochemical double-layer capacitors, J. Power Sources, 2007, 173, 822-828. https://doi.org/10.1016/j.jpowsour.2007.05.062.

55. Tan J., Zhiheng L., Ye M., Shen J., Nanoconfined Space: Revisiting the Charge Storage Mechanism of Electric Double Layer Capacitors, ACS Appl. Mater. Interfaces, 2022, 14, 37259-37269. https://doi.org/10.1021/acsami.2c07775.

56. Menzel J., Frackowiak E., Fic K., Agar-based aqueous electrolytes for electrochemical capacitors with reduced self-discharge, Electrochim. Acta., 2020, 332, 135435. https://doi.org/10.1016/j.electacta.2019.135435.

57. Kotz R., Carlen M., Principles and applications of electrochemical capacitors, Electrochim. Acta., 2000, 45, 2483-2498. https://doi.org/10.1016/S0013-4686(00)00354-6.

58. Zhao X., Koichi A., Chen J., Nishiumi T., Examination of the Gouy–Chapman theory for double layer capacitance in deionized latex suspensions, RSC Adv., 2014, 4, 63171-63181.
https://doi.org/10.1039/C4RA11258J.

59. Gorska B., Timperman L., Anouti M., Begiun F., Effect of low water content in protic ionic liquid on ions electrosorption in porous carbon: application to electrochemical capacitors, Phys. Chem. Chem. Phys., 2017, 19, 11173-11186. https://doi.org/10.1039/C7CP00398F.

60. Eftekhari A., Surface Diffusion and Adsorption in Supercapacitors, ACS Sustainable Chem. Eng., 2019, 7, 3692–3701. https://doi.org/10.1021/acssuschemeng.8b01075.

61. Elliott J., Chiricotto M., Troisi A., Carbone P., Do specific ion effects influence the physical chemistry of aqueous graphene-based supercapacitors? Perspectives from multiscale QMMD simulations, Carbon, 2023, 207, 292-304. https://doi.org/10.1016/j.carbon.2023.03.019.

62. Eftekhari A., The mechanism of ultrafast supercapacitors, J. Mater. Chem. A, 2018, 6, 2866-2876. https://doi.org/10.1039/C7TA10013B.

63. Kang J., Wen J., Jayaram S., Yu A., Wang X., Development of an equivalent circuit model for electrochemical double layer capacitors (EDLCs) with distinct electrolytes, Electrochim. Acta., 2014, 115, 587-598. https://doi.org/10.1016/j.electacta.2013.11.002.

64. Iglic A., Gongadze E., Kralj-iglic V., Differential Capacitance of Electric Double Layer – Influence of Asymmetric Size of Ions, Thickness of Stern Layer and Orientational Ordering of Water Dipoles, Acta Chim. Slov, 2019, 66, 534-541. http://dx.doi.org/10.17344/acsi.2019.5495.

65. Pandolfo A., Hollenkamp A., Carbon properties and their role in supercapacitors, j. Power Source, 2006, 157, 11-27. https://doi.org/10.1016/j.jpowsour.2006.02.065.

66. Fleischmann S., Mitchell J., Wang R., Zhan C., Jiang D., Presser V., Augustyn V., Pseudocapacitance: From Fundamental Understanding to High Power Energy Storage Materials, Chem. Rev., 2020, 120, 6738-67182. https://doi.org/10.1021/acs.chemrev.0c00170.

67. Chodankar N., Pham H., Nanjundan A., Fernando J., Jayaramulu K., Golberg D., Han Y., Dubal D., True Meaning of Pseudocapacitors and Their Performance Metrics: Asymmetric versus Hybrid Supercapacitors, Small, 2020, 16, 2002806.

https://doi.org/10.1002/smll.202002806.

68. Brousse T., Belanger D., Long J., To Be or Not To Be Pseudocapacitive?, J. Electrochem. Soc., 2015, 162, 5185.
http://dx.doi.org/10.1149/2.0201505jes.

69. Conway B., Gileadi E., Kinetic Theory of Pseudo-Capacitance and Electrode Reactions at Appreciable Surface Coverage, Trans. Faraday Soc., 1962, 58, 2493-2509.
https://doi.org/10.1039/TF9625802493.

70. Conway B., Birss V., Wojtowicz J., The role and utilization of pseudocapacitance for energy storage by supercapacitors, J. Power Source, 1997, 66, 1-14.
https://doi.org/10.1016/S0378-7753(96)02474-3.

71. Mu X., Wang D., Du F., Chen G., Wang C., Wei Y., Gogotsi Y., Gao Y., Dall'Agnese Y., Revealing the Pseudo-Intercalation Charge Storage Mechanism of MXenes in Acidic Electrolyte, Adv. Funct. Mater, 2019, 29, 1902953.
https://doi.org/10.1002/adfm.201902953.

72. Ando Y., Okubo M., Yamada A., Otani M., Capacitive versus Pseudocapacitive Storage in MXene, Adv. Funt. Mater, 2020, 30, 2000820.
https://doi.org/10.1002/adfm.202000820.

73. Zhang M., Song X., Xu O., Tang Y., Rechargeable batteries based on anion intercalation graphite cathodes, Energy Storage Mater., 2019, 16, 65-84.
https://doi.org/10.1016/j.ensm.2018.04.023.

74. Lokhande C., Dubal D., Joo O., Metal oxide thin film based supercapacitors, Curr. Appl. Phys., 2011, 11, 255-270.
https://doi.org/10.1016/j.cap.2010.12.001.

75. An C., Wang Y., Huang Y., Xu Y., Jiao L., Yuan H., Porous NiCo2O4 nanostructures for high performance supercapacitors via a microemulsion technique, Nano Energy, 2014, 10, 125-134.
https://doi.org/10.1016/j.nanoen.2014.09.015.

76. Lin T., Sadhasivam T., Wang A., Chen T., Lin J., Shao L., Ternary Composite Nanosheets with MoS2/WS2/Graphene Heterostructures as High-Performance Cathode Materials for Supercapacitors, ChemElectroChem, 2018, 5, 1024-1031.

https://doi.org/10.1002/celc.201800043.

77. Wang F., Xiao S., Hou Y., Hu C., Liu L., Wu Y., Electrode materials for aqueous asymmetric supercapacitors, RSC Adv., 2013, 3, 13059-13084. https://doi.org/10.1039/C3RA23466E.

78. Yu N., Guo K., Zhang W., Wang X., Zhu M., Flexible high-energy asymmetric supercapacitors based on MnO@C composite nanosheet electrodes, J. Mater. Chem. A, 2017, 5, 804-813. https://doi.org/10.1016/S0378-7753(96)02474-3.

79. Choudhary N., Li C., Moore J., Nagaiah N., Zhai L., Jung Y., Thomas J., Asymmetric Supercapacitor Electrodes and Devices, Adv. Mater., 2017, 29, 1605336. https://doi.org/10.1002/adma.201605336.

80. Zhang G., Feng M., Li Q., Wang Z., Fang Z., Niu Z., Qu N., Fan X., Li S., Gu J., Wang J., Wang D., High Energy Density in Combination with High Cycling Stability in Hybrid Supercapacitors, ACS Appl. Mater. Interfaces, 2022, 14, 2674-2682. https://doi.org/10.1021/acsami.1c17285.

81. Zhang S., Yin B., Liu X., Gu D., Gong H., Wang Z., A high energy density aqueous hybrid supercapacitor with widened potential window through multi approaches, Nano Energy, 2019, 59, 41-49. https://doi.org/10.1016/j.nanoen.2019.02.001.

82. Zhang F., Zhang T., Ynag X., Zhang L., Leng K., Huang Y., Chen Y., A high-performance supercapacitor-battery hybrid energy storage device based on graphene-enhanced electrode materials with ultrahigh energy density, Energy Environ. Sci., 2013, 6, 1623-1632. https://doi.org/10.1039/C3EE40509E.

83. Zhao J., Li Z., Yuan X., Yang Z., Zhang M., Meng A., Li Q., A High-Energy Density Asymmetric Supercapacitor Based on Fe2O3 Nanoneedle Arrays and NiCo2O4/Ni(OH)2 Hybrid Nanosheet Arrays Grown on SiC Nanowire Networks as Free-Standing Advanced Electrodes, Adv. Energy Mater., 2018, 8, 17002787. https://doi.org/10.1002/aenm.201702787.

84. Xie B., Yu M., Lu L., Feng H., Yang Y., Chen Y., Cui H., Xiao R., Liu J, Pseudocapacitive Co9S8/graphene electrode for high-rate hybrid supercapacitors, Carbon, 2019, 141, 134-142.
https://doi.org/10.1016/j.carbon.2018.09.044.

85. Wang Q., Yan J., Fan Z., Carbon materials for high volumetric performance supercapacitors: design, progress, challenges and opportunities, Energy Environ. Sci., 2016, 9, 729-762. https://doi.org/10.1039/C5EE03109E.

86. Liu C., Liu Y., Yi T., Hu C., Carbon materials for high-voltage supercapacitors, Carbon, 2019, 145, 529-548.
https://doi.org/10.1016/j.carbon.2018.12.009.

87. Kate R., Khalate S., Deokate R., Overview of nanostructured metal oxides and pure nickel oxide (NiO) electrodes for supercapacitors: A review, J. Alloys Compd., 2018, 734, 89-111. https://doi.org/10.1016/j.jallcom.2017.10.262.

88. Nguyen T., Montemor M., Metal Oxide and Hydroxide–Based Aqueous Supercapacitors: From Charge Storage Mechanisms and Functional Electrode Engineering to Need-Tailored Devices, Adv. Sci., 2019, 6, 1801797.
https://doi.org/10.1002/advs.201801797.

89. Gao Y., Zhao L., Review on recent advances in nanostructured transition-metal-sulfide-based electrode materials for cathode materials of asymmetric supercapacitors, J. Chem. Eng., 2022, 430, 132745.
https://doi.org/10.1016/j.cej.2021.132745.

90. Murali G., Rawal J., Modigunta J., Park Y., Lee J., Lee S., Park S., In I., A review on MXenes: new-generation 2D materials for supercapacitors, Sustainable Energy Fuels, 2021, 5, 5672-5693.
https://doi.org/10.1039/D1SE00918D.

91. Han Y., Dai L., Conducting Polymers for Flexible Supercapacitors, Macromol. Chem. Phys., 2019, 220, 1800355.
https://doi.org/10.1002/macp.201800355.

92. Qi D., Liu Y., Liu Z., Zhang L., Chen X., Design of Architectures and Materials in In-Plane Micro-supercapacitors: Current Status and Future Challenges, Adv Mater., 2016, 29, 1602802. https://doi.org/10.1002/adma.201602802.

93. Zhang L., Gu Y., Zhao X., Advanced porous carbon electrodes for electrochemical capacitors, J. Mater. Chem. A, 2013, 1, 9395-9408. https://doi.org/10.1039/C3TA11114H.

94. Frackowiak E., Abbas Q., Bequin F., Carbon/carbon supercapacitors, J. Energy Chem., 2013, 22, 226-240. https://doi.org/10.1016/S2095-4956(13)60028-5.

95. Prabaharan S., Vimala R., Zainal Zulkarnian., Nanostructured mesoporous carbon as electrodes for supercapacitors, J. Power Source, 2006, 161, 730-736. https://doi.org/10.1016/j.jpowsour.2006.03.074.

96. Dou Q., Park H., Perspective on High-Energy Carbon-Based Supercapacitors, Energy Environ. Mater., 2020, 3, 286-305. https://doi.org/10.1002/eem2.12102.

97. Chen X., Chen C., Zhang Z., Xie D., Deng X., Liu J., Nitrogen-doped porous carbon for supercapacitor with long-term electrochemical stability, J. Power Source., 2013, 230, 50-58. https://doi.org/10.1016/j.jpowsour.2012.12.054.

98. Xu B., Hou S., Cao G., Chu M., Yang Y., Easy synthesis of a high surface area, hierarchical porous carbon for high-performance supercapacitors, RSC Adv., 2013, 3, 17500-17506. https://doi.org/10.1039/C3RA41250D.

99. Long C., Jiang L., Wu X., Jiang Y., Yang D., Wang C., Wei T., Fan Z., Facile synthesis of functionalized porous carbon with three-dimensional interconnected pore structure for high volumetric performance supercapacitors, Carbon, 2015, 93, 412-420. https://doi.org/10.1016/j.carbon.2015.05.040.

100. Liu L., Wang X., Gao J., Zhang Y., Lu Q., Liu M., Hollow porous carbon spheres with hierarchical nanoarchitecture for application of the high performance supercapacitors, Electrochim. Acta, 2016, 211, 183-192. https://doi.org/10.1016/j.electacta.2016.05.217.

101. Frackowiak E., Carbon materials for supercapacitor application, Phys. Chem. Chem. Phys., 2007, 9, 1774-1785. https://doi.org/10.1039/B618139M.

102. Kleszyk P., Ratajczak P., Skowron P., Jagiello J., Abbas Q., Frackowiak E., Begiun F., Carbons with narrow pore size distribution prepared by simultaneous carbonization and self-activation of tobacco stems and their application to supercapacitors, Carbon, 2015, 81, 148-157. https://doi.org/10.1016/j.carbon.2014.09.043.

103. Zhang G., Chen Y., Chen Y., Guo H., Activated biomass carbon made from bamboo as electrode material for supercapacitors, Mater. Res. Bull., 2018, 102, 391-398. https://doi.org/10.1016/j.materresbull.2018.03.006.

104. Jin Z., Yan X., Yu Y., Zhao G., Sustainable activated carbon fibers from liquefied wood with controllable porosity for high-performance supercapacitors, J. Mater. Chem. A, 2014, 2, 11706-11715. https://doi.org/10.1039/C4TA01413H.

105. Frackowiak E., Beguin F., Carbon materials for the electrochemical storage of energy in capacitors, Carbon, 2001, 39, 937-950. https://doi.org/10.1016/S0008-6223(00)00183-4.

106. Galek P., Frackowiak E., Fic K., Interfacial aspects induced by saturated aqueous electrolytes in electrochemical capacitor applications, Electrochim Acta, 2020, 334, 135572. https://doi.org/10.1016/j.electacta.2019.135572.

107. Anita S., Hanifah T., Itnawita, Kartika G., Preparation and characterization of activated carbon from the nipa fruit shell irradiated by microwave: Effect temperatures and time of carbonization, Mater. Today Proc., 2023, 87, 390-395. https://doi.org/10.1016/j.matpr.2023.04.172.

108. Pallares J., Gonzalez-Cencerrado A., Arauzo I., Production and characterization of activated carbon from barley straw by physical activation with carbon dioxide and steam, Biomass Bioenergy, 2018, 115, 64-73. https://doi.org/10.1016/j.biombioe.2018.04.015.

109. Al Subi H., Adeeb M., Pandey M., Sadeq H., Kumar D., Shuka S., Effect of different activation agents on the pollution removal efficiency of date seed activated carbon: process optimization using response surface methodology, Appl. Water Sci., 2020, 10, 166. https://doi.org/10.1007/s13201-020-01251-x.

110. Yang H., Zhang D., Chen Y., Ran M., Gu J., Study on the application of KOH to produce activated carbon to realize the utilization of distiller's grains, IOP Conf. Ser.: Earth Environ. Sci., 2017, 69, 12051. doi :10.1088/1755-1315/69/1/012051.

111. Platek-Mielczarek A., Nita C., Ghimbeu C., Frackowiak E., Fic K., Link between Alkali Metals in Salt Templates and in Electrolytes for Improved Carbon-Based Electrochemical Capacitors, ACS Appl. Mater. Interfaces, 2021, 13, 2584-2599. https://doi.org/10.1021/acsami.0c18627.

112. Guerin D., Lenfant S., Godey S., Vuillaume D., Synthesis and electrical properties of fullerene-based molecular junctions on silicon substrate, J. Mater. Chem., 2010, 20, 2680-2690. https://doi.org/10.1039/B924255D.

113. Giacalone F., Martin N., Fullerene Polymers: Synthesis and Properties, Chem. Rev., 2006, 106, 5136-5190. https://doi.org/10.1021/cr068389h.

114. Jiang B., Zhang G., Tang Q., Meng F., Zhou D., Zhao W., Jiang W., Ji Q., Tailoring co-doping of cobalt and nitrogen in a fullerene-based carbon composite and its effect on the supercapacitive performance, Mater. Adv., 2022, 3, 1539-1546. https://doi.org/10.1039/D1MA00937K.

115. Lv Y., Wang J., Ji Dingwei., Li Jianhang., Zhao S., Zhao Y., Cai Z., He X., Sun X., Carbonaceous electrode materials for supercapacitor: Preparation and surface functionalization, Front. Energy Res., 2023, 10, 957032. https://doi.org/10.3389/fenrg.2022.957032.

116. Kakaei K., Khodadoost S., Gholipour M., Shouraei N., Core-shell polyaniline functionalized carbon quantum dots for supercapacitor, J. Phys. Chem. Solids, 2021, 148, 109753. https://doi.org/10.1016/j.jpcs.2020.109753.

117. Peigney A., Laurent C., Flahaut E., Bacsa R., Rousset A., Specific surface area of carbon nanotubes and bundles of carbon nanotubes, Carbon, 2001, 39, 507-514. https://doi.org/10.1016/S0008-6223(00)00155-X.

118. Zhong M., Zhang M., Li X., Carbon nanomaterials and their composites for supercapacitors, Carbon Energy, 2022, 4, 950-985. https://doi.org/10.1002/cey2.219.

119. Xu R., Wei J., Guo F., Cui X., Zhang T., Zhu H., Wang K., Wu D., Highly conductive, twistable and bendable polypyrrole–carbon nanotube fiber for efficient supercapacitor

electrodes, RSC Adv., 2015, 5, 22015-22021. https://doi.org/10.1039/C5RA01917F.

120. Yan J., Dong K., Zhang Y., Wang X., Abdolhassan A., Yu J., Ding B., Multifunctional flexible membranes from sponge-like porous carbon nanofibers with high conductivity, Nat Commun, 2019, 10, 5584. https://doi.org/10.1038/s41467-019-13430-9.

121. Ra E., Raymundo-Pinero E., Lee Y., Begiun F., High power supercapacitors using polyacrylonitrile-based carbon nanofiber paper, Carbon, 2021, 35, 8396-8405. https://doi.org/10.1016/j.carbon.2009.06.051.

122. Allado K., Liu M., Jayapalan A., Arvapali D., Nowlin K., Wei J., Binary MnO_2/Co_3O_4 Metal Oxides Wrapped on Superaligned Electrospun Carbon Nanofibers as Binder Free Supercapacitor Electrodes, Energy Fuels, 2021, 35, 8396-8405. https://doi.org/10.1021/acs.energyfuels.1c00556.

123. Berry V., Impermeability of graphene and its applications, Nat Commun, 2013, 62, 1-10. https://doi.org/10.1016/j.carbon.2013.05.052.

124. Ke Q., Wang J., Graphene-based materials for supercapacitor electrodes – A review, J Materiomics, 2016, 2, 37-54. https://doi.org/10.1016/j.jmat.2016.01.001.

125. Yi M., Shen Z., A review on mechanical exfoliation for the scalable production of graphene, J. Mater. Chem. A, 2015, 3, 11700-11715. https://doi.org/10.1039/C5TA00252D.

126. Deokar G., Jin J., Schwingenschlogl J., Costa P., Chemical vapor deposition-grown nitrogen-doped graphene's synthesis, characterization and applications, npj 2D Mater. Appl., 2022, 06, 5584. https://doi.org/10.1038/s41699-022-00287-8.

127. Li Z., Young R., Backes C.., Zhao W., A., Yu J., Tillotson E., Conlan A., Ding F., Haigh S., Novoselov K., Coleman J., Mechanisms of Liquid-Phase Exfoliation for the Production of Graphene, ACS Nano, 2020, 14, 10975-10985. https://doi.org/10.1021/acsnano.0c03916.

128. Hummers Jr W., Offeman E., Preparation of Graphitic Oxide, JACS, 1958, 80, 1339. https://doi.org/10.1021/ja01539a017.

129. Marcano D., Kosynkin D., Berlin J., Sinitskii A., Sun Z., Slesarev A., Alemany L., Lu W., Tour J., Improved Synthesis of Graphene Oxide, ACS Nano, 2010, 4, 4806-4814. https://doi.org/10.1021/nn1006368.

130. Xu Y., Sheng K., Li C., Shi G., Self-Assembled Graphene Hydrogel via a One-Step Hydrothermal Process, ACS Nano, 2010, 4, 4324-4330. https://doi.org/10.1021/nn101187z.

131. Yu X., Hwang C., Jozwiak C., Kohl A., Schmid A., Lanzara A., New synthesis method for the growth of epitaxial graphene, J. Electron Spectros. Relat. Phenomena, 2011, 184, 100-106. https://doi.org/10.1016/j.elspec.2010.12.034.

132. Meyer J., Geim A., Katsnelson M., Novoselov K., Booth T., Roth S., The structure of suspended graphene sheets, Nature, 2007, 446, 60-63. https://doi.org/10.1038/nature05545.

133. Li X., Zhi L., Graphene hybridization for energy storage applications, Chem. Soc. Rev., 2017, 47, 3189-3216. https://doi.org/10.1039/C7CS00871F.

134. Wang Y., Wang X., Tang S., Vongehr S., Syed Junaid., Meng X., Highly processible and electrochemically active graphene-doped polyacrylic acid/polyaniline allowing the preparation of defect-free thin films for solid-state supercapacitors, RSC Adv., 2015, 5, 62670-62677. https://doi.org/10.1039/C5RA05486A.

135. Nomura K., Nishihara H., Kobayashi N., Asada T., Kyotani T., 4.4 V supercapacitors based on super-stable mesoporous carbon sheet made of edge-free graphene walls, Energy Environ. Sci., 2019, 12, 1542-1549. https://doi.org/10.1039/C8EE03184C.

136. Wang K., Li L., Zhang T., Liu Z., Nitrogen-doped graphene for supercapacitor with long-term electrochemical stability, Energy, 2014, 70, 612-617. https://doi.org/10.1016/j.energy.2014.04.034.

137. Sivakumar P., Raj C., Jung H., Park H., 2D/2D nanoarchitecture of Ni/$NiCo_2O_4$ deposited onto reduced graphene oxide for high-performance hybrid supercapacitor applications, J. Energy Storage, 2023, 69, 107946. https://doi.org/10.1016/j.est.2023.107946.

138. Kim Y., Lee G., Choi Y., Kim K., In Situ Growth of Novel Graphene Nanostructures in Reduced Graphene Oxide Microspherical Assembly with Restacking-Resistance and

Inter-Particle Contacts for Energy Storage Devices, Small, 2021, 17, 2101930. https://doi.org/10.1002/smll.202101930.

139. Banda H., Aradilla D., Benayad A., Chenavier Y., Daffos B., Dubois L., Duclairoir F., One-step synthesis of highly reduced graphene hydrogels for high power supercapacitor applications, J. Power Source, 2017, 360, 538-547. https://doi.org/10.1016/j.jpowsour.2017.06.033.

140. Meng X., Lu L., Sun C., Green Synthesis of Three-Dimensional MnO_2/Graphene Hydrogel Composites as a High-Performance Electrode Material for Supercapacitors, ACS Appl. Mater. Interfaces, 2018, 10, 16474-16481. https://doi.org/10.1021/acsami.8b02354.

141. Wu Y., Gao G., Wu G., Self-assembled three-dimensional hierarchical porous V_2O_5/graphene hybrid aerogels for supercapacitors with high energy density and long cycle life, Nat Commun, 2015, 3, 1828-1832. https://doi.org/10.1039/C4TA05537C.

142. Wu Z., Yang S., Sun Y., Parvez K., Feng X., Mullen K., 3D Nitrogen-Doped Graphene Aerogel-Supported Fe_3O_4 Nanoparticles as Efficient Electrocatalysts for the Oxygen Reduction Reaction, JACS, 2012, 134, 9082-9085. https://doi.org/10.1021/ja3030565.

143. Gao Y., Zhang S., Fu H., Ma J., Xu X., Guan L., Wu H., Wu Z., Three-dimensional nitrogen doped hierarchically porous carbon aerogels with ultrahigh specific surface area for high-performance supercapacitors and flexible micro-supercapacitors, Carbon, 2020, 168, 701-709. https://doi.org/10.1016/j.carbon.2020.06.063.

144. Cheng Y., Zhou S., Hu P., Zhao G., Li Y., Zhang X., Han W., Enhanced mechanical, thermal, and electric properties of graphene aerogels via supercritical ethanol drying and high-temperature thermal reduction, Sci Rep, 2017, 7, 1439. https://doi.org/10.1038/s41598-017-01601-x.

145. Garemark J., Yang X., Sheng X., Cheung O., Sun L., Berglund L., Li Y., Top-Down Approach Making Anisotropic Cellulose Aerogels as Universal Substrates for Multifunctionalization, ACS Nano, 2020, 14, 7111-7120. https://doi.org/10.1021/acsnano.0c01888.

146. White R., Brun N., Budarin V., Clark J., Always Look on the "Light" Side of Life: Sustainable Carbon Aerogels, ChemSusChem, 2014, 7, 670-689. https://doi.org/10.1002/cssc.201300961.

147. Mao M., Chen Q., Zhang H., Hou Y., Guo J., Superior cycling performance of NiC_2O_4/rGO/NF composites for hybrid supercapacitors, J. Energy Storage, 2023, 68, 107702. https://doi.org/10.1016/j.est.2023.107702.

148. Song Y., Yang S., Ding G., Zhang C., Xie X., Yu J., Ding B., Ultralight boron nitride aerogels via template-assisted chemical vapor deposition, Sci. Rep., 2015, 5, 10337. https://doi.org/10.1038/srep10337.

149. Araby S.,Qui A., Wang R., Zhao Z., Wang C., Ma J., Aerogels based on carbon nanomaterials., J. Mater. Sci., 2016, 51, 9157-9189. https://doi.org/10.1007/s10853-016-0141-z.

150. Wei W., Liu B., Gan Y., Ma H., Chen D., Qi J., Li S., One-step hydrothermal synthesis of Ni_3S_2/MoS_2 nanocomposites on rGO: Structural evolution and supercapacitor performance, Surf. Coat. Technol., 2020, 403, 126442. https://doi.org/10.1016/j.surfcoat.2020.126442.

151. Wang X., Zhang Y., Zhi C., Wang X., Tang D., Xu Y., Weng Q., Jiang X., Mitome M., Golberg D., Bando Y., Three-dimensional strutted graphene grown by substrate-free sugar blowing for high-power-density supercapacitors, Nat. Commun., 2013, 4, 2905. https://doi.org/10.1038/ncomms3905.

152. Yu Q., Jauregui L., Wu W., Colby R., Tian J., Su Z., Cao H., Liu Z., Pandey D., Wei D., Chung T., Peng P., Guisinger N., Stach E., Bao J., Pei S., Chen Y., Control and characterization of individual grains and grain boundaries in graphene grown by chemical vapor deposition, Nature Mater, 2011, 10, 443-449. https://doi.org/10.1038/nmat3010.

153. Naguib M., Barsoum M., Gogotsi Y., Ten Years of Progress in the Synthesis and Development of MXenes, Adv. Mater., 2021, 33, 2103393. https://doi.org/10.1002/adma.202103393.

154. Gao L., Bao W., Kuklin A., Mei S., Zhang H., Agren H., Hetero-MXenes: Theory, Synthesis, and Emerging Applications, Adv. Mater., 2021, 33, 2004129. https://doi.org/10.1002/adma.202004129 .

155. Anasori B., Lukatskaya M., Gogotsi Y., 2D metal carbides and nitrides (MXenes) for energy storage, Nat. Rev. Mater., 2017, 2, 16098. https://doi.org/10.1038/natrevmats.2016.98.

156. Liu K., Zhang L., Cao T., Jin C., Qiu D., Zhou Q., Zettl A., Yang P., Louie S., Wang F., Evolution of interlayer coupling in twisted molybdenum disulfide bilayers, Nat. Commun., 2014, 5, 4966. https://doi.org/10.1038/ncomms5966.

157. Ci P., Chen Y., Kang J., Suzuki R., Choe H., Suh J., Ko C., Park T., Shen K., Iwasa Y., Tongay S., Ager J., Wang L., Wu J., Quantifying van der Waals Interactions in Layered Transition Metal Dichalcogenides from Pressure-Enhanced Valence Band Splitting, Nano Lett., 2017, 17, 4982-4988. https://doi.org/10.1021/acs.nanolett.7b02159.

158. Shi Q., Shi E., Gustafsson M., Rhodes D., Kim B., Watanabe K., Taniguchi T., Papic Z., Hone J., Dean C., Odd- and even-denominator fractional quantum Hall states in monolayer WSe_2, Nanotechnol., 2020, 15, 16098. https://doi.org/10.1038/s41565-020-0685-6.

159. Phalswal P., Khanna P., Rubahn H., Mishra Y., Nanostructured molybdenum dichalcogenides: a review, Mater. Adv., 2022, 3, 5672-5697. https://doi.org/10.1039/D2MA00150K.

160. Bertolazzi S., Brivio J., Kis A., Stretching and Breaking of Ultrathin MoS_2, ACS Nano, 2011, 5, 9703-9709. https://doi.org/10.1021/nn203879f.

161. Frindt R., Yoffe A., Physical properties of layer structures : optical properties and photoconductivity of thin crystals of molybdenum disulphide, Proc.. Royal. Soc. A, 1963, 273, 69-83. https://doi.org/10.1098/rspa.1963.0075.

162. Toh R., Sofer Z., Luxa J., Sedmidubsky D., Pumera M., 3R phase of MoS_2 and WS_2 outperforms the corresponding 2H phase for hydrogen evolution, ACS Appl. Energy Mater., 2021, 4, 7405-7418. https://doi.org/10.1039/C6CC09952A.

163. Strachen J., Masters A., Maschmeyer T., 3R-MoS_2 in Review: History, Status, and Outlook, Nat. Rev. Mater., 2017, 2, 16098. https://doi.org/10.1021/acsaem.1c00638.

164. Wang P., Sun H., Ji Y., Li. W., Wang X., Three-Dimensional Assembly of Single-Layered MoS_2, Adv. Mater., 2013, 26, 964-969. https://doi.org/10.1002/adma.201304120.

165. Splendiani A., Sun L., Zhang Y., Li T., Kim J., Chim C., Galli G., Wang F., Emerging Photoluminescence in Monolayer MoS_2, Nano. Lett., 2010, 10, 1271-1275. https://doi.org/10.1021/nl903868w.

166. Tan Z., Kong X., Ng B., Soo H., Mohamed A., Chai S., Recent Advances in Defect-Engineered Transition Metal Dichalcogenides for Enhanced Electrocatalytic Hydrogen Evolution: Perfecting Imperfections, ACS Omega, 2023, 8, 1851-1863. https://doi.org/10.1021/acsomega.2c06524.

167. Zhang X., Jia F., Song S., Recent advances in structural engineering of molybdenum disulfide for electrocatalytic hydrogen evolution reaction, J. Chem. Eng., 2021, 405, 127013. https://doi.org/10.1016/j.cej.2020.127013.

168. Zhang Z., Wu S., Cheng J., Zhang W., MoS_2 nanobelts with (002) plane edges-enriched flat surfaces for high-rate sodium and lithium storage, Energy Storage Mater., 2018, 15, 65-74. https://doi.org/10.1016/j.ensm.2018.03.013.

168. Lin L., Wen L., Zhang S., Liu Y., Wallace G., Chen J., Two-dimensional transition metal dichalcogenides in supercapacitors and secondary batteries, Energy Storage Mater., 2019, 19, 408-423. https://doi.org/10.1016/j.ensm.2019.02.023.

169. Qiao Y., Sun W., Yu F., Yu J., Yao P., Zhu C., Xu J., Exploration of high performance and highly flexible supercapacitor configuration with MXene/1T-MoS_2 composite paper electrode, Electrochim. Acta, 2023, 464, 142929. https://doi.org/10.1016/j.electacta.2023.142929.

170. Chhowalla M., Shin H., Eda G., Li L., Loh K., Zhang H., The chemistry of two-dimensional layered transition metal dichalcogenide nanosheets, Nat. Chem., 2013, 5, 263-275. https://doi.org/10.1038/nchem.1589.

171. Feng J., Sun X., Wu C., Peng L., Lin C., Hu S., Yang J., Xie Y., Metallic Few-Layered VS_2 Ultrathin Nanosheets: High Two-Dimensional Conductivity for In-Plane Supercapacitors, JACS, 2011, 133, 17832-17838. https://doi.org/10.1021/ja207176c.

172. Acerce M., Voiry D., Chhowalla M., Metallic 1T phase MoS2 nanosheets as supercapacitor electrode materials, Nature Nanotech, 2015, 10, 313-318. https://doi.org/10.1038/nnano.2015.40.

173. Bissett M., Worrall S., Kinloch I., Dryfe R., Comparison of Two-Dimensional Transition Metal Dichalcogenides for Electrochemical Supercapacitors, Electrochim. Acta, 2016, 201, 30-37. https://doi.org/10.1016/j.electacta.2016.03.190.

174. Masikhwa T., Barzegar F., Dangbegnon J., Bello A., Madito M., Momodu D., Manyala N., Asymmetric supercapacitor based on VS_2 nanosheets and activated carbon materials, RSC Adv., 2016, 6, 38990-39000. https://doi.org/10.1039/C5RA27155J.

175. Crane M., Lim M., Zhou X., Pauzauskie P., Rapid synthesis of transition metal dichalcogenide–carbon aerogel composites for supercapacitor electrodes, Microsyst Nanoeng, 2017, 3, 17032. https://doi.org/10.1038/micronano.2017.32.

176. Hwu H., Chen J., Surface Chemistry of Transition Metal Carbides, Chem. Rev., 2005, 105, 185-212. https://doi.org/10.1021/cr0204606.

177. Naguib M., Kurtoglu M., Presser V., Lu J., Niu J., Heon M., Hultman L., Gogotsi Y., Barsoum M., Two-Dimensional Nanocrystals Produced by Exfoliation of Ti_3AlC_2, Adv. Mater., 2011, 23, 4248-4253. https://doi.org/10.1002/adma.201102306.

178. Wang B., Zhou A., Liu F., Cao J., Wang L., Hu Q., Carbon dioxide adsorption of two-dimensional carbide MXenes, j. Adv. Ceramics, 2018, 7, 237-245. https://doi.org/10.1007/s40145-018-0275-3.

179. Colkesen P., Fitriani P., Yoon D., Synthesis of Titanium Carbide MXene Nanosheets by Ecofriendly Technique for Strontium Ion Adsorption, Phys. Status Solidi C, 2023, 221, 2300564. https://doi.org/10.1002/pssa.202300564.

180. Lukatskaya M., Kota S., Lin Z., Zhao M., Shpigel N., Levi M., Halim J., Taberna P., Barsoum M., Simon P., Gogotsi Y., Ultra-high-rate pseudocapacitive energy storage in two-dimensional transition metal carbides, Nat. Energy, 2017, 2, 17105. https://doi.org/10.1038/nenergy.2017.105.

181. Yang S., Zhang P., Wang F., Ricciardulli A., Lohe M., Blom P., Feng X., Fluoride-Free Synthesis of Two-Dimensional Titanium Carbide (MXene) Using A Binary Aqueous

System, Angew. Chem., 2018, 130, 15717-15721. https://doi.org/10.1002/ange.201809662.

182. Liu L., Yin H., Guo W., Jia B., Jiang H., High Gravimetric Capacitance MXene Supercapacitor Electrode Based on Etched $Ti_3C_2T_x$ by Chemical Etching, Adv. Eng. Mater., 2023, 25, 2201425. https://doi.org/10.1002/adem.202201425.

183. Urbankowski P., Anasori B., Makaryan T., Er D., Kota S., Walsh P., Zhao M., Shenoy V., Barsoum M., Gogotsi Y., Synthesis of two-dimensional titanium nitride Ti_4N_3 (MXene), Nanoscale, 2016, 8, 11385-11391. https://doi.org/10.1039/C6NR02253G.

184. Chen J., Jin Q., Li Y., Shao H., Liu P., Liu Y., Taberna P., Huang Q, Lin Z., Simon P., Molten Salt-Shielded Synthesis (MS^3) of MXenes in Air, Energy Environ. Mater., 2021, 6, 12328. https://doi.org/10.1002/eem2.12328.

185. Wang X., Mathis T., Lin Z., Vlcek L., Torita T., Osti N., Hatter C., Urbankowski P., Sarycheva A., Tyagi M., Mamontov E., Simon P., Gogotsi Y., Influences from solvents on charge storage in titanium carbide MXenes, Nat. Energy, 2019, 4, 241-248. https://doi.org/10.1038/s41560-019-0339-9.

186. Jacques S., Di-Murro H., Berthet M., Vincent H., Pulsed reactive chemical vapor deposition in the C-Ti-Si system from $H_2/TiCl_4/SiCl_4$, Thin Solid Films, 2005, 478, 13-20. https://doi.org/10.1016/j.tsf.2004.09.043.

187. Eklund P., Beckers M., Jansson U., Hogberg H., Hultman L., The $M_{n+1}AX_n$ phases: Materials science and thin-film processing, Thin Solid Films, 2010, 518, 1851-1878. https://doi.org/10.1016/j.tsf.2009.07.184.

188. Zhou W., Mei B., Zhu J., Hong X., Synthesis of high-purity Ti3SiC2 and Ti_3AlC_2 by spark plasma sintering (SPS) technique, J. Mater. Sci., 2005, 40, 2099-2100. https://doi.org/10.1007/s10853-005-1245-z.

189. Siebert J., Bischoff L., Lepple M., Zintler A., Molina-Luna L., Wiedwald U., Birkel C., Sol–gel based synthesis and enhanced processability of MAX phase Cr_2GaC, J. Mater. Chem. C, 2019, 7, 6034-6040. https://doi.org/10.1039/C9TC01416K.

190. Zhong C., Deng Y., Hu W., Qiao J., Zhang L., Zhang J., A review of electrolyte materials and compositions for electrochemical supercapacitors, Chem. Soc. Rev., 2015, 25, 7484-7539. https://doi.org/10.1039/C5CS00303B.

191. Lethesh K., Bamgbopa M., Susantyoko R., Prospects and Design Insights of Neat Ionic Liquids as Supercapacitor Electrolytes, Front. Energy Res., 2021, 9, 741772. https://doi.org/10.3389/fenrg.2021.741772.

Co-authorship statement

POZNAN UNIVERSITY OF TECHNOLOGY

Faculty of Chemical Technology

Institute of Chemistry and Technical Electrochemistry

Masoud Foroutan Koudahi

March 27, 2024

Declaration of individual contribution in publications

As the co-author of the following papers, I hereby declare that my contribution to those works was:

Article 1: *Electrochemical Capacitor Performance of Nanotextured Carbon/Transition Metal Dichalcogenides Composites*

Authors: Elżbieta Frąckowiak (20%), **Masoud Foroutan Koudahi** (40%), Maciej Tobis (40%)

Journal: Small

DOI: https://doi.org/10.1002/smll.202006821

Contribution: - Investigation

- Data curation

- Writing (original draft)

Article 2: *Fast response supercapacitor based on carbon-VS_2 electrodes with a wide operating voltage range*

Authors: **Masoud Foroutan Koudahi** (70%), Elżbieta Frąckowiak (30%),

Journal: Energy Storage Materials

DOI: https://doi.org/10.1016/j.ensm.2022.04.021

Contribution: - Conceptualization

- Methodology
- Investigation
- Data curation
- Writing (original draft)

Article 3: *$Ti_3C_2T_x$ MXene as Intriguing Material for Electrochemical Capacitor*

Authors: **Masoud Foroutan Koudahi** (75%), Elżbieta Frąckowiak (25%),

Journal: Small

DOI: https://doi.org/10.1002/smll.202307165

Contribution: - Conceptualization

- Funding acquisition
- Investigation
- Data curation
- Writing (original draft)

Article 4: *Charge storage and operando electrochemical dilatometry of MXene electrodes in ionic liquids*

Authors: **Masoud Foroutan Koudahi** (55%), Andres Camilo Parejo Tovar (20%), François Béguin (10%), Elżbieta Frąckowiak **(15%)**

Journal: Submitted

DOI: -

Contribution: - Conceptualization

- Funding acquisition
- Investigation
- Data curation
- Writing (original draft)

(signature)

Masoud Foroutan Koudahi

POZNAN UNIVERSITY OF TECHNOLOGY

Faculty of Chemical Technology

Institute of Chemistry and Technical Electrochemistry

Elżbieta Frąckowiak

March 27, 2024

Declaration of individual contribution in publications

As the co-author of the following papers, I hereby declare that my contribution to those works was:

Article 1: *Electrochemical Capacitor Performance of Nanotextured Carbon/Transition Metal Dichalcogenides Composites*

Authors: **Elżbieta Frąckowiak** (20%), Masoud Foroutan Koudahi (40%), Maciej Tobis (40%)

Journal: Small

DOI: https://doi.org/10.1002/smll.202006821

Contribution: - Supervision

- Conceptualization

- Methodology

- Review and editing

Elżbieta Frąckowiak

E. Frąckowiak

Article 2: *Fast response supercapacitor based on carbon-VS_2 electrodes with a wide operating voltage range*

Authors: Masoud Foroutan Koudahi (70%), **Elżbieta Frąckowiak** (30%),

Journal: Energy Storage Materials

DOI: https://doi.org/10.1016/j.ensm.2022.04.021

Contribution: - Supervision

- Conceptualization

- Data curation

- Review and editing

Article 3: *$Ti_3C_2T_x$ MXene as Intriguing Material for Electrochemical Capacitor*

Authors: Masoud Foroutan Koudahi (75%), **Elżbieta Frąckowiak** (25%),

Journal: Small

DOI: https://doi.org/10.1002/smll.202307165

Contribution: - Supervision

- Conceptualization

- Data curation

- Review and editing

Elżbieta Frąckowiak

E. Frąckowiak

Article 4: *Charge storage and operando electrochemical dilatometry of MXene electrodes in ionic liquids*

Authors: Masoud Foroutan Koudahi (55%), Andres Camilo Parejo Tovar (20%), François Béguin (10%), **Elżbieta Frąckowiak** (15%)

Journal: Submitted

DOI: -

Contribution: - Supervision

- Conceptualization

- Data curation

- Review and editing

Elżbieta Frąckowiak

E. Frąckowiak

(signature)

POZNAN UNIVERSITY OF TECHNOLOGY

Faculty of Chemical Technology

Institute of Chemistry and Technical Electrochemistry

Maciej Tobis

March 27, 2024

Declaration of individual contribution in publications

As the co-author of the following papers, I hereby declare that my contribution to those works was:

Article 1: *Electrochemical Capacitor Performance of Nanotextured Carbon/Transition Metal Dichalcogenides Composites*

Authors: Elżbieta Frąckowiak (20%), Masoud Foroutan Koudahi (40%), **Maciej Tobis** (40%)

Journal: Small

DOI: https://doi.org/10.1002/smll.202006821

Contribution: - Investigation

- Data curation

- Writing (original draft)

Maciej Tobis

(signature)

Maciej Tobis

POZNAN UNIVERSITY OF TECHNOLOGY

Faculty of Chemical Technology

Institute of Chemistry and Technical Electrochemistry

Andres Camilo Parejo Tovar

March 27, 2024

Declaration of individual contribution in publications

As the co-author of the following papers, I hereby declare that my contribution to those works was:

Article 4: *Charge storage and operando electrochemical dilatometry of MXene electrodes in ionic liquids*

Authors: Masoud Foroutan Koudahi (55%), **Andres Camilo Parejo Tovar** (20%), François Béguin (10%), Elżbieta Frąckowiak **(15%)**

Journal: Submitted

DOI: -

Contribution: - Investigation

- Data curation

Andrés Parejo-Tovar

(signature)

POZNAN UNIVERSITY OF TECHNOLOGY

Faculty of Chemical Technology

Institute of Chemistry and Technical Electrochemistry

François Béguin

March 27, 2024

Declaration of individual contribution in publications

As the co-author of the following papers, I hereby declare that my contribution to those works was:

Article 4: *Charge storage and operando electrochemical dilatometry of MXene electrodes in ionic liquids*

Authors: Masoud Foroutan Koudahi (55%), Andres Camilo Parejo Tovar (20%), **François Béguin** (10%), Elżbieta Frąckowiak (15%)

Journal: Submitted

DOI: -

Contribution: - Supervision

- Review and editing

.....

(signature)

François Béguin